International Materials Reviews 68 (2023) p. 1245-1319, DOI: 10.1080/09506608.2023.2265701

METHODS AND MODELS FOR FIBRE-MATRIX INTERFACE CHARACTERISATION IN FIBRE-REINFORCED POLYMERS: A REVIEW

Sina AhmadvashAghbash, Ignaas Verpoest, Yentl Swolfs* and Mahoor Mehdikhani
Department of Materials Engineering, KU Leuven, Kasteelpark Arenberg 44 bus 2450, Belgium
*E-mail: *yentl.swolfs@kuleuven.be*

Abstract

The fibre-matrix interface represents a vital element in the development and characterisation of fibre-reinforced polymers (FRPs). Extensive ranges of interfacial properties exist for different composite systems, measured with various interface characterisation techniques. However, the discrepancies in interfacial properties of similar fibre-matrix systems have not been fully addressed or explained. In this review, first, the interface-forming mechanisms of FRPs are established. Following a discourse on three primary factors that affect the fibre-matrix interface, the four main interface characterisation methods (single-fibre fragmentation, single-fibre pull-out, microbond, and fibre push-in/-out tests) are described and critically reviewed. These sections review various detailed data reduction schemes, numerical approaches, accompanying challenges and sources of reported scatter. Finally, following the assessment of several infrequent test methods, comprehensive conclusions, prospective directions and intriguing extensions to the field are provided.

Keywords: *Carbon fibre; Glass fibre; Epoxy; Thermoplastic; Interface characterisation; Interfacial shear strength; Interfacial fracture toughness; Interfacial friction coefficient*

1. Introduction

The high stiffness, strength, and low density of fibre-reinforced polymers (FRPs) make them an exceptional choice for lightweight structural components and a part of the solution for resolving the climate crisis. FRPs are highly tailorable: they can yield different mechanical behaviour by adjusting, for instance, their fibre type, orientation, or volume fraction. The most common reinforcing fibres are carbon (CF), glass (GF) and natural fibres, and the most frequent matrices are polyester and epoxy (thermoset), and thermoplastics such as polypropylene (PP), polyamide (PA), polycarbonate (PC) and high-temperature thermoplastics such as polyether ether ketone (PEEK) and polyetherimide (PEI). The fibre-matrix interface plays a crucial role in the mechanical properties of FRPs since the stress is transferred between these two components through their interface. Achieving superior load transfer efficiency and mechanical properties is contingent upon establishing strong compatibility between the fibre and matrix at the interface. Several methods, such as interfacial adhesion modifiers, coatings, and surface treatments, are employed to improve interfacial bonding in FRPs. These methods improve one or more of the six main mechanisms to form an interface in FRPs (see Fig. 1).

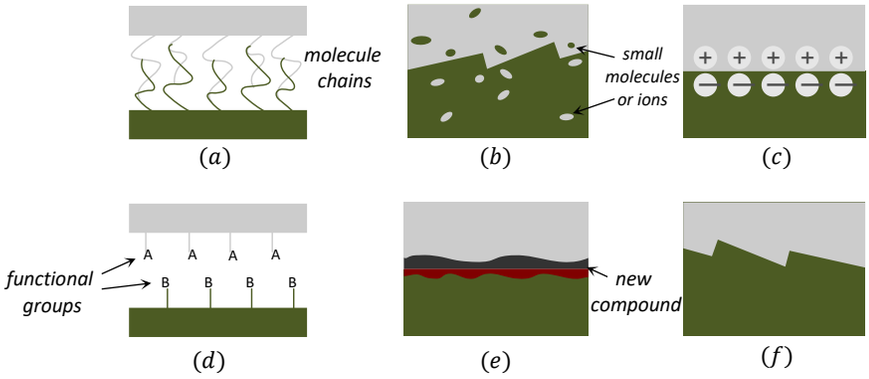

Fig. 1. The six main mechanisms to form a fibre-matrix interface: (a) molecular entanglement, (b) inter-diffusion of elements, (c) electrostatic attraction, (d) chemical reaction between groups on reinforcement and matrix surfaces, (e) chemical reaction forming of a new compound, particularly in metal matrix composite, and (f) mechanical interlocking (redrawn from [1]*).*

In the interaction between fibre and matrix, an intricate situation develops in which a third phase is thought to exist. This third phase extends between the fibre and matrix, known as the interphase (see Fig. 2a), and results from physicochemical interactions between the constituents. In this 3D region, the matrix molecules have a constrained degree of freedom to polymerise [2]. As a result of these restrictions, the interphase material can be perceived as a region with varying properties (from those of fibre and matrix) [2]. Within the interphase, Nath et al. [2] suggested a quadratic variation of the elastic modulus and Poisson's ratio as a function of radial distance from the fibre axis. On the other hand, the interface is a 2D surface that forms around the fibre, where it comes in contact with the matrix.

The properties of FRP constituents do not always translate into expected performance in manufactured FRPs [3–5]. The bond between fibres and matrix is regarded as the heart of FRPs. Thus, ensuring good bonding between them is crucial. For instance, fibre surface modification can lead to improved intra- and interlaminar crack resistance of novel FRPs [6,7]. The quality of the bond also affects other macroscopic interface-reliant properties of the composite, such as its shear strength [8], compressive strength [9], translaminar fracture toughness [10], transverse strength, response to environmental exposure (such as aqueous or corrosive) and its impact performance [11]. The interface/interphase is subjected to a complex force field, and its failure will be determined by the applied stress tensor, as well as the chemical or mechanical affinity of the two phases (fibre and matrix). Debonding reduces the load-bearing capability of the composites. Interphasial failure modes can be categorised into three types based on the failure location: interface failure, failure in the modified reinforcement or failure in the modified matrix, as shown in Fig. 2b-d (apart from matrix or fibre failure out of the interphase region). These failure modes can occur separately or simultaneously depending on the bond, fibre, or matrix shear strength [1]. The experimental methods for characterising the fibre-matrix adhesion are agnostic on the difference between interface and 3D interphase. However, none of the major models that are used for data reduction explicitly incorporate the interphase. We will, therefore, mainly be referring to *interfacial failure* in the rest of this review article.

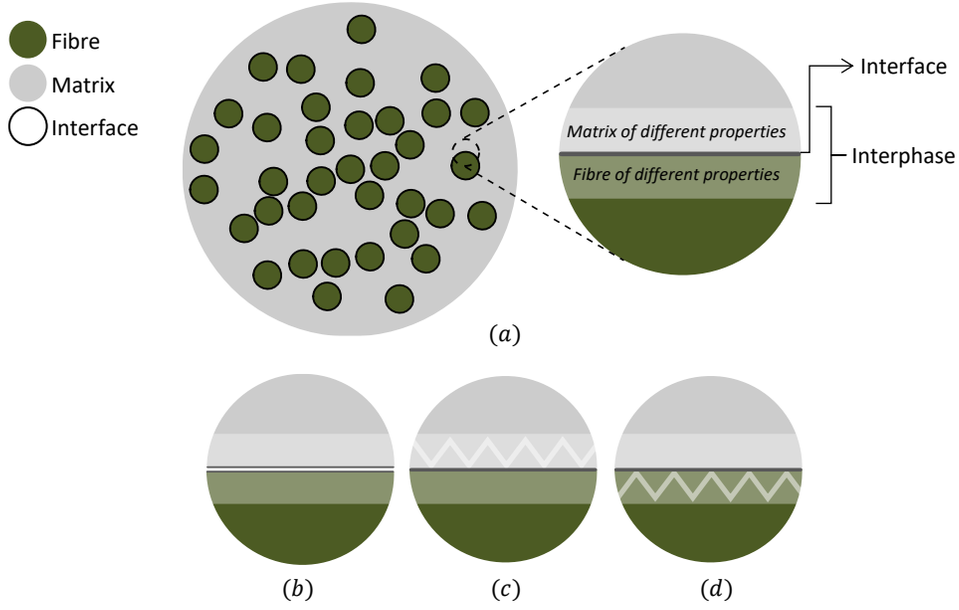

Fig. 2. Schematic illustration of: (a) the interface and interphase in the FRPs, and failure modes of interphase: (b) debonding failure, (c) failure in the modified matrix and (d) failure in the modified reinforcement (redrawn from [12,13]*, with permission from Elsevier).*

The mechanical tests for interface characterisation in FRPs, depending on the testing scale, can be classified into three categories:

- Nanoscale: these measurements are typically carried out by pulling-out a nano-fibre (for instance, on carbon nanotubes) or nanoparticle by the probe in a scanning probe microscope or atomic force microscope [13].

- Microscale: following the micromechanical models, direct micromechanical tests were developed to characterise the interface through debonding the (microscale) fibre from the matrix. The main microscale tests are the single-fibre fragmentation test, single-fibre pull-out test, microbond test and fibre push-in/-out test.
- Macroscale: macroscale mechanical evaluations for laminated or filament wound FRPs include indirect test methods such as short beam shear test (ASTM D2344 [14]/ISO 14130 [15]), transverse flexure test (ASTM D7264 [16]/ISO 14125 [17]), fibre bundle pull-out (using fibre bundles instead of a single fibre) [129], and transverse fibre bundle tensile (TFBT) and 45° fibre bundle tensile (45FBT) tests [130,131].

The nanoscale tests are not relevant for typical fibres in FRPs. These tests do not provide direct results on the interface since the microlevel heterogeneity of FRPs complicates the measurement of their microscale properties via a macrolevel test. This makes macroscale tests more suitable for relative comparisons than for absolute measurements of interface properties. Thus, this review only considers the microscale methods. The micromechanical models enable the deconstruction of the macroscale behaviour into simpler fibre-matrix interactions. However, the interfacial debonding models require demanding inputs: interfacial shear strength (IFSS) and interfacial fracture toughness (IFFT). The normal interfacial strength is somewhat less studied since mode II is frequently the dominant failure mode (for studied CF/GF-epoxy systems) [18]. To clarify, fracture toughness is typically expressed in MPa$\sqrt{m}$ unit, while the IFFT within this review is presented in J/m^2 (fracture energy unit rather than toughness unit), which is a commonly used unit in interface-related literature. The IFFT plays a crucial role in micromechanical models that aim to predict transverse crack development [19,20]. As a result, obtaining accurate measurements of the mode I and II IFFT is essential in propelling progress in the field of FRPs.

Fibre-matrix interfacial characterisation still poses some challenges from both practical and theoretical aspects. The laborious manufacturing process involves the manipulation of individual thin fibres, requires specific test setups, and sometimes uses non-standardised test methods. Additionally, there are theoretical disputes over parameter selection and data reduction approaches for extracting interface parameters from the test data [21]. In the early 1990s, a round-robin exercise on micromechanical tests to measure the IFSS [22] reported an acceptable scatter within each laboratory but a high degree of inter-laboratory scatter for a specific test and material. This highlighted the demand for improved and unified data reduction and standardisation schemes.

To characterise the interface, direct or indirect observation methods can be exploited, including scanning electron microscopy (SEM), transmission electron microscopy, and Fourier-transform infrared spectroscopy. These tools can provide a morphological/structural or chemical interfacial bond analysis and therefore are beneficial for understanding the interface forming mechanisms from a physical or physicochemical viewpoint. Fibre diameter, d_f, being the most common physical feature, can be measured through microscopy, vibrometry or laser diffraction [23]. Furthermore, the effect of treatment of the fibre surface on the interfacial properties is reflected by interfacial chemical bonding, modified surface energy, and hence, the wetting of the fibre (which furthermore can affect the mechanical interlocking).

Overall, the fibre-matrix interface characterisation in FRPs is a complex and multi-faceted task requiring various experimental techniques and analytical methods. Some of the critical parameters that need to be measured in the fibre-matrix interface characterisation of FRPs include: IFSS, IFFT and interfacial friction coefficient (μ_i). These critical parameters affect the load transfer from the matrix to the fibre and are essential for enabling more precise predictions. Due to the complexity and heterogeneity, major uncertainties exist in the measured interfacial properties, leading to an insufficient theoretical correlation between the microscale interfacial properties and the mechanical properties of FRPs. Analysing the interfacial debonding process can be achieved through numerical interface simulation. The finite element (FE) method (FEM) is the most frequently used approach to simulate the

FRPs' behaviour under various loading scenarios and length scales, described by constitutive models such as the continuum damage model, cohesive zone model (CZM), and Coulomb friction [1]. Other interface simulation methods include the discrete element method [24], the boundary element method [25], and molecular dynamics [26–28].

Analysis of the bibliographic data in Web of Science shows that the share of the publications on the interface in FRPs field per year, complying with the search criteria "(*composite**, *carbon fib*/glass fib**, *matrix/epoxy/thermoplastic and interfac**)" normalised by "(*composite**, *carbon fib*/glass fib**, and *matrix/epoxy/thermoplastic*)", has increased from 0.4% in 1990 to almost 6% in 2021. These results showcase an escalating interest in interfacial studies. This paper, therefore, critically reviews seven decades of literature on fibre-matrix interface characterisation in FRPs. The majority of the available review articles (e.g., [13,29]) focus on primary data reduction methods for simplicity. However, in addition to basic approaches, the current review paper elucidates comprehensive data reduction methods for each micromechanical test in unambiguous and more straightforward steps. Consequently, acting as a reference for interfacial studies in FRPs, this paper reduces the time and effort required for progressive and inclusive comprehension. Section 2 provides a concise examination of three primary factors (matrix cracking, fibre surface treatment/sizing, and curing cycle) that have significant roles in the majority of micromechanical tests utilised for characterising the interface. The subsequent four sections describe and review the most frequently used methods, which are single-fibre fragmentation (Section 3), single-fibre pull-out (Section 4), microbond (Section 5), and push-in/-out tests (Section 6). Each section is concluded by reporting the highly sought-after interfacial properties for different composite systems measured with that method. The seventh section briefly reviews some less frequent test methods, and the final section concludes this review and provides recommendations for future work. It is envisioned that this review will aid in steering future research efforts in the most fruitful way possible to expedite the creation of a rigorous methodology and, ultimately, a standard for determining interface properties. Eventually, this might be employed to measure the interlaminar shear strength of a UD laminate; nonetheless, further research is warranted.

2. Influencing factors

Interfacial failure can be significantly affected by matrix cracking, fibre surface treatment/sizing and the curing cycle. We, therefore, first describe these three features before diving into the specific test methods. Note that matrix cracking is only relevant for fragmentation tests, as it does not occur in the other test methods.

2.1. Matrix cracking

The (co-)existence of interfacial debonding and transverse and/or bi-conical matrix cracks in SFFT affect the stress transfer to the fibre. The debonding occurrence can minimise the matrix crack initiation probability or the extent of its propagation [30]. The small matrix cracks are predominantly associated with the instant energy release due to a fibre break and do not significantly propagate during SFFT. The three common damage modes at the fibre fracture site, based on experimental observations [2,31,32] and interfacial adhesion level, are:

- Mode α: for very strong interfaces, the crack propagates extensively into the matrix, which can lead to specimen failure. The resulting disk-shaped crack, normal to the fibre (see Fig. 3a), grows suddenly, and its size is determined by the magnitude of the strain energy released when the fibre fails and the crack sensitivity of the matrix surrounding it. Reportedly, this mode occurs mainly in aramid fibre-epoxy systems [31,33].
- Mode β: for a weak interface, the fibre breaks hardly damage the matrix and reveal an immediate widening of the breaking gap due to extensive debondings. Some of these breaking gaps can even become larger than $5d_f$ with additional loading [34] (Fig. 3b). This failure mode has been detected in GF and unsized CF model composites [32,35]. A characteristic feature of this mode

is that a portion of the fibre load-bearing capability is sustained via the frictional stress transfer across the debonded interface.

- Mode γ: a conical matrix crack initiates at the fibre end and propagates into the matrix at an angle with respect to the fibre axis (see Fig. 3c, with 45° or 21° as in [2]). This failure mode is probable in high-modulus CF-epoxy systems [2,36] and in a matrix material that exhibits a lower shear strength relative to its tensile strength.

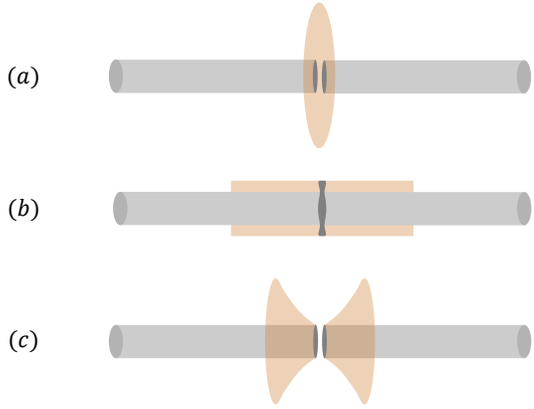

Fig. 3. Three types of fracture in the matrix in SFFTs: (a) a disk-shaped matrix crack indicating a strong interfacial bond, (b) fibre-matrix debonding which implies a rather weak interface, (c) double-cone matrix crack referring to a matrix with lower shear strength than the tensile strength. Note that crack (c) becomes nearly normal to the fibre axis as it propagates (redrawn from [37]*).*

2.2. Fibre surface treatment and sizing

There are two primary methods for achieving an optimal interfacial bond: treating the surface of the fibre/reinforcement or modifying the composition of the matrix (see Fig. 2). However, it is important to note that the objective is not always to maximise the bond strength. In brittle matrix composites, an excessively strong bond could lead to embrittlement.

The interfacial bond strength significantly relies on the surface treatments applied to the fibre. *Size* (also known as fibre finish or coating) is a protective coating applied to the fibre surface that improves the fibre handling during processing and enhances the interfacial adhesion. The process of coating fibres with *size* is termed *sizing*. Nonetheless, many authors use the sizing terminology instead of *size*, which can often save confusion in "fibre size" not relating to the "fibre dimension" [38]. Fibre sizing is arguably the most crucial element involved in GFs and GFRPs manufacturing and their optimal functioning. Yet due to the high level of secrecy surrounding size formulations, only a limited number of individuals within the extensive supply chain of FRPs suppliers, processors and end-users have a profound grasp of GF sizings. An inquisitive reader may refer to a recent review article by Thomason [38] that provides an in-depth analysis of GF sizing. This article explores various aspects, such as sizing formulations, their impact on the performance of both the fibre and the composite, as well as the challenges and advancements in GF sizing technology.

SEM and X-ray photoelectron spectroscopy can be utilised to characterise the surface morphology (or roughness) and to examine the chemical structure of the fibre surface, respectively [39]. The IFSS enhancement can be directly related to the number of chemical functional groups on the fibre surface [40] or micromechanical interlocking (Fig. 1f) due to surface roughness [39]. Note that the CF structure has distinct "skin-core" characteristics. The graphite crystallites on the CF skin layer are in a compact arrangement and lack active carbon atoms. This results in low surface energy and inadequate functional groups for chemical reactions [41]. Based on experimental evaluations on a CF-epoxy system [42,43], the IFSS is influenced chiefly by the local morphology of the outermost graphite surface layers and the number of active sites. Apart from sizing [44,45], various methods have been developed to modify the

fibre surface activity, roughness, and wettability and hence improve the interfacial adhesion. For CFs, these treatments include electrochemical [46] or wet chemical oxidation (with aqueous ammonia) [47], gas-phase oxidation in ozone or oxygen mixtures [48], γ-ray irradiation [49], ultrasonic treatment [50], carbon nanotubes (CNTs) deposition (with methods such as chemical vapour [51] or electrophoretic deposition [52] or layer-by-layer grafting [53]), and plasma treatment [54].

Oxidative surface treatment chemically activates the surface layer of CFs (see Fig. 1d), increasing the interaction with the matrix [55]. Plasma treatment increases both the surface energy and roughness of the fibre to improve the wettability of the fibre by the matrix and the micromechanical interlocking (see Fig. 1f) [56]. The fibre sizing, succeeding surface treatment, creates a brittle interface/interphase layer which increases the IFSS but could potentially alter the failure mode from interfacial debonding to matrix cracking (see Fig. 2) [57]. The grafting of CNTs onto the CFs enhanced the IFSS between the CNT-CF hybrids and the epoxy resin in [53,58]. Contrarily, a lower IFSS with CNT-grafting was achieved in [59], which was linked to the smaller size and lower density of the grown CNTs, lowering the contribution of fibre surface roughness. Moreover, the CNTs were more hydrophobic than the unmodified CFs, resulting in poorer wettability (larger contact angle) with the epoxy resin [60]. The advantage of CNT-grafting chiefly relies on the tensile strength of CNTs and their interfacial cohesion with the matrix. The utmost enhancement is acquired when the matrix is allowed to absorb energy through microscale damage, and the CNT debonding at the nanoscale has only a partial contribution to it [61]. According to Godara et al. [62], the most efficient strategy for enhancing the IFSS is achieved by exclusively incorporating CNTs in fibre sizing [62,63].

Graphene oxide and other 2D materials have gained attention due to their desirable properties, including high specific area, flexibility, and good mechanical, thermal, and electrical conductivity [64,65]. Graphene oxide exhibits higher chemical reactivity with both the fibre and epoxy resin compared to graphene. This is attributed to the presence of epoxide and hydroxyl groups within the graphene oxide sheets, as well as carbonyl and carboxyl groups at their edges [66]. This property enables improved mechanical interlocking at the fibre-matrix interface (see Fig. 1f), making fibre surface modification with graphene oxide a viable strategy [7,67]. A similar approach, treating the CF surface with polydopamine and graphene oxide, yielded enhanced IFSSs in [7].

Both short- and long-term FRP performances are critically influenced by the optimisation of fibre sizing [38]. Significant reductions in glass-fibre-reinforced polymers (GFRPs) performance were directly correlated with a loss of fibre-matrix adhesion caused by thermal degradation of some of the primary sizing components in [68]. Reportedly [35], the interfacial failure of their sized system consisted mainly of mixed-mode cracking, whereas clear fibre-matrix debonding was observed in the unsized system. Reportedly and based on LRS and SEM observations [35], sized CF-epoxy systems can withstand higher interfacial shear stresses than unsized ones. However, this might lead to a mixed-mode interfacial failure which is undesirable since only a portion of the crack faces are in full contact, and, therefore, the effective length of the fibre reduces heavily. On the contrary, a clear mode II debonding was observed for the unsized systems, in which the radial compression, which was developed throughout the curing, effectively kept the interface closed [35].

As a plausible scenario in UD FRPs, an improved surface treatment could give rise to shorter debonded and ineffective lengths, potentially leading to the development of transverse matrix cracks. The transverse matrix crack results in an increased stress/strain concentration factor (SCF) on the neighbouring fibres, causing brittle failure of the FRP. Consequently, it was shown that the tensile strength of a UD CF-epoxy FRP was maximised when 50% of the standard commercial fibre surface treatment was used [69]. Hoecker and Karger-Kocsis [70] studied the effect of the interface on the transverse and impact properties of the CF-epoxy FRPs. The effect of the adhesion quality was observed in a transverse tensile test, even though the loading direction in this test is very different from the SFFT. The improvement in properties was attributed to differing mechanisms of failure, which changed from a clean fibre surface fracture to a cohesive matrix failure (similar to Fig. 2c) as the interfacial adhesion improved. The relevance of the interface to the transverse flexural properties was not observed.

Furthermore, short beam shear tests did not show the effect of the adhesion, while the transverse Iosipescu test shows improved shear properties for the composite with the improved adhesion, as suggested by the micromechanical tests. The Charpy impact resistance of the UD laminates were a complex function of the interfacial adhesion. An improvement in impact properties of an FRP with a "good" interface (as predicted by the micromechanical tests) was observed, which is contrary to the popular belief that improved adhesion will cause brittle failure of the composite [70]. Moreover, the effect of interfacial adhesion can be substantial in the case of compression-moulded or injection-moulded short-fibre composites since a major portion of the fibres will not be aligned with the loading direction [71].

Based on the above discussion, it can be concluded that the macromechanical properties are a complex function of the interface properties as measured from the micromechanical tests, in particular, the SFFT. A clear understanding of the translation of the micromechanical results to the macromechanical properties is still being developed. A proper consideration of the loading scenario of the ultimate composite application is therefore indispensable for the design of the optimal interfaces for the improved mechanical properties of the FRPs [71].

2.3. Curing cycle

The type of curing cycle utilised can impact interfacial properties. Cross-linking occurs during the curing of thermosets, and there may be various alterations, such as changes in elastic modulus, thermal expansion coefficients, expansion paired with contraction, and increases/decreases in toughness and plasticity. With multiple variables throughout the curing process, it is challenging to fully understand how curing schedules alone affect adhesion without considering factors such as the resin's degree of cure or crosslinking [72].

Ideally, the curing cycle for microcomposites should align with that of conventional FRPs. Not only do cure pathways influence the interfacial properties, but the cure paths required to fabricate the specimens for each of the testing methods is fundamentally different to those recommended by manufacturers for making FRP laminates due to the different geometries and small amounts of materials used. Furthermore, even if the exact same cure cycle were used for SFFT (or other) specimens, the resulting microstructure would likely be different due to thermal effects, heat transfer limitations, and material volume-to-surface area ratio. These factors, in turn, impact the cure kinetics and environmental factors at play. The higher the temperature of post-curing, the higher the T_g and crosslinking degree will be. However, post-curing leads to a modification of FRP mechanical properties, especially at high temperatures (~170°C for epoxies). For instance, both tensile strength and elongation at break are reported to decrease when the post-curing temperature increases [73]. Haider et al. [74] and Li et al. [75] indicated that curing temperature does not directly impact the final cure shrinkage of a thermoset material. Instead, shrinkage is determined by the degree of cure achieved. Thus, it can be inferred that resins that have been cross-linked to the same degree will have similar residual stress levels. However, when curing temperatures are higher, the process occurs more rapidly, limiting the mobility of the polymer and reducing the time available for rearrangement towards a stress-free state. As a result, different levels of stress accumulation occur. Wang et al. [76] demonstrated how curing temperature and speed directly affect the residual stress state of an epoxy resin. The study found that rapid curing resulted in higher levels of internal stress.

ElKhoury and Berg [72], for CF-epoxy SFFT specimens, investigated the effects of a number of curing cycles, curing temperature and schedule, degree of cure, use of accelerants, annealing, and the use of fibre handling agents. To achieve the highest apparent adhesion, curing at the highest temperature in a single stage is the most effective method. The addition of accelerants can speed up the curing process without affecting the level of adhesion, but it may reduce the plastic yield strength in some cases. Annealing of thermoset composites can reduce both the induced residual stress and the apparent adhesion but cannot lower it below the level attained at lower curing temperatures. For thermoplastic composites,

Wang et al. [77] indicated that post-process annealing could significantly affect apparent adhesion due to the development of internal stress. This suggests that the thermal history of polymers must be considered during the design process.

3. Single-fibre fragmentation test

Single-fibre fragmentation test (SFFT), occasionally referred to as the single-fibre composite test, is the most common interface characterisation test. An SFFT provides concurrent *in-situ* insights into both the statistical fibre strengths at small gauge lengths and the fibre-matrix interfacial properties. Many of the theoretical fundamentals for interfacial load transfer were based on this test and later used in other test configurations. It typically uses a dog-bone-shaped or straight specimen containing a single fibre (see Fig. 4). The specimen is strained in tension along the fibre axis. Upon further straining, the fibre will fracture consecutively at some flaw loci along its length. The fragments will be in tension due to the shear stresses transfer from the matrix via the interface. The fragmentation proceeds until no new breaks can occur, a state called saturation.

Historically, several models have been proposed to represent the stress distribution, the interface debonding and the frictional sliding between the debonded fibre and matrix. Generally, these models can be classified into *stress-based* and *energy-based* categories. The mechanical properties of fibre-matrix interfaces in FRPs were primarily described in terms of IFSS [78,79], which represented either the yielding of a ductile interface or the interfacial strength of a brittle interface. This concept sparked the development of the SFFT [78,79]. In the recent past, it has been proposed to characterise the fibre-matrix interface in terms of debond energy and frictional shear stress or Coulomb friction [80–82]. The basis for such models is derived from observations made during SFFTs, indicating that fibre-matrix debonding takes place progressively under monotonic loading [83]. According to the stress-based models (shear strength criterion), debonding occurs when the interfacial shear stress reaches the interfacial shear bond strength. However, in an energy-based approach, the crack propagates once the energy release rate reaches the interfacial fracture toughness value. A comprehensive model must integrate all the key features in the interface analysis, including debonding, thermal residual stresses, frictional sliding, matrix plasticity and matrix cracking.

The following subsections critically review the data reduction schemes, experimental characterisation techniques and the features influencing SFFT. Once all the SFFT-specific subjects have been addressed, the final segment before the conclusions will give a concise overview of the multi-fibre fragmentation test.

3.1. Data reduction schemes

3.1.1. Cottrell-Kelly-Tyson model

Cottrell (1964) [78], Kelly and Tyson (1965) [84] (CKT), concurrently but independently, used a simple force balance to calculate the average IFSS. They assumed that the matrix is perfectly-plastic, and the interfacial shear stress is constant and equal to the shear yield strength of the matrix, τ_y, in the recovery region. This results in a linear axial stress build-up from 0 at the fibre fragment end to the applied stress level farther from the fibre end, where it reaches a plateau. At saturation, the fragments are too short to reach the applied stress, and thus the plateaus disappear (see Fig. 4). In this model (also known as the simple shear-sliding model), the interface bears any shear stress up to the IFSS, after which the deformation occurs through interfacial sliding. This model assumes that all the stress recovery in the broken fibre occurs through shear sliding. The primary shortcoming or uncertain presumption is that the interfacial shear stress is constant over the fibre length. Additionally, real-world materials are seldom perfectly-plastic.

Due to the assumption of constant interfacial shear stress in the CKT approach, this scheme is not suitable for fibre-polymer systems, in which friction is not the primary mechanism for axial stress

transfer. However, for ceramic-/metal-matrix composites, with absent interfacial chemical bonding, the CKT reduction scheme may provide a reasonable estimate of the interfacial yield stress. This, in principle, is due to the underdeveloped constitutive models. The response of metallic materials to applied loads can be described with greater precision compared to that of thermoset matrices. This is due to the fact that the mechanical behaviour of amorphous thermoset matrices possesses a degree of atomic-level long-range order [4].

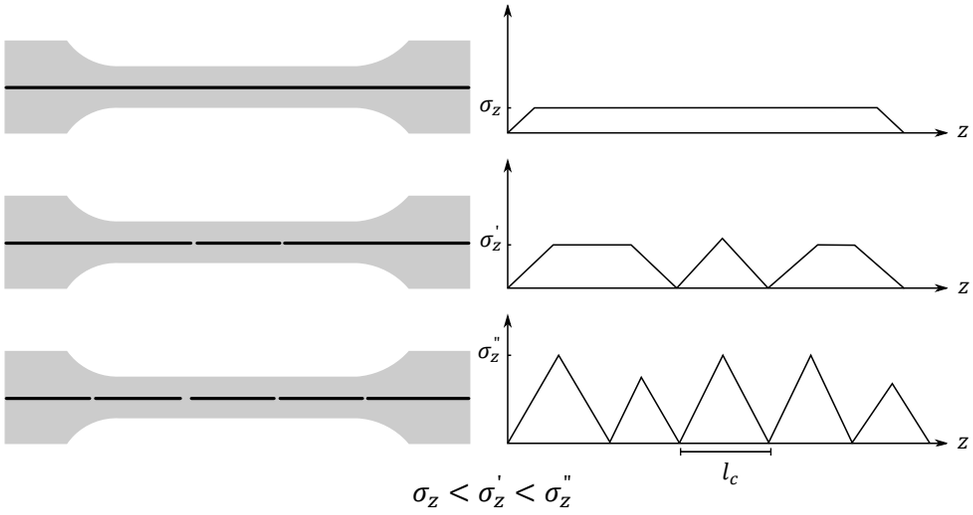

Fig. 4. Schematic representation of the fragmentation process in SFFT. Left: specimen with an increasing number of fibre breaks due to increased loading. Right: fibre axial stress along its length (z-axis) for the corresponding applied stress levels. The zero stresses correspond to the positions with fibre breaks (redrawn from [39]*, with permission from Elsevier).*

The critical length of the fibre, l_c, the length below which the fibre cannot fragment any further due to insufficient load transferred to it via the interface, is calculated as:

$$l_c = \frac{d_f \sigma_f(l_c)}{2\tau_y} \tag{1}$$

with d_f denoting the fibre diameter and σ_f being the fibre failure strength at l_c. Based on this model, the l_c is often considered to be a material constant and independent of the applied strain [85,86]. Fig. 5 depicts the effect of fibre length on the axial and shear stress profile along the fibre. The fragment lengths are measured conventionally either directly by transmission optical microscopy [55] or indirectly via acoustic emission (AE) [87,88]. The modified versions of this relation (such as in [89]) vary by the definition of the critical length or the incorporation of the length-dependency of σ_f. The l_c can be:

(1) the same as the arithmetic mean of the fragment lengths at saturation, $l_c = l_{avg}$ [90,91],
(2) the widely used definition of $l_c = 4/3\ l_{avg}$ (also called the corrected length) [92],
(3) the maximum fragment length, $l_c = l_{max}$ [90,91], or
(4) equal to the fibre fragment length at which the maximum fibre axial stress coincides with its nominal strength from the single-fibre tensile tests [89].

The choice of *corrected length* is based on the premise that the lengths of the fibre fragments from SFFT data fall within the range of $l_c/2$ to l_c. However, it has been documented that the distribution of fragment lengths does not conform to this range, as evidenced by studies such as [93–95]. Drzal et al. [95] utilised a two-parameter Weibull distribution, discussed in [93], to model the fragment length distribution during the saturation stage. Therefore, the IFSS values obtained using any traditional approaches for the critical length (option (1)-(3)) are of relatively low importance, as emphasised in [93]. The "nonlinear stress transfer model" [89] warns against using l_c alone to determine IFSS. Instead, it suggests that SFFT data analysis should be used with caution, taking into account both the fragment

lengths and test specimen loading to avoid overlooking possible changes in fibre strength. This approach will help prevent potential changes in fibre strength and ensure accurate results [89].

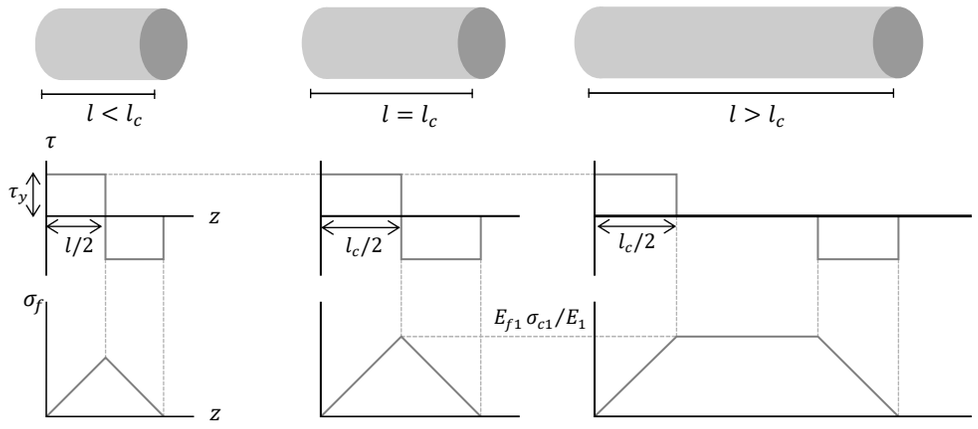

Fig. 5. Effect of fibre length on axial and shear stress profile along the fibre according to the CKT model. $E_{f1}\,\sigma_{c1}/E_1$ is the fibre stress in a continuous fibre composite under longitudinal composite stress, σ_{c1}, with the longitudinal modulus of E_1.

It should be pointed out that the CKT model solely considers the load transfer that transpires within the plastic zone at the fibre ends, disregarding the effects of elastic load transfer in the central portion of the fibre ($\tau_i = 0$). This approach remains valid under the assumption that the plasticity threshold of the matrix (or the interfacial sliding threshold) is minimal. Accordingly, plastic deformation (or slippage) occurs at the onset of loading, without an elastic load phase.

Meeting the saturation condition is primarily regulated by the yield strain of the matrix rather than the fibre failure strain [96]. This indicates the necessity of a matrix system with a higher failure strain than the embedded fibre. A typical recommendation is for the matrix failure strain to exceed the fibre failure strain by at least three times [22]. Alternatively, the coaxial geometry fragmentation test (bimatrix SFFT) can be used to extend the applicability to brittle resin systems that cannot attain saturation. This intricate method applies a thin coating of the brittle resin of interest to the fibre surface before being enclosed in a tough resin [97,98].

Regarding the standardisation and round-robin efforts, an inter-laboratory round-robin on the SFFT was accomplished with the participation of seven laboratories [99] (similar to [22]). To conduct the test with minimum operator dependency, a set of protocols is essential. The principal steps proposed by the round-robin were:

1. Measure d_f at *five* different locations in the gage section with an accuracy of at least ±1 μm,
2. Place fiduciary marks on the specimen to facilitate strain measurements,
3. Increment coupon strain by 0.2%, hold for 8 min before counting fibre breaks,
4. After a 10 min interval from the completion of the previous strain increment, apply the subsequent strain step and repeat till saturation,
5. Document the images of the fibre under polarised light at saturation,
6. Measure the fragments lengths pre-unloading.

The CKT approach of measuring an average IFSS from the SFFT is an oversimplification that can only be justified in full debonding or full matrix-yielding cases. The search for a better data reduction scheme resulted in partially-elastic models that divided the interface into inelastic and elastic regions and disconfirmed the CKT critical length as a strain-independent material constant [42,86]. Moreover, the *constant interfacial shear stress* assumption was discredited by experimental observations [100]. Further experiments invalidated the intrinsic assumptions of the CKT model, such as meeting the perfect saturation state [101], its inability to differentiate bonded/debonded surfaces and disregarding the effect

of matrix plasticity and interfacial friction [102]. Recently, modified versions of CKT and Bader-Bowyer (derived from the original CKT model) [103,104] models were proposed [105]. These versions calculate the IFSS for short (aspect ratio < 20) and ultra-short (aspect ratio < 10) fibre composites and consider the end effects that were excluded in the original model.

3.1.2. Cox (shear-lag) model

The shear-lag approach, developed by Cox (1952) [106], assumes that the matrix in a polymer composite is exceedingly compliant compared to the fibre. The matrix, therefore, does not contribute significantly to the tensile stiffness of the composite. Accordingly, the acting longitudinal loads in the matrix can be neglected, simplifying the calculation of fibre stresses. The matrix is exclusively responsible for transferring shear loads occurring at the fibre ends of a discontinuous fibre or a fibre break site. These shear loads occur due to the mismatch in longitudinal strain between the fibre ends and the surrounding material. To generate an analytical formulation, a matrix volume around the fibre, whereupon the shear stresses act, is required. This volume commonly takes the form of an arbitrarily drawn cylinder with the radius R_m around the fibre with a radius r_f. This model still forms the basis for many recent models. The main assumptions of these shear-lag-based stress transfer models (1D analytical models) are linear-elastic isotropic and well-bonded constituents, non-interacting fibre fragments and the absence of residual stresses and plasticity.

Lacroix et al. [107] used a unimodal Weibull distribution for the fibre strength to predict the critical length in SFFTs. They compared the results for fully-elastic (perfect adhesion), partially-elastic and total-debonding 1D shear-lag-based models. The fully-elastic model predicts that the critical length decreases as the applied strain increases, while the total-debonding model considers it a material constant (assuming frictional sliding stress to be strain-independent). The more realistic partial-debonding model predicts lower values of critical length compared to the overestimated lengths by the CKT model, underlining the significance of considering both IFSS and frictional sliding in processing the SFFT data [107].

The Cox-based models, limited by the introduction of the effective matrix radius, R_m (whose physical existence has not been defined clearly in the case of single-fibre composites), and disregarding hoop and radial stresses, were more qualitative than quantitative [108]. Nairn [109] comprehensively examined the potential of the shear-lag methods (SLMs). The shear-lag inaccuracy grows as E_f/E_m decreases or at low fibre volume fractions, V_f (approaching the case of a fibre embedded in an infinite matrix). The shear-lag parameter, β, employed in various shear-lag analyses of composites (see Appendix Table 1.A), depends on the material properties and the geometry of the problem. To have a reasonable agreement with FEM predictions, the erroneous β suggested by Cox, β_{Cox}, must be replaced by the β's proposed notably by Nairn [109], Nayfeh [110] or McCartney [111] for two concentric cylinders case. Nairn [112] extended his *optimal* shear-lag method (for perfect interfaces) [109] to a *generalised* analysis to include imperfect interfaces. Nairn's analysis also handles any fibre volume fractions and anisotropy levels of the fibres. Fig. 6 compares the CKT and Cox model predictions for the axial stress recovery of a broken fibre.

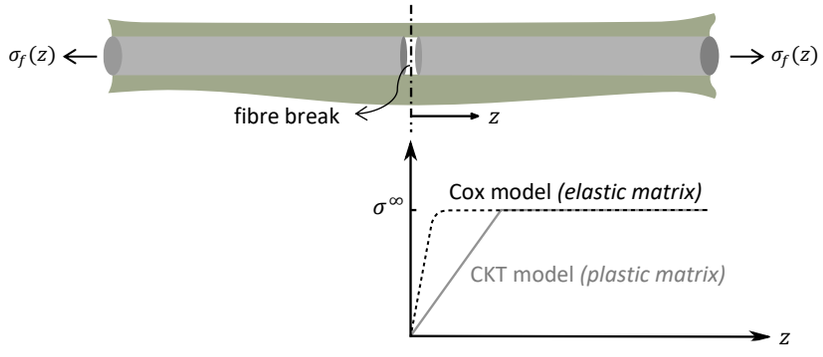

Fig. 6. Predicted stress recovery profiles by CKT and Cox models (adapted from [113]*).*

Following the initial shear-lag analysis, the extended SLMs include models with a matrix carrying tensile stress [114], elastoplastic matrix [115,116], debonded fibre-matrix interfaces [117,118], and matrix with linear damage evolution along with interfacial slipping [119]. The shear-lag analyses have also been supplemented with fibre-strength statistical models [118,120,121] to predict composite failure. The polymeric matrix properties can also affect the measured interfacial properties. Based on Cox's [106] prediction (see Table 1.A), the IFSS increases with increasing matrix shear modulus, G_m, and presumably elucidates why amorphous thermoplastics, typically possessing a lower G_m than thermosetting matrices, have a weaker adhesion to CF [122]. In an elastoplastic SLM [123], the addition of interfacial debonding to matrix cracking slowed down the fibre axial stress build-up [124]. Having a perfectly plastic matrix rather than plastic deformation with hardening had a similar effect [124].

3.1.3. Other stress-based models

The 2D analytical models (based on axisymmetric micromechanics analyses) for SFFT were premiered by Whitney and Drzal (1987) [125] and were later refined by the variational mechanics' approach by assuming the axial stress to be independent of the radial direction either in both constituents [126] or merely in the fibre [127]. The axisymmetric model of Whitney and Drzal [125] (relevant equations given in Table 1.A) was competent at estimating all the stress components (also for transversely isotropic fibres) and reforming the shear stress distribution of the SLMs. The duo employed a stress function method that ensured a valid solution, but it had two drawbacks. Firstly, their stress function was not based on one that minimises the complementary energy. However, this solution showed good agreement with experimental data for high aspect ratios of fibre length over r_f [108]. Secondly, their evaluation only considered an isolated fibre break, whereas in actual SFFTs, the fibre breaks can interact [126]. Consequently, to improve the limitations of SLM and the Whitney and Drzal approach, Nairn [126] presented a closed-form, 3D, variational mechanics-based axisymmetric solution for the stresses around breaks in an embedded single fibre (the pertinent equations are not presented here, but can be found in [126]). This model implemented thermal residual stresses and interacting fibre breaks but was only relevant for perfectly bonded fibres (no debond nor frictional effects). Thereafter, the matrix plasticity exclusion was resolved by the plasticity effect model of Tripathi et al. [128]. The variational model of Wu et al. [129] considered both a perfectly bonded region and a discontinuous interface of a two-phase composite. Johnson et al. [130] in their plasticity model, by addressing the shortcomings of the plasticity effect model (for instance, no radial stress variation from bonded to debonded regions), integrated matrix non-linearity into the model of Wu et al. [129]. Nevertheless, it could not predict the debond initiation/propagation and required a predefined debond length.

The location of the debond tip reveals itself as an inflexion point in the fibre axial stress profile, with the debonded region having a linear stress build-up, while the rest displaying a Cox-type stress profile [32]. A key discrepancy between models is the shape of this transition region between the debonded and intact regions. Piggott (or similarly in [108]), claims that this shift is an unsmooth point of mathematical discontinuity, while Nath et al. [32] argue that the transition is smooth. This discrepancy emerges due to the linear elasticity assumption in Piggott's analysis, leading to stress singularities at the crack tip and a discontinuity in the stress recovery profile. Contrarily, the plastic zone at the crack tip in [32] creates a smooth transition in the fibre stress recovery profile. Fig. 7 and Fig. 8, respectively, compare the axial stress recovery of the broken fibre and the interfacial shear stress profiles for the full-bonding and partial-debonding models.

To conclude, Cox [106] and CKT [78,84] models offer analytical solutions to the interfacial stress transfer problem. Cox's SLM, presuming a linear elastic behaviour for both constituents, enables the determination of the fibre axial stress and shear stress between the fibre and matrix. This model is only viable at low applied strains prior to the inherent non-linear behaviour of epoxy resins at higher strains. The CKT model uses a perfectly-plastic matrix and determines the critical length by assuming a constant interfacial shear stress. Table 1.A in the Appendix elaborates on the major stress-based analytical models.

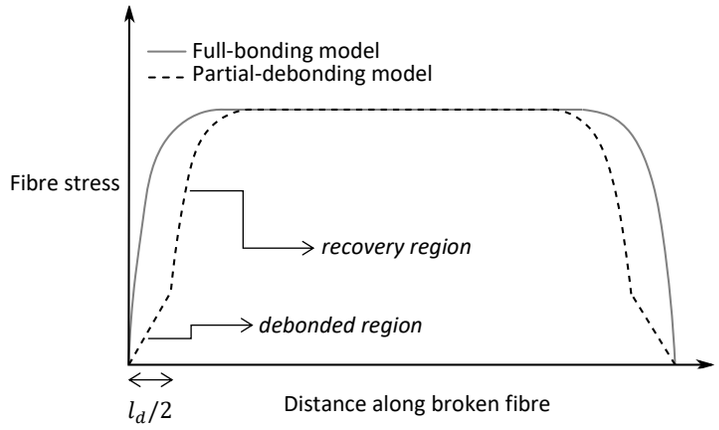

Fig. 7. Schematics of fibre stress distributions predicted by the full-bonding (Cox model [106]*) and partial-debonding* [131,132] *models (inspired by* [108] *and redrawn from* [133]*, with permission from Elsevier).*

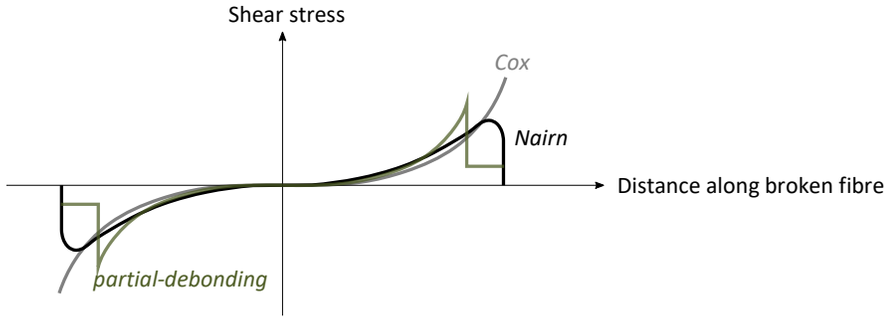

Fig. 8. Interfacial shear stress as determined by Cox [106]*, Nairn* [126]*, and partial-debonding models (redrawn from various figures in* [108]*).*

Assuming the perfect interfacial bonding and disregarding the existence of matrix axial stress can lead to inaccuracies in predicting the load transfer mechanisms and overall mechanical behaviour of FRPs using SLMs. Various solutions and alternatives to traditional SLMs have been proposed to address this issue, such as FE models and improved analytical models. For instance, Nardone and Prewo [134] considered the load transferred from the matrix to the end faces of the fibre, which was overlooked in Cox's original SLM that assumed a continuous or significantly long fibre compared to its d_f. A modified SLM [135] accounted for the influence of fibre shape on the fibre tensile stress distribution. Other studies, such as [136,137], have developed modified SLMs with a cohesive interface that can incorporate the effect of various factors such as cohesive interfacial shear stiffness, elastic properties of the fibre and matrix, fibre aspect ratio, and average fibre axial stress at the embedded end face on the stress-transfer characteristics and axial tensile properties of FRPs.

3.1.4. Energy-based approaches

The CKT model is not always accurate in calculating the IFSS when saturation is not attained. This drove the development of alternative data reduction methods, such as energy-based approaches [96]. Interfacial debonding is a major energy absorber during composite damage and failure [138]. An energy-based approach (fracture mechanics) is an eligible alternative to the traditional stress-based methods (strength of materials) for interpreting the SFFTs. The energy-based method was instigated using approximate Bessel-Fourier [139] or shear-lag-based (Cox-based [140] or Nayfeh-based [141]) analyses. With IFFT (G_{ic}) being a reliable parameter, the energy-based method allows the interfacial bond to be quantified even in SFFTs without saturation. Moreover, the accurate evaluation of the l_c is crucial for the design of FRP since it affects the FRP's fracture toughness, impact resistance, notched strength, and notch sensitivity. This property is relevant to loading along the fibre direction and can be used to measure

the IFSS, which plays a role in transverse cracking in multidirectional laminates. However, some micromechanical models for transverse cracking have revealed that IFFT may be even more essential than IFSS [19,20].

In FRPs with relatively poor adhesion, the released energy during fibre breakage typically initiates a short interfacial debond at the vicinity of the break [142]. However, the debond remains arrested at a certain distance since the strain energy release rate (SERR) decreases as the debond grows. Owing to the larger Poisson's ratio and coefficient of thermal expansion (CTE) of the matrix compared to the fibre, the debond crack surfaces are continuously in contact. Thus, the debond propagation is mode II-dominant [18,82,143] under tensile loading and below the curing temperature. Additional debond growth would require an increase in the applied strain [18]. Note that due to the brittle nature of the epoxy matrix, it is inclined to crack under tensile stress, which is the predominant mode of stress in mode I loading. The mentioned IFFT in the majority of the interface characterisation tests is more representative of a (near-) pure mode II cracking since the applied stress in mode II loading is parallel to the interface, which puts more stress on the interface itself rather than the matrix. However, in transverse cracking, both mode I and II components play a role.

Wagner et al. [144] use a 1D approach to determine the interfacial fracture energy caused by the initial debond. Their approach compares the energies before and after fibre and interface failure and considers the matrix contribution to the energy balance. The debonded region was assumed to be frictionless, and the residual stresses were neglected. However, the Boundary Element Method (BEM) [82] included the effect of these two key debond propagation suppressors. Using the solution of the BEM model (investigated for GF-epoxy), Graciani et al. [145] speculated that SERR evolves linearly with applied strain, ε. In this manner, the interfacial friction coefficient, μ_i, and G_{ic}^{II} (the debond crack growth takes place when the SERR $= G_{ic}^{II}$) can be jointly determined by parametrical variation of μ_i on SERR-ε numerical solutions. Using the SFFT (GF-epoxy) data of Kim and Nairn [146], the BEM model led to $\mu_i = 1.0$ and $G_{ic}^{II} = 12.12$ J/m^2 [145], while Kim and Nairn model [146] (based on [147]) determined that $\mu_i = 0.01$ and $G_{ic}^{II} = 120$ J/m^2.

It is peculiar that the two models identify widely different parameters despite using the same raw data, whereas both approaches incorporate Poisson's effects as well as frictional and residual stresses. In pursuit of a practical approach for more explicit identification of the interfacial parameters, Sørensen [148] developed a simple 1D SLM that determines the interfacial fracture energy and frictional sliding shear stress using the documented applied strain, debond length, and opening displacements of the fragment ends in the SFFTs. Using the potential energy approach of Budiansky et al. [149], Sørensen [148,150] considered friction and residual thermal stresses but dismissed the effect of matrix plasticity. Consequently, a more inclusive model that incorporates all relevant interfacial and material features is required to investigate the detailed stress transfer attributes of the constituents.

3.1.5. Numerical methods

Overly simplified perfectly-bonded or fully-debonded models disregard realistic debonding and pull-out mechanisms. The majority of the existing analytical interface models, such as Cox's SLM, assume a well-bonded condition and no interfacial friction ($\mu_i = 0$). These assumptions lead to overestimated IFSS and IFFT values. A more accurate interfacial analysis asks for the addition of a third state between full-bonding and debonding states. The cohesive zone model (CZM) introduces partial-debonding as an intermediate state when stiffness degrades [151]. For the CZM, compared to the fracture toughness, it is less straightforward to determine damage onset and penalty stiffness (K_i) parameters for FE modelling. The cohesive strength is difficult to determine from experiments and is usually assumed based on mesh size considerations [152–154] as a compromise between computational efficiency and numerical accuracy [155]. K_i is a numerical parameter employed to preserve the inter-ply connection prior to delamination initiation [156–158] and is vital in FE modelling [159]. Selecting an appropriate value for K_i is essential to ensure that it does not significantly alter the overall compliance of the structure or lead

to non-convergence issues [152]. However, a value within the acceptable range, which balances numerical accuracy and feasibility, have been found to affect numerical predictions [159,160], particularly under mixed-mode loading [161,162]. Fig. 9 illustrates the traction-separation law, with several common softening laws, required to establish a CZM. Based on the stress concentration around a fibre break in an SFFT, Budiman et al. [151,163] linked the photoelastically observed matrix stress contours to the IFSS. Using an axisymmetric elastic FEM and iterating the simulation with various interfacial properties (μ_i, IFSS, IFFT and K_i) for the studied CF-epoxy system, the resulting stress contour can match the experimental stress contour [151]. The discrepancy between their FEM-predicted IFSS and IFFT values and the predictions of CKT and an energy-based model [164] was justified by disregarding debonding and frictional energies in the analytical models, respectively. The key benefit of their method is that only a single fibre break is required to evaluate IFSS. This reduces the matrix plasticity effect, whereas the CKT approach requires saturation [151,163].

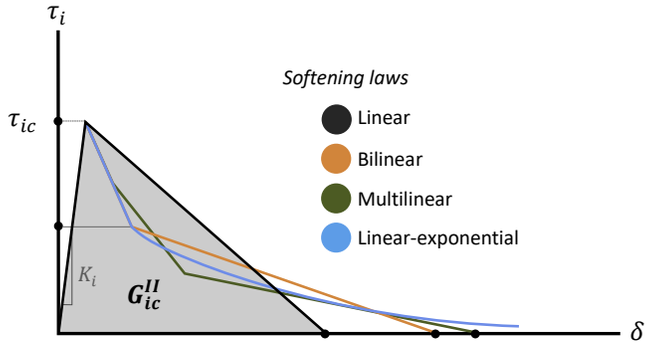

Fig. 9. Cohesive zone model for mode II fracture with various softening laws (inspired by [165]*).*

Based on an axisymmetric single-fibre FEM [151], the limiting radius into the matrix beyond which no stress transfers is reported to be at least 20 times the fibre radius ($R_m/r_f \geq 20$) to avoid the radius ratio effect. Different features and phenomena were considered in various numerical models. Varna et al. [166] considered the residual stresses in their axisymmetric FE model but adopted an elastic matrix. For a material system consisting of CF-epoxy, Nishikawa et al. [101] included matrix plasticity, debonding and matrix cracks but neglected the effect of thermal residual stresses and interfacial friction. Graciani et al. [82] used the BEM and included the interfacial friction and thermal residual stresses but neglected matrix plasticity. Recently, Van der Meer et al. [102] assessed the authenticity of the simplified shear-lag assumptions, including constant friction, non-interactive debond zones (no interaction between different fibre breaks) and neglected plasticity in a simulated GF-epoxy SFFT. Their numerical results revealed the absence of debonding interactions and the insignificance of the matrix plasticity in the debonding process. In addition, for an excessively non-linear matrix material, the fibre strain was found to lose its proportionality to the applied stress. Therefore, it is highly recommended that the l_d is monitored as a function of the applied strain rather than the applied stress [102]. Reportedly, the constant frictional stress assumption in debonded regions upholds only in the presence of matrix plasticity in the numerical models [102].

The SLM is widely employed for calculating the ineffective length (twice the length at which 90% of the broken fibre stress is recovered) and/or SCFs in FRPs. SCF is the relative increase of the cross-sectional average stress, $\bar{\sigma}_z$, at $z = z^*$ with respect to the average far-field stress (at $z = L$) ($\mathrm{SCF}_{z=z^*} = \frac{\bar{\sigma}_z(z=z^*)-\bar{\sigma}_z(z=L)}{\bar{\sigma}_z(z=L)} \times 100\%$) [167]. Green's function [168] and FEM [169] methods have been compared with SLM for their competence in stress transfer analysis. SLM is computationally less expensive than FEM, owing to its simplified portrayal of the constituents. However, its accuracy is limited to the systems with a high E_f/E_m ratio and high V_f. Compared to FEM, the ineffective length is well-estimated by the SLM. However, the predicted SCFs from SLM and FEM are only identical for a high E_f/E_m ratio and high V_f since SLM ignores the matrix load bearing capacity, its plasticity and the shear deformation of the fibre [169].

A new interface model based on continuum damage mechanics was established to investigate interfacial debonding in CF- and GF-epoxy composites in 2D [170]. The discrete element method (DEM), developed initially to model movements within granular media [171], has been extended to laminated FRPs and interfacial debonding issues [172–174]. To better describe the post-failure frictional behaviour [174], 3D DEMs were conceived. Recently, a 3D DEM with an interfacial cohesive contact model was developed based on experimental SFFTs [175]. The novel 3D FEM of AhmadvashAghbash et al. [176,177] considers the significant interrelated phenomena during CF-epoxy debonding, including thermal residual stresses, frictional sliding, matrix crack and matrix plasticity, and does not pre-impose the debond length (see Fig. 10). Their predicted stress recovery profiles were verified versus those obtained with Raman spectroscopy. Using this 3D FEM, a reliable simulation of a debonding single-fibre can be tailored to multi-fibre models, whereas the improved accuracy of the stress concentration factor predictions enables generating authentic numerical fibre break models and optimising composites at fibre level for a preferential behaviour.

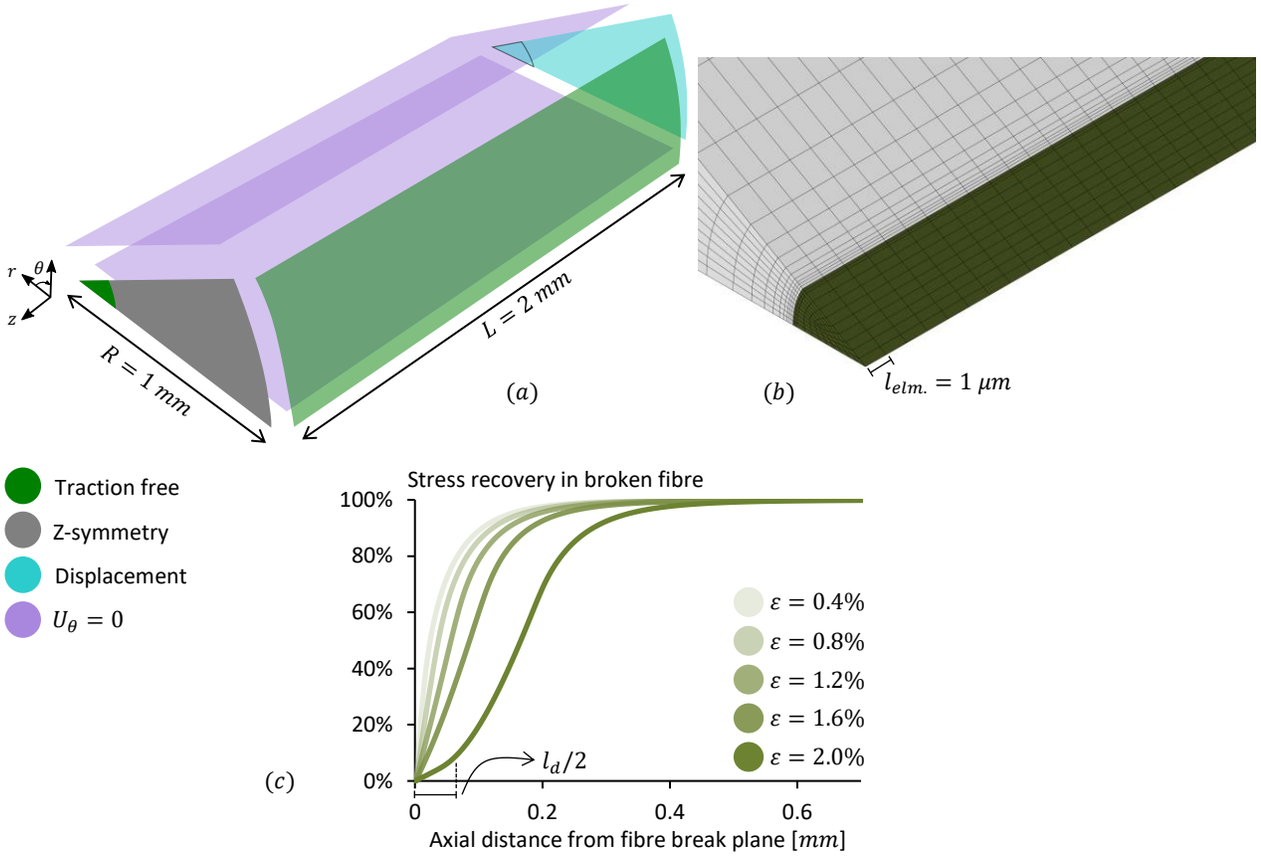

Fig. 10. 3D FE model of single-fibre debonding model: (a) reduced wedge model (due to symmetry) and assigned boundary conditions, (b) mesh refinement biased towards the interface and the debonding zone, and (c) predicted stress recovery profile for the broken fibre throughout the applied strain of 2%. Note that the indicated half-debond length corresponds to the extent of the initial linear segment of the stress profile (reprinted from [176]*, with permission from Elsevier).*

3.2. Experimental characterisation techniques

3.2.1. Laser Raman spectroscopy

A Raman spectrum can be acquired from materials that scatter light inelastically. Laser Raman spectroscopy (LRS or micro-Raman (MRS)) enables the evaluation of the stresses in CF-reinforced polymers (CFRPs) using the stress/strain dependency of certain vibrational modes of the fibres [35,178,179]. Although simplified, the following explanation helps to grasp the fundamental concepts of using LRS for conducting microstrain measurements (for further details regarding the basics of LRS

and its utilisation for strain measurements, as well as the necessary instrumentation, the interested readers may refer to [180]):

Vibrational energy states exist between the electronic states of a molecule or crystal, and when a group of atoms vibrates, it causes instantaneous changes in the electron cloud and polarisability. This periodic change in the charge distribution interacts with an external electromagnetic field, leading to various light scattering phenomena, including infrared and Raman effects. If the incoming light frequency matches the frequency of a normal vibrational state in the material and results in a dipole moment alteration, the light is absorbed, and this is how infrared spectroscopy originates. When the incoming frequency does not match a normal vibrational frequency, the material can be excited to a virtual excited state and scatter light either elastically (Rayleigh scattering) or inelastically. Raman scattering is a type of inelastic scattering. The Raman effect occurs when the molecule or crystal drops from the excited state into a normal vibration mode with either higher or lower energy than its initial state and if there is a change in the molecule's polarisability. The scattered photon's energy equals the initial energy plus or minus the molecule's vibrational energy. Various types of reinforcing fibres, including graphite, aramid, rigid rod polymer fibres, silicon nitride, and highly aligned organic fibres like polyethene, display a shift in their Raman peak when subjected to compressive or tensile strain [180]. These shifts in amorphous materials, such as CF, are mainly due to strain-induced lattice deformation, changes in the degree of disorder and interfacial debonding.

Galiotis et al. (1984) [181] were the first to adopt LRS to evaluate the strain dependency of Raman peaks in polydiacetylene fibres rather than crystals along with the Raman response of a crystalline urethane resin system [182]. Robinson et al. (1987) [179] and Galiotis et al. (1988) [178] subsequently analysed and evaluated the Raman spectrum response of various types of CFs under uniaxial stress. This was followed by a series of studies by Galiotis and his colleagues [33,180,183–185] regarding fibres embedded in polymer resins and identifying interfacial stress transfer efficiency. A review [186] of the relevant work on FRPs was presented in the 1990s. Fig. 11 displays a diagram depicting the standard LRS equipment along with strain profiles that have been fitted for both the broken and an adjacent fibre. LRS is capable of measuring the fibre stress with a spatial resolution in the order of 1 μm. The fibre is required to be positioned in the close vicinity of the model composite surface. Once the Raman spectra are taken along the fibre fragment and the maximum of a Raman band is plotted against the distance from the fragment ends, the stress or strain point-to-point variation along the embedded fibre in a matrix can be determined by evaluating the maximum of that Raman band using an appropriate calibration curve [187]. The Raman band frequency and intensity depend on the manufacturing method and the subsequent surface treatment of the fibres [178].

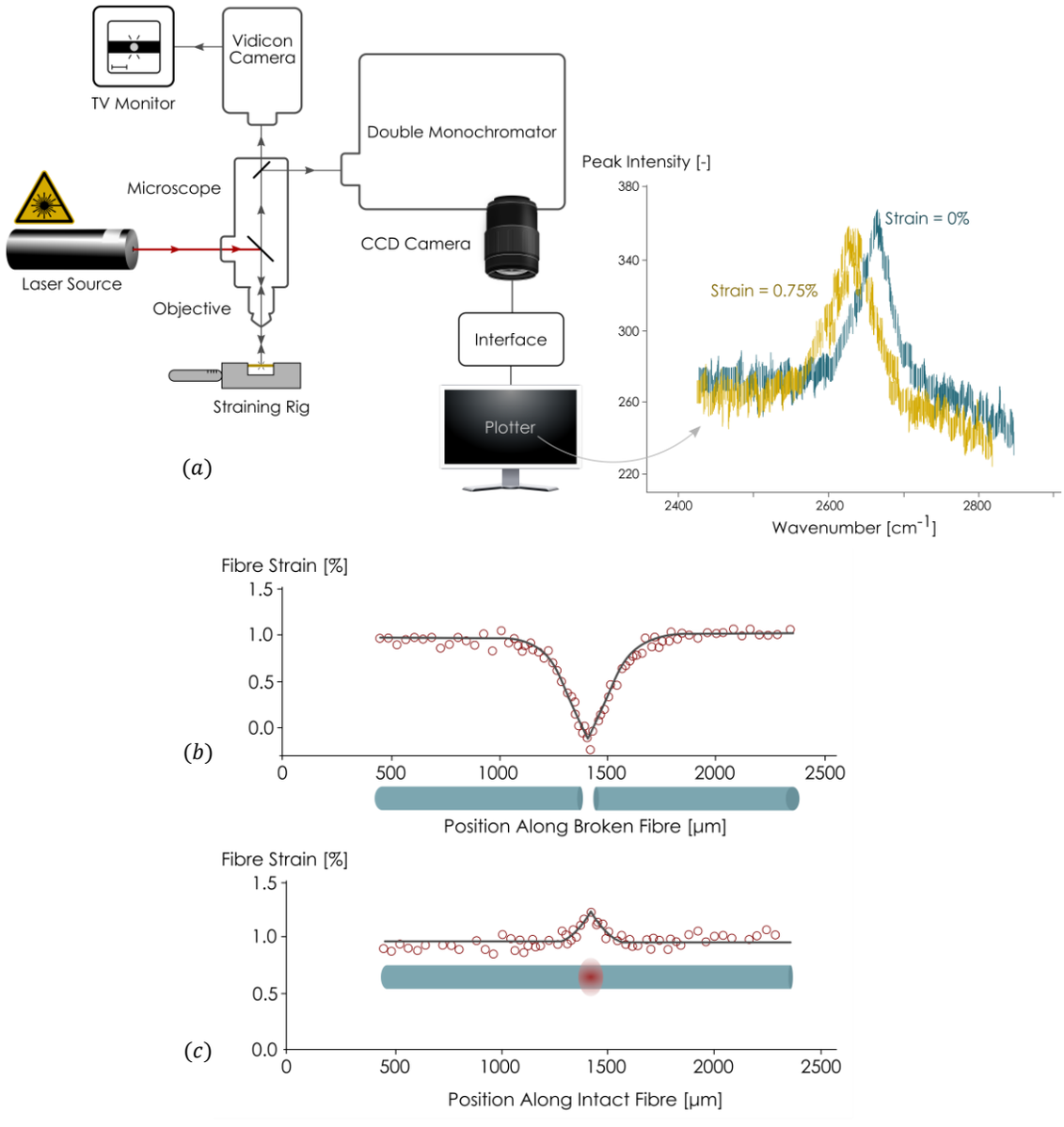

Fig. 11. (a) Schematic of standard LRS equipment (adapted from [188]*) and fitted strain profile for (b) the broken fibre, and (c) a neighbouring fibre positioned at a relatively small inter-fibre spacing of* $0.8d_f$ *in a 2D CF-epoxy microcomposite* [189].

LRS can yield a detailed understanding of the stress transfer micromechanics in SFFT. The obtained stress variation along the fibre assists in discerning between bonded and debonded interface regions and can be employed to validate fibre axial stress predictions by straightforward stress transfer models (CKT, SLM) or more elaborate ones which consider plasticity, friction, and so forth. Hence, after acquiring raw experimental data via SFFT augmented with LRS or optically assisted SFFT, estimating the interfacial properties requires using a reliable model to predict the interfacial stress transfer.

Huang and Young [39] utilised both strain-induced Raman band shifts and stress birefringence patterns during SFFTs. Their experiments confirmed that for low strain levels (pre-debonding), the fibre strain distribution follows a Cox-type SLM. Recently, Zhu et al. [190] developed an analytical model for inverse identification of all three interfacial properties: IFSS, IFFT and τ_f (compared to only IFSS and τ_f by [132]) for both micro-Raman-SFFT and the conventional SFFT data. Interfacial cohesive damage and frictional sliding were integrated into a trilinear constitutive law, and the fibre/interface analytical stress profile predictions were validated by axisymmetric linear-elastic FEM and experiments. Fig. 12 shows the fibre stress recovery profile over one-half of an untreated T50-U CF embedded in

epoxy. The partial-debonding and full-debonding models were fitted to the experimental data by [106,132]. In addition to a recent 3D FEM [176], the partial-debonding, in particular, matches well with the experiments.

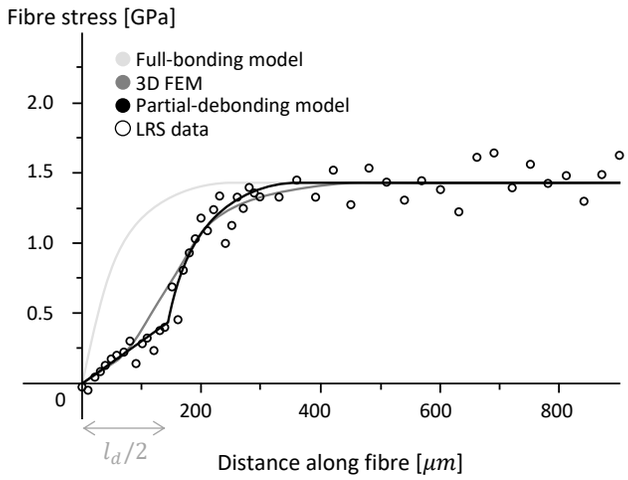

Fig. 12. Axial stress recovery profile along a T50-U fibre in an epoxy matrix at $\varepsilon_m = 0.37\%$, obtained from Raman spectroscopy [133]*, and predicted by analytical models* [106,132] *and an FEM* [176]*.*
↔ indicates half of the total debond length (recreated by the digitised data from [133] *and existent FEM results from* [176]*, with permissions from Elsevier).*

In addition to its quantitative precision in yielding fibre axial stress, another experimental advantage of the LRS approach is its application versatility. In tensile procedures for determining IFSS, as mentioned earlier, the strain-to-failure of the matrix should preferably be up to three times greater than that of the fibre to ease measurement [154]. However, for Raman-active fibres, the LRS can be employed for matrix/fibre strain-to-failure ratios much smaller than this [155], which is more indicative of engineering applications.

3.2.2. Photoelasticity

Polarised light can be used to monitor the *in-situ* fragmentation process. Since the epoxy resin is stress-birefringent, cross-polarisers enable the observation of the stress state near fibre breaks and the interface [34]. A schematic illustration of a typical fragmentation test setup is shown in Fig. 13. Once the fibre breaks, the specimen exhibits birefringence colours (or photoelastic patterns) surrounding the broken fibre ends due to the developed shear stresses at the interface as a result of stress transfer from the matrix to the fibre. The tensile stress drops to zero in the break gap between the fragments, creating a zone with no birefringence. This phenomenon offers a valuable tool to observe shear strain patterns and the fracture of opaque CFs. The birefringence usually exhibits symmetric features around the given fibre break and becomes more prolonged and flatter for higher load levels (see Fig. 14b). Upon saturation, the birefringence pattern ends almost touch each other, indicating that shear stress transfer takes place over the whole fragment length and further fibre breakage is then unlikely [34].

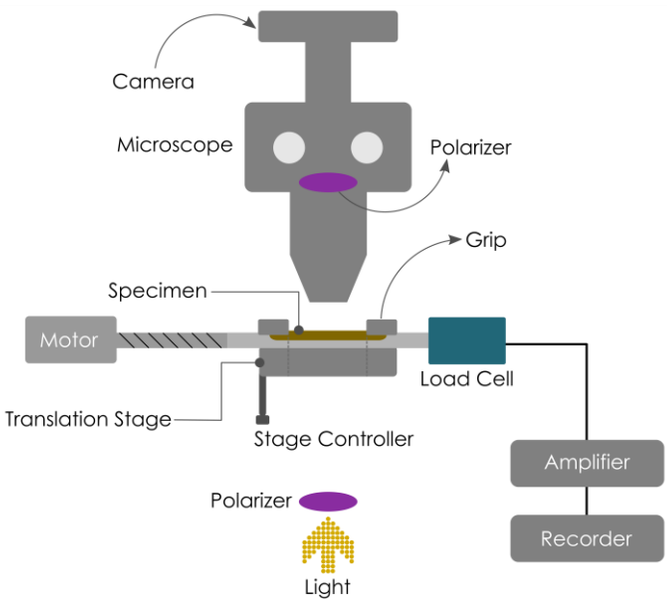

Fig. 13. Schematic feature of the fragmentation test apparatus (adapted from [83]*). The recorder displays the applied load level. Using polarisers and a camera, events such as fibre breaks, debonding, matrix cracking, and the resulting photoelasticity (or birefringence) are observable.*

Reportedly, as-received (sized) CFs display a highly concentrated birefringent pattern within the adjacent matrix [59], indicating strong adhesion. However, unsized CFs exhibit noticeable break gaps and long debonded interfaces, with some debond zones even connecting to form "chain-like" breaks. Epoxy systems exhibit extensive birefringence, which persists even after unloading the specimen (see Fig. 14c). However, in polyester matrix systems, the birefringence is less prominent and promptly disappears once the specimen is unloaded [34].

The birefringence patterns were employed to determine the debond length at each fibre break in epoxy resins in [191]. Fig. 14 compares the two expected birefringence patterns for fibre breaks with and without debonding. Based on Kim and Nairn's [191] observations, the birefringence around the fibre break includes two distinct colours, representing the inner and outer zones (see Fig. 14b). Upon unloading, the outer birefringence disappears, while the inner band remains visible (albeit contracted). The authors assumed that, throughout loading, the debond zone length was therefore equal to the length of the inner zone at the interface, as indicated in Fig. 14b. Commonly, half of the distance between the two brightest light spots observed in the photoelastic birefringence is regarded as the "experimentally measured l_d". Debond growth in an AS4 CF-epoxy SFFT is shown in Fig. 15, wherein the debond zones lengthen with an increase in the externally applied load.

Feih et al. [34] suggested an alternative definition for the debond zone extent by comparing the birefringence and white light images. The l_d in their definition corresponds to the maximum of the two colours in the birefringence pattern. Zhu et al. [190] recently showed that the shear stress field from FEM has a very similar morphology to the photoelastic birefringence. Their justification is that the photoelastic birefringence reflects the disparity between the minimum and maximum principal stresses in the material (i.e. twice the maximum shear stress). The photoelastic birefringence can therefore be analogous to the shear stress field from a fragmentation FE model.

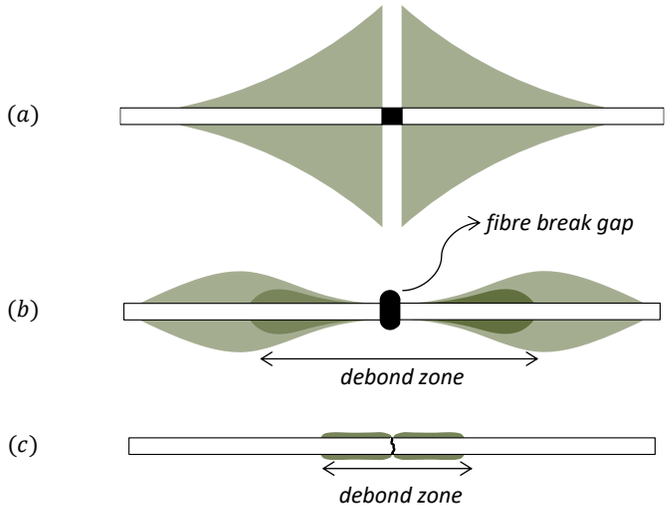

Fig. 14. The schematics of photoelastic birefringence patterns indicating the shear stress originated from an E-glass fibre break inside an epoxy matrix: (a) without interfacial debonding, (b) with debonding, and (c) unloaded state with vanished larger birefringence (redrawn from [191]*).*

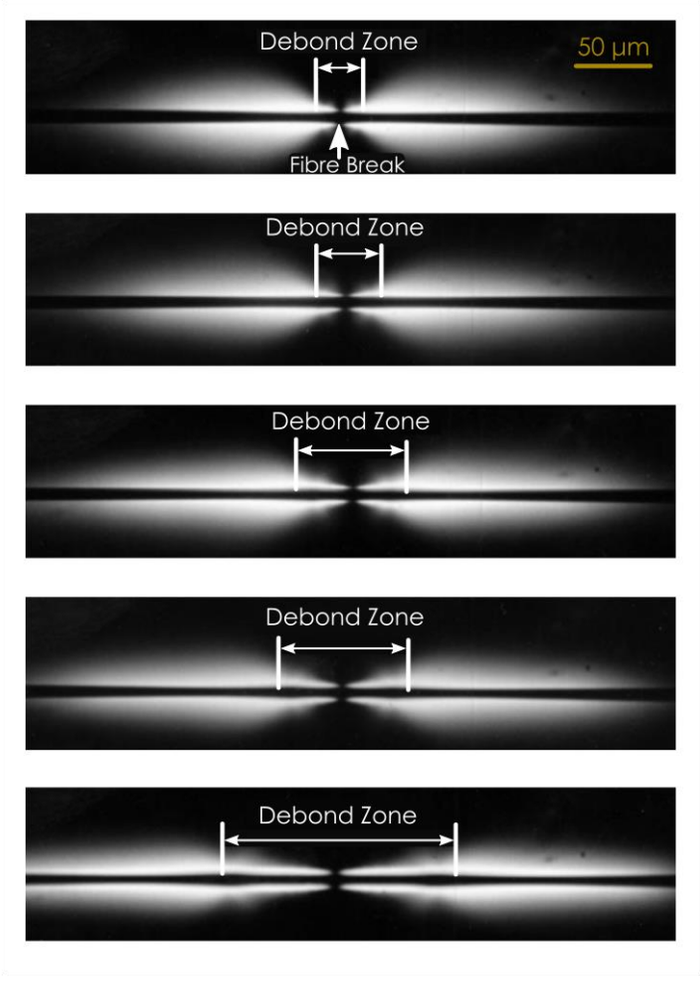

Fig. 15. Debond propagation for AS4 CF-epoxy as a function of applied strain (adapted from [83]*).*

3.3. Multi-fibre fragmentation test (MFFT)

Conducting experimental investigations on stress concentrations in neighbouring fibres resulting from fibre fracture (and accompanying matrix failure) necessitates using model composites consisting

of multiple fibres arranged in a precisely defined geometry and embedded within a matrix. Of specific significance is the requirement that the distance between adjacent fibres is limited to a few fibre diameters or less. This strict proximity criterion ensures the accurate examination and analysis of stress distribution and the intricate interplay between fibres within the composite structure. Except for the layout of testing frames and equipment, which is adjusted to ensure constant inter-fibre spacings, the multi-fibre fragmentation test (MFFT) closely mimics SFFT.

The interfibre spacing directly influences the effective stiffness experienced locally by fibres and thus impacts fragmentation length. An interfibre distance of $4d_f$ has been considered by Li et al. [192] to be insufficiently close for a meaningful stress transfer study; still, Cox model proposes a much higher ratio of $15d_f$ as a reasonable stress transfer radius. Moreover, the MFFT results of [193] demonstrated that for an interfiber spacing of 0.5-$4d_f$, the failure process of the fibre was predominantly governed by fibre-fibre interactions, irrespective of the polymer matrix properties. The increase in mean fragment length in the presence of closer fibres [192] directly contradicted the predictions of the Cox model, where a decrease in mean fragment length was expected as the matrix radius R_m decreased. It can be theorised that the efficiency of stress transfer along a fibre in a closely spaced array is less than that observed in a comparable single fibre. This inefficiency results in an effective increase in the critical transfer length. Overall, these results demonstrate the necessity in the absence of an accurate model for direct measurement for fibre fragmentation of bundled fibres since fragment length results for single fibres are not necessarily representative of those for bundled fibres.

In addition to enabling the in-situ strain measurements at the fibre level in single-fibre model composites, LRS is a valuable method for determining SCFs and also investigating the effect of the SCF on the subsequent failure process in multi-fibre model composites. The SCF and ineffective length have been measured experimentally using LRS [194–197] and are often calculated using SLMs. For instance, for 2D Kevlar multi-fibre micro-composites, the strain along the fibres was mapped, via LRS, at different load levels, and specimens with various inter-fibre spacings were utilised to investigate the effect of fibre content. The obtained experimental SCFs were compared with values predicted by different theoretical models, and in general, they aligned with the literature models that considered inter-fibre distance and matrix effects [194]. Similarly, CF-epoxy micro-composites with an inter-fibre spacing ranging from 0.8 to $19d_f$ were examined. The SCF was found to decrease from 1.26 at an inter-fibre spacing of $0.8d_f$ to 1.06 at an inter-fibre spacing of $10.4d_f$ [195]. Evidently, at relatively small inter-fibre spacings, the SCF was sufficiently high to induce further fibre failure in neighbouring fibres, leading to aligned fibre breaks. As the inter-fibre spacing increased, the decrease in SCF resulted in a reduced influence of the initial fibre break on the progressive fibre failure process, yielding a more random failure process. The experimentally measured variation of SCF with inter-fibre spacing was compared to analytical models found in the literature. However, none of the models adequately described the experimental data [195].

To obtain the maximum SCF from the experimental data, the strain profiles of the SCF in the fibres adjacent to a broken fibre, for instance, might be fitted to a Gaussian distribution function and the IFSS (using Eq. 34). A Piggott-type stress transfer model [198], consisting of two linear stress build-up regions (CKT), was found to fit the experimental strain profiles better [195]. The suggestion made by the authors [195] is to enhance the existing theories by considering the local yielding of the interface in the area surrounding the broken fibre, as indicated by the strain profiles. A preliminary FE study that included this local yielding showed encouraging outcomes [195]. Concerning the effect of the inter-fibre spacing on the interfacial shear stress at the fibre adjacent to a break, an increase in the inter-fibre spacing led to a reduction in the interfacial shear stress [195].

Grubb et al. [199] suggested that SLMs, designed to model the behaviour of single-fibre fragmentation along the fibre axis, were inherently incompetent in modelling stress transfer between fibres. Nairn's SLM [200] offers the advantage of relying heavily on parameters such as V_f and V_m as well as E_f and E_m, all of which can be determined through macroscopic methods. However, the

applicability of this model is limited to a single fibre embedded in an *infinite* matrix, and it cannot be directly extended to situations involving multiple fibres in close proximity (parallel) to each other.

Typically, the difficulty associated with MFFTs has been embedding small, brittle fibres at uniform inter-fibre intervals within a matrix [4]. Wagner & Steenbakkers [201] used a fibre spacing pin-array system, and fibres were placed between pin arrays, which were then rotated to deliver precise and reproducible interfibre distances in the eventual specimen. This approach performed well for Kevlar and other polymer fibres, but CFs and GFs broke too easily under rotation. Jones and DiBenedetto [202] employed rotating brass combs with 101 μm spacings. The interfibre spacing was controlled by adjusting the rotation angle on the device before depositing the aligned dry fibres in a silicone mould to cure. Li et al. [192] introduced another fibre-spacing tool that uses spacers to maintain fixed and settled fibre spacings. The MFFT specimens in [203] were prepared using the rotation device concept developed by Wagner and Steenbakkers [201] with modifications [204] made to achieve uniform interfibre spacings of about 1 μm. While MFFT test equipment has achieved increasingly more precise control over fibre uniaxial testing, fibre tension handling during fibre embedding is arduous due to the absence of an effective in-situ fibre local tension measurement. Additionally, the embedment process is typically manual, which introduces variability in initial fibre tension and potential undetected crazes on fibre surfaces that might trigger premature failure. Moreover, the literature lacks comprehensive consideration of the stress relaxation state of individual fibres within an array, highlighting the necessity for in-situ tension measurement during the embedment process. However, advancements in micro-actuators, sensors, and programming offer promising opportunities to overcome these challenges [4].

3.4. Conclusions

An SFFT moderately replicates the stress transfer characteristics in real FRPs and allows a large statistical interface sampling. Additionally, the critical length is sensitive to and reflects the changes in the fibre-matrix adhesion level, which is vital for a decent interface characterisation method. Fracture mechanics-based data reduction methods have been established which do not require fragmentation saturation. However, a highly complex/non-uniform stress state at the interface due to interfacial shear stress concentration near the fragment ends complicates the data analysis. Additionally, nearby fractures and fibre pre-tension integrate more difficulty into the analysis. The majority of the existing data reduction models ignore at least one of the key features of the SFFT. None of the developed approaches for SFFT has yet achieved adequate credibility to form the basis of a universal standard for the measurement of IFSS that could later be used to estimate the ILSS of a laminate [4]. An optimal data reduction method considers all the major interrelated phenomena during fibre-matrix debonding, including thermal residual stresses, frictional sliding and matrix plasticity, and avoids a pre-imposed debond length. Although it is possible to design a fragmentation test for a high V_f that roughly mimics the behaviour of a real FRP, MFFT is unable to isolate the actual intrinsic IFSS in question. As an alternative, one can pursue an SFFT that offers a more accurate estimate of IFSS but does not, as the MFFT can, capture the effects of SCFs imposed to the neighbouring fibres. The issue still lies in devising a method that strikes a balance between these two extreme circumstances [4].

The SFFT is severely limited by the elastic mismatch requirements between the fibre and the matrix. The test evaluations are consistent and reliable only if the fibre failure strain is several times lower than the matrix failure strain. The test is cumbersome to perform, and the specimen quality and success of SFFTs largely depend on the skill and experience of the operator. The process of isolating single fibres requires a high level of precision, and any errors can compromise the accuracy of the results. However, with careful preparation and attention to detail, SFFT can provide valuable insights into the mechanical properties of the interface. The key factors for the prevalence of the SFFT are the less intricate test setup and its applicability to brittle fibre systems and more frequent (relative to the other three main methods) attempts to ameliorate the data reduction methods. The SFFT is more suitable for CFRPs due to the small diameter and brittleness of CFs [39]. The SFFT, the only test involving fibre breakage while

assessing the interfacial properties, is restricted to transparent or highly-translucent matrices with high failure strain. However, acoustic emission can be used to determine the length distribution of the fibre fragments, even for specimens with opaque polymer matrices and fibrillar fibre breaks [205]. The majority of the *in-situ* measurements of the fibre strain and debond length in SFFTs are acquired either by optical microscopy, photoelastic birefringence patterns (using polarisation filters) or LRS. The key advantage of LRS-derived axial fibre strain data is that the $\sigma_f(x)$ can be determined directly by experiment, so that neither the CKT model nor SLMs are required to calculate it [4]. X-ray computed tomography (CT), *ex-situ* or *in-situ*, for the time being, might not yield a detailed 3D representation of the interface. Nevertheless, CT, alongside other techniques, such as digital volume correlation, is an asset in scrutinising microscale 3D strain maps around fibre break(s) and more precise strain recovery lengths.

Note that the direction (tension versus compression) or type of applied loading (static versus fatigue) may affect IFSS. A comparative assessment of stress transfer efficiency in tension and compression for a CF embedded in epoxy revealed that the rate of stress transfer from a fibre break was extremely high in compression, resulting in a short ineffective transfer length compared to tension. By further loading of the system, stress was transferred in the fibre not only by interfacial shear but also by fibre-fibre contact at the compressive failure location [206]. To observe the debond growth with increasing cycles, a single-fibre specimen containing a fragmented fibre can be subjected to axial fatigue loading. Previous fatigue tests on model composites with only 2-5 fibres have been conducted, such as in reference [207]. When a simulation tool is available for debonding process, combining experimental and simulation approaches can help identify the fatigue law and its parameters for the interface being studied. This information can then be used to analyse the fatigue of UD FRPs. The approach in [208] assumes that the propagation of an individual interfacial debond follows the Paris law. This law describes the growth rate of the debond as a power-law function of the difference between strain energy release rates at the highest and lowest load levels during cyclic loading. Moreover, approaches such as analytical, FEM, and virtual crack closure techniques have been employed to analyse the debond growth in tension-tension fatigue using Paris law [18,143].

Additionally, the dependency on the load direction and specimen size is a distinct feature of thermosets matrices compared to thermoplastics. The stress-strain behaviour of macro-scale bulk epoxy resin specimens exhibits an over-reliance on the loading direction [209,210]. Performing tensile tests typically leads to a brittle behaviour [211] and, contrarily, specimens under uniaxial compression exhibit notable non-linearity and plasticity on both the micro- and macro-scale. The micro-scale shear behaviour, as the most relevant description of the matrix in SLMs, displays a similar stress-strain diagram as obtained by macroscopic compressive tests. However, there is currently no agreement on the best practice to measure the relevant epoxy constitutive properties for use in micro-scale composite models and, therefore, also on the correct constitutive model. Conceivably, a first-order approximation can be achieved by simulating the constitutive behaviour based on compressive stress-strain data through the use of a yield criterion [212,213].

Table 2.A highlights the scatter in the reported interfacial properties measured with SFFT for CF or GF (separated by a horizontal dashed line) embedded in thermosetting or thermoplastic (TP) matrices. The immense existent ranges for the reported interfacial properties have received various rationalisations. High radial compression stresses can give rise to overestimated IFSSs (especially in TP matrices, related to the higher processing temperatures). Reportedly [214], the IFSS never exceeds the shear yield strength of the matrix. However, a widely used explanation for inflated IFSSs is that the polymer layer formed with a finite thickness around the fibre surface exhibits substantially different properties from those of the bulk matrix, which was criticised in [215]. The large μ_is (an order of magnitude above the typical $\mu_i = 0.3$ [216]), for instance, were explained by a large "ploughing" effect, while the extreme frictional shear stresses at full debond were mainly observed in post-cured resins [217]. Although the μ_i is a vital input parameter for reliable interfacial FEMs, the majority of the

inspected literature data for SFFT does not directly report the μ_i. However, they often include ranges for the frictional sliding stress (τ_f), which can be used to back-calculate μ_i.

Reportedly, in the case of intermediate-modulus (IMD) FRPs, the matrix tends to yield first rather than debonding along the interface, whereas in high-modulus (HM) FRPs, debonding may occur first. However, when the CKT model is adopted for IFSS calculation, its value is approximately half of the Tresca matrix yield stress. If the LRS-derived IFSS is considered more accurate, a clear disparity arises between credible experimental data for IFSS and the calculations of a classical theoretical model, with the LRS-measured IFFS tending to be twice that of the CKT IFSS [218]. The decrease in IFSS with increasing E_f aligns with the data derived for ILSS of CFRPs, which also exhibits a decrease in ILSS with the increase in E_f of CF. However, the LRS data contradicts the trend predicted by the SLMs, where the axial/interfacial shear stress profile of the fibre is predicted to increase with E_f, thus predicting an IFSS that is too high [180]. This further underlines the inability of the SLMs to account for the effect of E_f on IFSS. Therefore, both the shear-lag and CKT models exhibit quantitative deficiencies when LRS is employed to measure the IFSS for composite systems.

4. Single-fibre pull-out test

The single-fibre pull-out tests consist of performing a tensile test on an individual fibre partially embedded in resin and measuring the force needed to extract the fibre from the matrix (see Fig. 16). This test was initially developed by Shiriajeva and Andreevskaya (1962) [219], and later modified by Favre and Perrin (1972) [220], Piggott et al. (1985) [216], and Hampe (1988) [221,222]. These modifications include adapted resin block formation for CFs, embedding a controlled, short fibre length, and using a device for the stiffness-optimised pull-out test, respectively. This test is governed by the interfacial friction coefficient, interfacial pressure (caused by curing/cooling), work of interfacial fracture, fibre embedded and free length [223]. The pull-out test is challenging to perform but competent at providing the most comprehensive data since, under proper conditions, it allows measurement of IFFT, friction coefficient and shrinkage pressure [224]. The common impediments include the handling of delicate specimens and the difficulty of observing the failure events instrumentally or visually with sufficient details [225]. This test (Fig. 16) requires only a small amount of material and can be used with both brittle and ductile matrices [226]. The analysis and interpretation of the experimental data is an elaborate task considering the various theoretical models developed for this test.

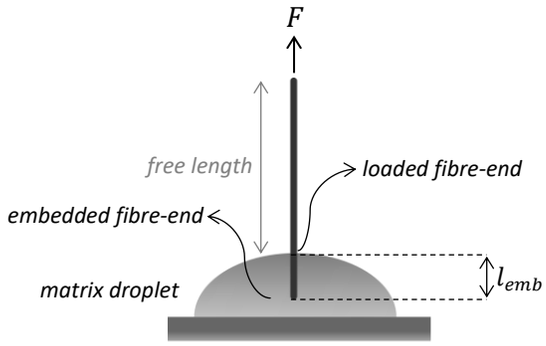

Fig. 16. Schematics of a single-fibre pull-out test, illustrating the fibre intersection on the surface of the matrix (loaded fibre-end), and its buried end (embedded fibre-end).

One of the primitive descriptions of the single-fibre pull-out test was given by Kelly in 1970 [227], elaborating on initial debonding, debond propagation, completion and fibre pull-out. Takaku and Arridge [228] clarified the dependence of the debonding and the pull-out stress on the embedded length (l_{emb}) of stainless steel wire in an epoxy resin. Although the early observations included the inception of the debond initiation and propagation along the interface, quantitative distinctions between the occurring events were not established. Instead, the maximum load, F_{max}, was used as the basis for comparison between specimens.

4.1. Load-displacement response

The pull-out load-displacement curve generally contains the typical linear elastic, crack propagation and fibre pull-out zones. According to Piggott [229], the evident regions can be distinguished in each plot as:

i. a linear increase in force with displacement;
ii. a shift in slope or a convexly curved region, indicating matrix yielding at the interface;
iii. an abrupt decrease in force due to interfacial failure; and
iv. force re-establishment and a knobbly region with decreasing force,

For the reported experiments in [229], all systems have a region (i) to a greater or lesser extent, and Kevlar-epoxy and GF and CF in thermoplastics have a distinct curved region (region ii). GF-polyester and GF-epoxy [217] have no region ii, whereas CF-epoxy does. Reportedly, all systems display a sudden decrease in force and only the systems with shorter l_{emb} (a few fibre diameters) lack region (iv) [229]. Fig. 17 shows three commonly observed force-displacement curves for the fibre pull-out test.

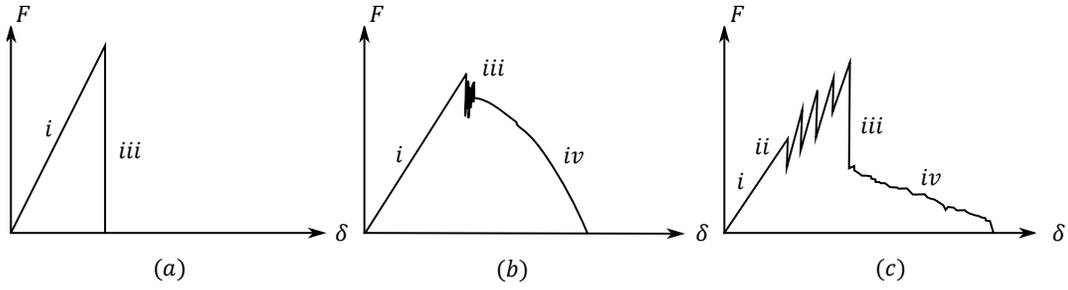

Fig. 17. Schematic illustrations of three typical force-displacement curves for the single-fibre pull-out test of brittle fibre-resin systems: (a) for strong interfaces or weak interfaces with small l_{emb}, (b) commonly observed for systems with weak interfaces, and (c) observed for Kevlar-epoxy where the peaks in the ascending region were related to friction or a stepwise debonding phenomenon (redrawn from [230]*, with permission from Elsevier).*

It is customary, although not necessarily correct, to associate F_{max} with the debonding initiation [225]. These interpretations have changed with the understanding of the damage mechanisms. It is reported that debonding initiation does not conclusively coincide with the F_{max} in the load-displacement curve [225]. However, for a catastrophic interfacial failure, that is the case. F_{cat} is a linear function of l_{emb} up to a certain fibre length, beyond which catastrophic failure would not occur, $l_{max,cat}$ (see Fig. 18). If the interfacial failure is not catastrophic, then the maximum load may represent the load required for debonding plus the frictional force over the debonded length. If l_{emb} is somewhere between $l_{max,cat}$ and $l_{max,friction}$, then there is a different relationship between l_{emb} and the maximum load. For l_{emb} greater than $l_{max,friction}$, the Poisson contraction comes into play, and thus the maximum load is independent of the l_{emb} [225].

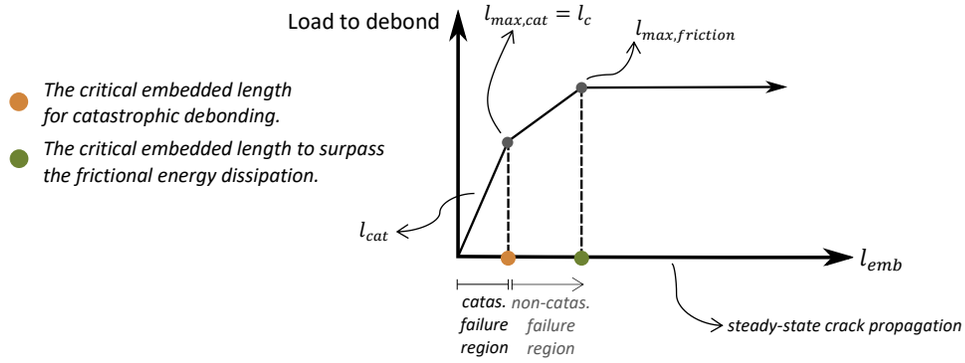

Fig. 18. Theoretical relationship between the embedded length and the load required to debond (redrawn from [225]*, with permission from Elsevier).*

The most basic model for the fibre pull-out process is the constant interfacial shear stress (linear $F_{max} - l_{emb}$), which fits reasonably well for systems with short l_{emb} (a few fibre diameters) [229]. DiFrancia et al. [225] modelled the load-displacement diagram for a single-fibre pull-out test. They showed that succeeding debond initiation, the interfacial crack initially propagates with a substantial amount of friction [225]. The frictional effect declines as the applied load increases due to Poisson contraction. The debonding reaches a steady-state at a particular debond extent, and thus the load required for crack propagation becomes constant. This steady-state debonding continues till it reaches the fibre end, followed by frictional sliding.

The apparent maximum debonding force increases with l_{emb}, which is attributed to the interfacial friction in the debonded region. The contribution of friction to the total debonding force can be as large as that of the detachment of the interface [231]. Due to stress concentrations, two possible locations exist for a debond to initiate: at the loaded fibre-end or the embedded fibre-end (see Fig. 16). In general,

embedded-end debonding occurs when E_f is much higher than E_m. Some simple criteria exist to predict which fibre-end debonds first under an axial load. Using a stress-based analysis, the embedded fibre-end debonds initially if the ratio of E_f/E_m is greater than the value of $(R_m/r_f)^2 - 1$ (R_m is the matrix radius) [232]. Similarly, the energy-based criterion of Wang [231] can be used for pinpointing the debond initiation site. The intensity of the stress singularities at the two potential debond initiation loci was compared in [233]. The results suggest that if the l_{emb} is short, debonding may occur at fibre embedded end [233,234].

4.2. Specimen design and test setup

A carefully designed experiment, in addition to IFFT, can yield data on the frictional region of the pull-out curve. Regarding the test configuration, different boundary conditions would provoke different stress states in the constituents [235]. Fig. 19 demonstrates the schematics of various fibre pull-out configurations in analytical models. Commercial devices have been developed to (partially) automate the pull-out procedure [236]. For the pull-out process, there are advantages to using a stiff loading system (including fibre grips, drivetrain, and so on) to achieve controlled and stabilised debond propagation [223]. To ensure a highly stiff test setup, the Federal Institute for Materials Research and Testing (BAM), in addition to piezo force sensors, has utilised piezo translators for precise displacement generation [222]. The components were mounted on a stiff steel frame and reported to yield stable crack propagation during the pull-out test. Often the most compliant part of the test setup is the fibre itself since a significant length of fibre (the free length, see Fig. 16) connects the embedded part of the fibre and the part in the grips. This free length mainly reduces the reliability of the post-debonding frictional data [223]. Even moderately short free lengths (a few mm) can completely eliminate the pure frictional part of the pull-out curve. Regarding the experimental settings, cross-head speed ranges of 0.2-5 mm/min [237,238], pull-out velocities of 0.01-1 $\mu m/s$ and data acquisition rates of 1 or 2 s^{-1} are reported in [222,239].

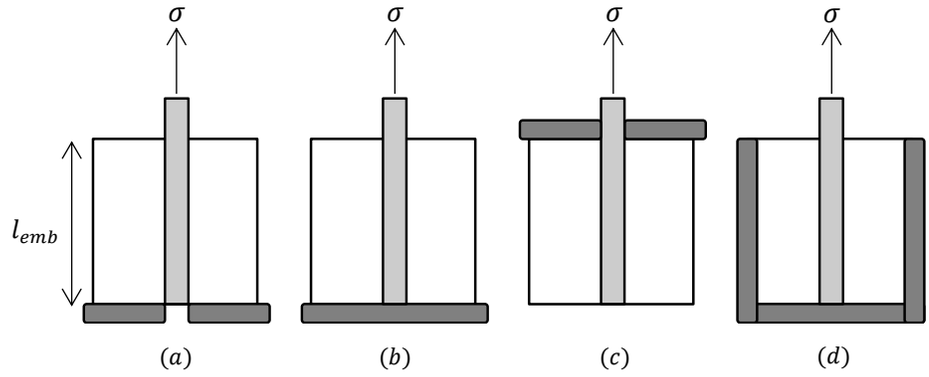

Fig. 19. Schematics of various fibre pull-out configurations in developed analytical models: (a) fixed matrix bottom, (b) fixed fibre and matrix bottom, (c) restrained matrix top [235]*, and (d) bounded bottom and sides, after Piggott* [216] *(subfigures (a-c) are redrawn from* [235]*, with permission from Elsevier).*

In a pull-out test, it is crucial that interfacial debonding occurs ahead of the fibre break. Since the interfacial debond force is directly related to the l_{emb} (positive linear relationship), there exists a maximum l_{emb} that permits fibre pull-out without breakage. This maximum l_{emb} is typically quite short, particularly for systems with small fibres and/or strong interfacial bonding. For instance, the maximum l_{emb} is generally less than 200 μm for CF-epoxy systems, posing challenges in accurately controlling the l_{emb} during specimen preparation [240]. To obtain IFSS during pull-out with high accuracy, it is necessary to have very short free lengths of fibre (e.g., ~ 1 mm for CF) [223]. However, the thermal expansions and contractions during cure (for thermosets) or melting and solidification (for thermoplastics) make the l_{emb} difficult to control to the desired degree (± 10 μm). An optical procedure to accurately control the l_{emb} and to reduce the resin meniscus formation is explained in [240].

The *in-situ* observations could include LRS [241,242] and photoelasticity (isochromatic fringe patterns) [238]. The single-fibre pull-out test was analysed for Kevlar-cold-cured epoxy using both

conventional pull-out and LRS-coupled tests in [230,243]. At low strains, the behaviour follows the elastic shear-lag analysis, but as the fibre strain increases, interfacial debonding occurs. Reportedly, the conventional pull-out test only produces an apparent IFSS value, and employing a partial-debonding model allows using the interfacial parameters obtained from Raman spectroscopy to predict the data from the conventional pull-out test [230].

4.3. Data reduction schemes

4.3.1. Stress-based methods

The stress-based models, being plainer than the energy-based approaches, target estimating the interfacial stress profile in accordance with the applied load. It is generally agreed upon that the strength approach, neglecting friction, can be applied to a totally unstable debonding process with short l_{emb}. The energy method, however, can describe stable debonding, usually with long l_{emb} [244,245]. Uniform interfacial shear stress (or mean stress model) [79] is often presumed as the first approximation. In fact, this is only valid when the matrix is fully plastic. Consequently, based on force equilibrium on the fibre, the IFSS, τ_{ic}, is:

$$\tau_{ic} = \frac{F_d}{2\pi r_f l_{emb}} \tag{2}$$

where F_d is the debond load. Greszczuk [246,247], by modifying Cox's SLM [106], derived the shear stress distribution along the fibre for an elastic matrix. The test geometry studied by Greszczuk is similar to the one considered by Piggott (Fig. 19d). The interface was assumed to be perfectly bonded (no interfacial sliding was allowed), the embedded fibre-end carried no load, and radial effects were neglected [245,246]. The non-constant shear stress along the fibre incorporates interfacial shear modulus and the effective interphase thickness, which are assumed to be G_m and $r_f \ln\left(R_m/r_f\right)$, respectively, for convenience. The IFSS, at the point of emergence of the fibre, equals to:

$$\tau_{ic} = \frac{F_d}{2\pi r_f l_{emb}} \frac{l_{emb}\sqrt{\frac{2G_m}{r_f^2 E_f \ln\left(R_m/r_f\right)}}}{\tanh\left(l_{emb}\sqrt{\frac{2G_m}{r_f^2 E_f \ln\left(R_m/r_f\right)}}\right)} \tag{3}$$

Note that R_m is the radius of the matrix involved in the shear strain. Greszczuk's analysis, possibly being the oldest, has inspired many authors [131,248] to extend this SLM for the interpretation of pull-out tests.

Lawrence et al. (1972) [249] introduced the partial interfacial debonding concept with a debond initiating at the loaded fibre-end and propagating towards the embedded fibre-end, while the effect of frictional shear stress was included throughout the debonding process. The authors recalculated the shear stress distribution to an expression analogous to that given by Greszczuk [246] but with a different elastic constant [245]. The Lawrence model predicts the debond stress satisfactorily for short l_{emb}, but tends to underpredict it as the l_{emb} increases [245].

The analytical model of Zhang et al. [250] (developed for continuous fibre-reinforced cementitious composites) divides the pull-out curve into three segments: perfect bonding, debonding, and pure friction. The matrix was considered as a rigid non-deformable body, and the constituents were isotropic and linearly elastic. Their proposed shear stress profile is reminiscent of a CZM with a bilinear traction-separation law coupled with a frictional sliding after debond completion. Sørensen and Lilholt [21] developed a relatively simple 1D analytical SLM that incorporates the residual stresses but neglects the Poisson effects. Hsueh [251,252] included the effects of interfacial debonding, residual radial and axial stresses and fibre sizing and determined the axial strains of the constituents only by the axial stresses and disregarded the effect of Poisson contraction [253]. Regarding the micromechanics of elastic stress transfer, a two-cylinder model for the single-fibre pull-out test and a three-cylinder model for the multi-fibre pull-out test were compared in [254]. This comparison revealed the importance of neighbouring

fibres (local fibre volume fraction). Concisely, none of the current and prevalent stress-based models capture all relevant features within interfacial failure in FRPs.

4.3.2. Energy-based methods

The strong heterogeneous interfacial stress distribution, exhibiting stress singularities, suggests that a stress-based evaluation of the test data is not entirely appropriate [255]. Based on Griffith's fracture criterion [256], an interfacial crack propagates once SERR (G) is just equal to the critical fracture energy release rate. The energy method includes the early work of Outwater and Murphy [257] in 1969. The basis of their work, and many to follow, was the general compliance equation expressed as:

$$G = \left(\frac{P^2}{2d}\right)\left(\frac{\mathrm{d}C}{\mathrm{d}a}\right) \tag{4}$$

where P is the load, $\mathrm{d}C/\mathrm{d}a$ the change in compliance with crack length, and d the crack width. The appeal of this type of approach was highlighted, notably by Piggott [258,259]. Initially employing a stress-based criterion in earlier studies, Piggott advocated an energy-based approach to interpret tests where brittle fracture develops. This is particularly relevant for most GF or CF-epoxy systems. The geometry used in this model is that of pull-out in Fig. 19d, in which fibre of radius r_f has an embedded length of l_{emb} within a resin cylinder with a radius of R_m. When the fibre is subjected to a tensile force, the matrix is sheared elastically. The fibre is predicted to debond at a force F_d:

$$F_d = \pi d_f \sqrt{r_f E_f G_{ic}} \sqrt{\frac{\frac{2G_m l_{emb}}{E_f \ln\left(R_m/r_f\right)} \tanh\left(\frac{\frac{2G_m l_{emb}}{E_f \ln\left(R_m/r_f\right)}}{r_f}\right)}{r_f}} \tag{5}$$

The geometry considered by Penn and Chou [260] is more comparable to that of the microbond test (in the absence of the blades, see Fig. 20). By assuming an initial interfacial crack size of length a, the energy equilibrium indicates that portion of the stored elastic energy releases to allow interfacial failure. This leads to the derivation of the debonding force, F_d, as:

$$F_d = \frac{\pi d_f \sqrt{r_f E_f G_{ic}}}{\sqrt{\left(1 + \frac{1}{\cosh\left(\cosh\left(\frac{2G_m}{E_f \ln\left(R_m/r_f\right)}\left(\frac{l_{emb} - a}{r_f}\right)\right)\right)}\right)}} \tag{6}$$

In the case where a is negligible compared to l_{emb}, this expression can be simplified as:

$$F_d = \frac{\pi d_f \sqrt{r_f E_f G_{ic}}}{\sqrt{\left(1 + \frac{1}{\cosh\left(\cosh\left(\frac{2G_m l_{emb}}{E_f \ln\left(R_m/r_f\right)}\right)\right)}\right)}} \tag{7}$$

Piggott's expression for the debond force as a function of the interfacial toughness and the l_{emb} (given in [224]) was not satisfactory since the strain energy in the fibre free length was neglected [245]. Penn and Lee [261] reformed his expression by considering the strain energy stored in the fibre free length within the energy balance equation [245]. Jiang and Penn [226] further improved the analysis by including the matrix compression contribution and the effect of the work of friction at the debonded interface in the energy balance.

The majority of energy methods assume a stable interfacial crack propagation with a constant value of the IFFT. Therefore, these approaches cannot be applied in the case of short l_{emb}, which displays an abrupt and complete debonding [245]. The important assumption of another group of models, namely the Lamé solution-based models [80,81,235,262–264], is that the axial strain in the matrix is independent of the radial distance and is approximated to an average strain in the matrix [253]. In addition, in the region near the loaded end, the stresses in both fibre and matrix are incapable of satisfying the equilibrium equation in the radial direction [253]. By extending the Lamé solution for a 2D-axisymmetric problem to the pull-out problem, Gao et al. (1988) [80] established a fracture-mechanics-based analysis, also known as the Gao-Mai-Cotterell model. This model incorporates the effect of interfacial friction in the debonding region, Poisson contraction and initial thermal residual stresses on the stress distributions. The SERR for crack propagation is given as:

$$G_{prop.} = \frac{(1 - 2kv_f)[P - (1 + \beta)Q]^2}{4\pi^2 r^3 E_f (1 + \beta)} \tag{8}$$

The unaccustomed parameters are defined in Eq. 1.A-8.A of the Appendix.

Owing to its simplified equations and methodology in assessing the interface parameters based on experimental data, the Gao-Mai-Cotterell model is extensively exploited by other researchers. This model has been adapted to incorporate the effects of loading mode [235], fibre anisotropy [262], interfacial roughness [263] and fibre volume fraction [264]. Hutchinson et al.'s solution [81], based on the Lamé solution and considering the debond as a mode II fracture, was limited to systems featuring residual compressive stresses.

As mentioned earlier, debonding can be viewed as either complete or partial. In the case of partial debonding, the friction parameters must be considered in the pull-out analysis [245]. Accordingly, the partial debond stress was represented as a function of the debond length in [265], based on fracture mechanics. However, the expression for their debond stress was intricate, and the same interfacial parameters were obtained using a simpler model in [80], overshadowing its practicality [245].

The debonding stability is regulated by the elastic constants, the relative volume of fibre and matrix, the nature of the interfacial bonding and the l_{emb} [266]. The schematic representation of the stability state in load-displacement curves (i.e. totally unstable, partially stable, and totally stable) for the interfacial debond process is given in [266].

The shear strength-based approach of Hsueh [267] and the energy-based approach of Gao et al. [80] were compared with experimental results in [266]. In Gao et al. [80], a pre-debonded interface is modelled as a stable interfacial crack propagating with a constant interfacial fracture toughness under plane strain conditions. Both models, considering an SLM, contain the effects of friction at the debonded region and Poisson contraction by assuming that the debond propagates from the loaded fibre-end (no two-way debonding) [266]. For epoxy matrix composites, Gao et al.'s model [80] predicted the trend of maximum debond stress quite well for long l_{emb}, but it always overestimated it for systems with very short l_{emb} [245]. The expressions for partial debonding of Gao et al. [80] are summarised in the appendix of [245]. Contrarily, Hsueh's model [267] can predict the maximum debond stress for a short l_{emb}, but often a considerable adjustment was required for a better fit to the experimental results for cases with a long l_{emb}.

The model of Gao et al. [80] was later applied by Kim et al. [268] to determine the IFFT, friction coefficient and residual fibre clamping stress. A stochastic approach (Ising model combined with Monte Carlo simulation) was applicable to partial debonding, fibre breakage and matrix failure [244] in the course of a single-fibre pull-out. The energy-based models of the pull-out process can also be solved with the aid of FEM [255]. For instance, Atkinson et al. [269] calculated the energy release rate in a pull-out test using FEM.

4.3.3. Numerical methods

One of the earliest FEMs for the fibre pull-out test, based on the energy method, was developed by Beckert et al. [270]. They incorporated the thermal residual stresses, specimen geometrical features and a basic model for interfacial friction. In a perfectly bonded system, a parametric study with different fibre/matrix stiffness ratios and irregular fibre cross-sections was carried out in [271]. The effect of V_f on the stress transfer was assessed both analytically and numerically by a three-cylinder composite model (coaxial fibre, matrix and composite) in [264].

The CZM bridges the gap between the stress- and energy-based approaches. Tsai et al. [272] used a CZM-friction interface model to simulate copper fibre-epoxy pull-out. In their axisymmetric FEM [273], CZM was used to explore the effect of various interfacial parameters in a single CF pull-out test. The debonding force was found to have a linear relationship with the IFSS and fibre geometric parameters (r_f and l_{emb}), but slightly decreases with increasing initiation separation displacement (the δ that corresponds to τ_{ic} on Fig. 9). Furthermore, the influences of E_f, complete separation displacement and μ_i are reported to be insignificant [273]. Additionally, the thermal residual stresses were shown to have a significant influence on the fibre pull-out during the frictional sliding stage, leading to higher specific pull-out energies (fibre pull-out energy per unit interfacial area) [274]. This highlights the importance of using an anisotropic material property for CFs in assessing the thermal residual stresses instead of simplified isotropic properties. Also, the specific pull-out energy increases with l_{emb} (but not with r_f) due to the effect of these thermal residual stresses and interfacial friction. This observation implies that merely reducing r_f would not improve the fracture resistance [274]. Moreover, this model certifies that the apparent IFSS is not constant and decreases with increasing l_{emb} [274]. According to a recent FE model [275], the most significant factors that affected the simulated pull-out test results and the corresponding force-displacement curves were the traction-separation law parameters of mode II and the free fibre length. The simulation of the crack indicated that although mode I had an influence on crack initiation, mode II dominated the further crack propagation.

Machine learning techniques have the potential to significantly enhance the accuracy, efficiency, and automation of numerical models for interface characterisation methods. It is advisable to explore novel machine learning algorithms and techniques, develop hybrid models that integrate machine learning with conventional numerical methods, and examine the potential of machine learning in multi-scale modelling. For instance, the FEM with cohesive damage model and frictional contact for the interface was combined with Artificial Neural Network (ANN) to study the load-displacement behaviour during fibre pull-out in fibre-reinforced ceramic composites in [276]. The ANN, trained and tested using an analytical model and an FEM, can accurately predict load-displacement behaviour. By utilising a larger dataset of experimental results, the ANN can be thoroughly trained to capture the elaborate details derived from experimental observations, which otherwise are challenging to investigate through analytical models [276].

4.4. Frictional behaviour

Friction is described by two independent parameters: the friction coefficient (μ_i) and the normal stress acting on the fibre surface. The μ_i is typically assumed to be 0.3, but some values ranging from 0.01 (reported as a result of the best analytical fit to the experimental GF-epoxy results [146]) to above 1 (for analytically derived μ_i from GF-polyester pull-out experiments) have been reported [237]. The exact reason for this variation unfortunately, remains unclear. Some explanations for this, however, may include the difficulties of performing reliable measurements at the fibre-matrix scale, uncertainty on the radial compressive stresses due to residual stresses and Poisson contraction, and the lack of standardised test methods. Normal stress, σ_n, arises due to the (1) chemical shrinkage of the resin (polymerisation) during isothermal curing at an elevated temperature, (2) difference in the coefficients of thermal expansion of fibre and matrix when cooled down from either the curing temperature for thermosets or moulding temperature for thermoplastics and (3) Poisson contraction (in case of the pull-out test) or

expansion (in case of the push-out test) of the fibre. The interfacial frictional stress in the debonded region is equal to $\mu_i \sigma_n$. The chemical shrinkage of polyesters is up to 8% by volume, which is significantly larger than the 3.5-4.2% shrinkage of epoxies [277]. For room-temperature-cured resins, the thermal shrinkage is minimal and may be neglected.

Contrarily to the conventional Coulomb friction ($\mu_i = \text{constant}$), a "stick-slip" phenomenon has been observed in pull-out tests [238], where the pull-out load throughout the debonding and frictional sliding is inversely proportional to the velocity imposed at the fibre end [253]. Accordingly, the Zhang et al. [253] model uses a new friction law in the debonded region (with a rate-dependent μ_i) to determine the interfacial shear stress. Their model, by dismissing the plane strain assumption in the matrix cross-section used in the Lamé solution, provided the stress fields in both bonded and debonded regions. Through numerical analysis, their findings demonstrated a significant influence of the pull-out rate, even within a steady-state pull-out procedure [253]. Additionally, the debond initiation stress decreases with the pull-out rate, but both full debonding and initial frictional sliding stresses increase with decreasing pull-out rate [278].

4.5. Conclusions

The pull-out test can directly estimate the IFSS and provide information on friction coefficients and shrinkage pressures. Despite being an excellent choice for novel fibre-matrix configurations (e.g., fibres with interfacial topographical anchors), this method is challenging for brittle fibre systems. Apart from demanding specimen preparation and handling, this method is governed by critical embedded fibre length and is limited to maximum embedded lengths of tens of micrometres for certain systems (lower bound due to meniscus formation and upper bound constrained by fibre strength [98]). The existence of high shear stress concentration near the loaded fibre-end and lower shear stress concentration at the embedded fibre-end complicates the interfacial stress state. Another challenge associated with single fibre pull-out testing in FRPs, apart from a prerequisite thorough interpretation of the load-displacement trace, is that the interpretation varies between laboratories [225]. These interpretations have primarily centred around the maximum point in the load-extension diagram. If this maximum results from a catastrophic interfacial failure, the l_{emb} is less than or equal to the length that would otherwise serve as the crack initiation length. Using this data point for comparisons between specimens requires specific consideration of the l_{emb}. Moreover, this test provides a single data point per run, which implies time-consuming data acquisition. The small load cells and fixtures used in such tests are typically highly compliant. Consequently, machine compliance needs to be determined and explicitly included in the data analysis [279]. Several models for analysing pull-out (and SFFT) test are sophisticated and, for instance, incorporate Poisson's effects of both fibre and matrix, as well as the residual stresses [81,82,280–282]. Admittedly, due to mathematical complexity, many of these models necessitate numerical implementation. Moreover, it is often challenging to determine how model parameters can be obtained from experiments [283]. A simpler analytical model, applicable to SFFT and single-fibre pull-out, is detailed in [283].

The stress distribution of an appropriate test configuration must be similar to that in a bulk composite. For composites with brittle fibres and ductile matrices, the favoured candidate is the SFFT. Contrarily, for composites with brittle matrices, inducing failure via multiple transverse cracks, the pull-out test seems more appropriate [284]. Systems with strong interfaces entail very small critical l_{emb} ($< 100\ \mu m$), that are challenging to achieve in a pull-out test configuration. For low l_{emb}, the force required to break the adhesion at the embedded fibre-end can surpass the force necessary for debonding, rendering the test ineffective (unstable). These drawbacks have prompted the development of a variant of this test: the microbond test (see Section 4). In addition to relatively more straightforward specimen fabrication, the microbond test enables testing systems with stronger adhesion (obtaining a shorter l_{emb} of about 30 μm) [258].

Table 3.A summarises the interfacial properties from pull-out tests reported in the literature. The IFSSs estimated from shorter l_{emb} are often high and, quite frequently, higher than the shear strength of the polymer matrix [229]. Piggott's test results [229] ruled out ductile interfacial failure, even with ductile thermoplastics like PEEK. Nevertheless, pseudo-ductility was observed with thermoplastics during debonding, and an apparent constant interfacial shear stress was observed with some thermosets. However, in some cases, this constant interfacial shear stress appears to be greater than and utterly independent of that of the polymer matrix itself.

5. Microbond test

The microbond test (or MB, MBT, microdrop, microdroplet, micro-debond, microbond pull-out or single-fibre-microbond-pull-out), as a revision to the conventional pull-out test, was incepted by Miller et al. (1987) [285]. Since, for an individual test, only a minuscule proportion (droplet, microdrop) of the resin is deposited on the fibre, this method is referred to as the microbond technique. In the early years of interfacial testing, the weaker reinforcing fibres were thicker and favoured by the pull-out test. However, contemporary and commercially available thin fibres demanded the conceiving of new methods, such as the microbond test.

The microbond test enables interfacial characterisation of relatively thin fibres ($5 \leq d_f \leq 15\ \mu m$). The pull-out test is problematic for these fine fibres due to the meniscus formation, which is the outward convex shape created by the surface tension between the liquid resin and solid fibre. This phenomenon lengthens the embedded length and prompts fibre rupture rather than interfacial failure. Even for a successful pull-out test, meniscus failure is generally encountered ahead of the interfacial failure and revealed by residual resin droplet on the fibre (matrix cohesive failure preceding the interfacial debonding). Contrarily, the microbond method yields sufficiently short embedded lengths that prevent fibre failure and trivialises any meniscus failure [285,286].

The experimental procedure follows the curing of a resin droplet onto the surface of a single fibre (see Fig. 20) and then applying a constant velocity to the loading knife (also called a blade, razor blade, micro-vise, micro-vise plate, miniature grip, shearing plate or simply plate). This motion exerts a shearing force on the droplet as it moves downwards and pulls the fibre out. Alternatively, the knife can be stationary while the fibre is pulled upwards at a constant velocity. Further discussion will be held on the impact of the various parameters depicted in Fig. 20.

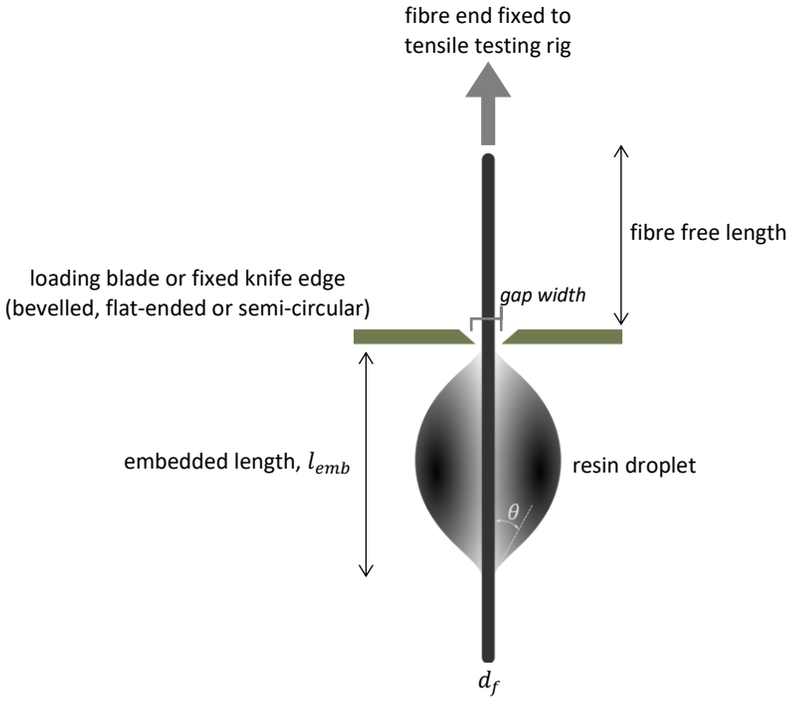

Fig. 20. Schematic of the microbond test set-up (redrawn from [287]*).*

The droplet must form symmetrically, concentrically, and ellipsoidally around the fibre to ensure concurrent contact with the knives and a uniform interfacial loading. If the contact angle is relatively low and the ratio of the droplet volume over r_f is above a critical value, an axisymmetric configuration emerges [285]. The embedded area is computed by optically quantifying r_f and l_{emb} using $A_{emb} = 2\pi r_f l_{emb}$. The presence of a meniscus region complicates the accurate determination of l_{emb}. The

discrepancy in fibre diameter measurement and the failure mode identification further complicates the test results. Moreover, unlike the pull-out test, interfacial failure in microbond specimens is reported [288] to be catastrophic, with minor or no partial debonding.

5.1. Contact angle

The surface energy of solids (and the surface tension of liquids), serving as a direct indication of intermolecular forces, encompasses Lifshitz-van der Waals (dispersive), basic, and acidic components. By considering these components, one can assess the physical adhesion between two dissimilar materials and indirectly infer their compatibility [289,290]. The fibre surface energy, as an essential physical parameter to assess surface activity, and one of the key parameters in determining the final interfacial properties, is difficult to be directly measured due to the cylindrical shape and the small diameter of the fibre. Typically, the fibre surface energy, or wettability of the matrix on the fibre surface, is determined by the contact angle (θ) of the liquid droplet deposited on the fibre surface (Fig. 20). An alternative method is inverse gas chromatography.

Carroll (1976) [291] and Yamaki and Katayama (1975) [292], concurrently and independently, developed analytical models to determine θ of the microdroplet on the fibres (as cylindrical surfaces). The microdroplet dimensions (length, L and height, H, see Fig. 23) are typically measured optically or via SEM ($L \sim 300\ \mu m$ and $H \sim 100\ \mu m$ [286]). Knowing these values and the fibre radius, θ is estimated through the corresponding Carroll's characteristic plots [291]. However, the accuracy of this method, known as the maximum drop length-height method (L, H method) [291,292], is about ±5°. To overcome the statistical errors in evaluating θ by this conventional method, the "generalised" drop L, H method [293] (also known as the tangent method or Young-Laplace fitting method), with an accuracy of ~ 0.5°-1°, was established. This numerical approach involves fitting a mathematical model of the liquid droplet shape to the actual droplet shape captured in an image. This method accounts for the effects of gravity and assumes that the droplet is symmetrical and axisymmetric, which may not always be the case. On the other hand, Carroll's method is a graphical approach that involves plotting the height of the droplet as a function of distance along the solid surface and using the resulting graph to determine the contact angle. This method is less precise than the generalised drop L, H method but is easier to use and can provide a reasonable estimate of the contact angle. The free energy functional variational method [294], with high precision for $\theta > 15°$ (cut-off error $< 0.5°$), results in angles similar to those determined by Wagner and Wiesel's numerical method [295].

To provide a visual representation, a comparison of an elliptical fit, circular arc fit, and Carroll's fit to a SEM image of a thermoplastic droplet on a sized CF is presented in Fig. 21. Carroll's equation assumes the preservation of the unduloid shape of the droplet within both its initial liquid form and after its consolidation, considering negligible gravitational effect. The droplet profile (see Fig. 22) on a cylindrical fibre is determined by the following two equations [291,296]:

$$y^2 = h^2(1 - k^2 \sin^2 \varphi) \tag{9}$$

$$x = \pm\left(ar_f F(\varphi, k) + hE(\varphi, k)\right) \tag{10}$$

The parameters definitions are brought in Eq. 9.A-12.A.

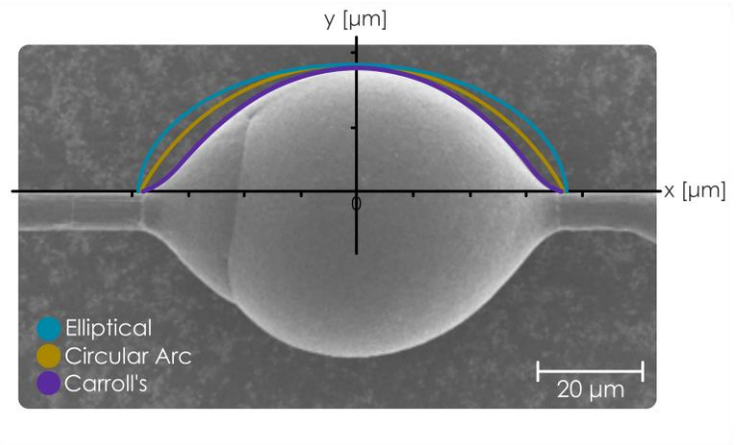

Fig. 21. Comparison of elliptical fit, circular arc fit, and Carroll's fit to SEM image of a polypropylene homopolymer droplet on an epoxy-sized CF (TR50S) (adapted from [297,298]*).*

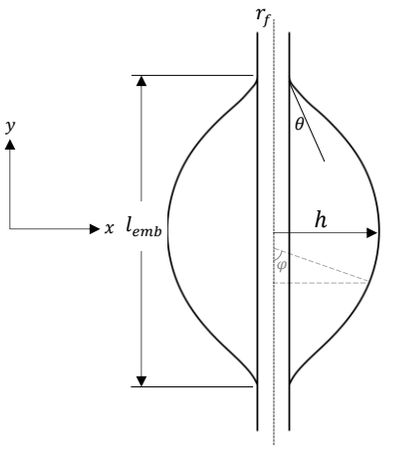

Fig. 22. Schematics of the droplet profile in a microbond test and the parameters for determination of the contact angle (redrawn from [291]*, with permission from Elsevier).*

The optical measurement of θ is typically obtained within a ±5° precision. Carroll's method [291] calculates the angle with optically observed droplet length and radius, and the r_f based on the Young-Dupre equation for a cylindrical geometry. This equation is limited to the systems with negligible gravitational forces acting upon the droplet relative to the capillary forces, which is the case for the microbond specimens having droplet dimensions of few 10 μm and viscosities of typical polymers [299]. Using Carroll's method, Mendels et al. [299] determined θ with a precision of ±0.1°.

The "debonding cone" phenomenon commonly occurs for a brittle matrix system (such as epoxy) when $\theta < 20°$. This event emerges as a residual droplet fragment, still clinging to the fibre after the droplet has been debonded [299,300]. This fragment is situated on the loading side and would result from the droplet failure due to the stress concentration at the inflexion point. The numerical model of Mendels et al. [299] anticipates a second debonding cone at the unloaded end of the fibre when the IFSS is large and the debonding is incomplete.

5.2. Specimen design and test setup

The absence of a standardised procedure for the microbond test has generated discrepancies in experimental setups among research groups, with universal testing machines equipped with low-capacity load cells being the mainstream approach. However, reliable measurement of the interfacial properties requires appropriately scaled exclusive equipment, as in [301]. In addition to having a highly stiff testing device, enabling a precise displacement measurement due to stabilised crack propagation, a shorter fibre free-length, l_{free}, is suggested to prevent the system stiffness loss based on:

$$K \propto K_f = \frac{E_f \pi d_f^2}{4 l_{free}} \tag{11}$$

where K is the slope of the force-displacement curve, K_f is the fibre free length stiffness. A compliant system conceals the nonlinearity that signals the damage initiation and destabilises the interfacial crack [302–305].

Regarding the effect of the loading device types, [306] reports higher average IFSS values (and lower scatter) utilising a pin-holed steel film over microvise tips in quasi-disk type microbond specimens. Mendels et al. [299] reported that the numerically calculated IFSS is independent of the loading point location if it is positioned in between the inflexion point of the droplet profile and the endpoint of the droplet. The inevitable discrepancies concerning the droplet configurations, as a consequence of θ variation between the two surfaces, require the shearing slit to be the narrowest. The IFSS is overestimated if the slit is too wide [288]. The coupling effect of matrix cracking and interfacial debonding was assessed using FE simulations [296]. Accordingly, if the knife-edge position is set to be around $2d_f$ away from the interface, the fibre debonds purely without significant matrix cracking [296].

Concerning the deposition of multiple droplets on an individual fibre, pragmatically, it is recommended that placing more than two droplets on the fibre complicates the droplet identification/tracking, and in the case of fibre break, all the efforts will be in vain [285]. The measured $\mathrm{IFSS_{app}}$ in a successive debonding of two microdroplets on an individual fibre, when the initial droplet debonded by the microvise is shearing the second droplet (known as droplet-droplet shearing), were identical [307].

The microbond technique is widely used for thermoset matrices but much less for thermoplastic composites. The preparation of thermoplastic droplets is, therefore, less established. An optimised method was proposed [308] using a cardboard frame with a single fibre glued to it and a rectangularly cut polymer film mounted on the fibre and melted in a convection oven. This is an alternative to those of V-shaped polymer strips [309,310], melting polymer pellets to form films and sandwiching GFs between two films [311] or knotting polymer fibre around CF [312].

Herrera-Franco and Drzal [300] provide comprehensive descriptions of the stepwise procedures for forming thermosetting or thermoplastic microdroplets. To pull the fibre out from the droplet without breaking the fibre (precondition: $\sigma_f > \tau_{ic}$), the l_{emb} range needs to be established. An l_{emb} greater than $l_{emb,c}$ (the critical l_{emb}) will result in undesired tensile failure in the loaded fibre-end. The IFSS is evaluated below this critical length which is defined as [285]:

$$l_{emb} < \frac{\sigma_f d_f}{4\tau_{app}} = l_{emb,c} \tag{12}$$

where σ_f is the fibre tensile strength. The l_{emb} is usually kept between 50 and 150 μm, proportional to the fibre's anticipated σ_f. Since the interfacial contact area is confined in the microbond test, interfacial debonding will likely occur before fibre failure [288]. For CF-epoxy, F_{max} increases with l_{emb}, however for $l_{emb} > l_{emb,c} = 120\ \mu m$ the interfacial failure was replaced by fibre failure [313]. CFs tend to rupture if the droplet size exceeds ~50% of the critical fragment length determined from the SFFT ($\sim 300\ \mu m$) [314]. Hodzic et al. [315] report l_{emb} range of 90-200 μm for 20 μm GF embedded in epoxy, while Kang et al. [313] reported the effective range to be 50-120 μm for AS4 CF-epoxy. A large l_{emb} denotes a large droplet size, abates the meniscus region effect (meniscus region maintains its size despite the enlarged l_{emb}) and approaches a quasi-spherical geometry [313].

Laurikainen et al. [301] reported that for small droplets (~50-200 μm) the debonding behaviour is catastrophic, as predicted by stress-based analytical models. If the droplet size becomes smaller, the

β^2_{Nayfeh} parameter may have to equal a negative value (for a high V_f, see Eq. 23.A or Table 1.A), and alternatively β_{Cox} can be used in stress-based models (e.g., [316]) [301]. Establishing a lower limit for the l_{emb} (e.g., 55 μm for GF-epoxy as suggested in [301]) reduces the errors associated with smaller droplets. This limit is controlled by d_f and marginally by the fibre-resin system in use.

The $IFSS_{app}$ of a microbond test can vary by more than a factor of three depending on the atmospheric conditions during the preparation [317]. Schober [317] prepared the microbond specimens in a reduced oxygen atmosphere (oven flushed with inert argon gas) to reduce the polymer degradation (manifested by the discolouration) of the PP droplets. The resulting well-formed droplets with smooth menisci and limited asymmetries yielded much higher $IFSS_{app}$ values. This indicates the need for expeditious standardisation.

The ratio of the droplet length and diameter and test speed repercussion on the measured IFSS were studied in a cylinder microbond test (droplet geometry is modified to a cylinder) complemented with *in-situ* acoustic emission monitoring [318]. Within the range of 10-100 mm/min, the IFSS was no longer altered by the test speed with embedded lengths of 120-300 μm for GF-PES system [318]. Similarly, for CF- polyphenylene sulphide (PPS), within the range of 1.2-2.4 mm/min, IFSS is unaffected by l_{emb} [312]. Zhandarov et al. [319] reported that lower test speeds of ~15 $\mu m/min$ assure a slow crack propagation. For CF-epoxy the l_{emb} range to avoid premature fibre breakage drops to 60-179 μm at a 200 $\mu m/min$ test speed (or 100 $\mu m/min$ as in [313]) [285]. The loading rate influences the contributions of viscoelasticity and plasticity to the matrix deformation. The extension rate is presumed to alter the fracture behaviour, particularly for glassy matrices possessing low shear yield stresses. A GF-epoxy system, tested at 50 $\mu m/min$ exhibited a ductile interfacial fracture, while higher displacement rates induced a brittle fracture [320].

Apart from the cylindrical droplet [318,321] (see Fig. 23), other attempts in modifying the conventional ellipsoidal droplet geometry to diminish the scatter in IFSS values include forming quasi-disk droplets (averting high interfacial stress concentrations pliant to the geometrical variations) [306,322] and forming controlled symmetrical periodic microdroplets along the fibre through Rayleigh instability [323].

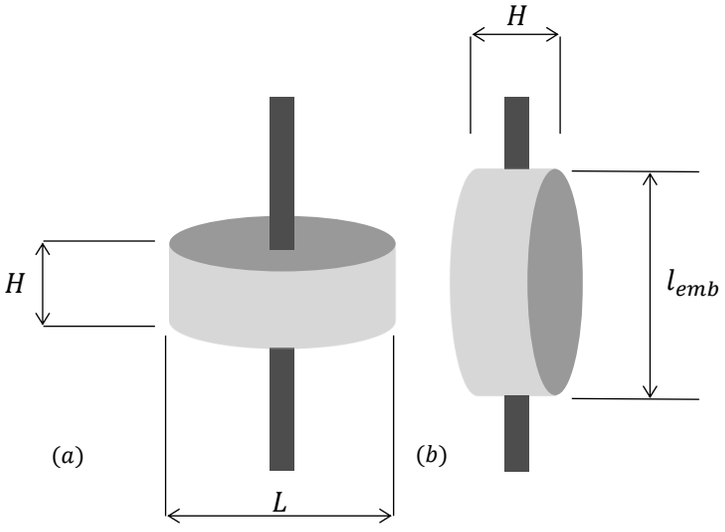

Fig. 23. A cylindrical (flattened droplet or polymeric disc) microbond specimen in which the fibre (a) runs transversely [318,321] *or (b) parallel to the droplet base* [319,324] *(subfigure (b) is redrawn from* [324]*, with permission from Elsevier).*

Despite being referred to as "microbond" test, the quantity of material contained within these microdroplets actually falls within the nanogram range, particularly when dealing with fine fibres like CF. This opens up the potential for scaling problems that can lead to unexpected and substantial disparities in the properties and performance of these droplets when compared to larger-scale specimens

even with similar thermal and environmental exposure [325]. In an infrequently referenced study, Haaksma and Cehelnik [326] noted several problems with microdroplet specimen preparation. These issues suggest potential challenges in scaling up the polymerisation process for thermosetting resins at this size. Given that the droplets were not fully cured, the researchers concluded that achieving an IFSS value was "impossible" using the cure cycle conditions employed for SFFT specimens. In the context of epoxy systems, it has been demonstrated that the performance of thin specimens undergoes notable variations in comparison to bulk specimens, primarily attributed to internal stress experienced during the curing process [327]. This observation holds relevance for both microbond and SFFT specimens. Thomason [325] elaborated on the scaling issues in the specimen preparation and data interpretation of the microbond test, for both thermosetting and thermoplastic droplets. An extensive evidence has demonstrated the strong reliance of microbond test results on the properties of the microdroplet, including its modulus and T_g. Remarkably, alterations in the properties of the droplet can exert significantly greater influences on the test results compared to modifications in the fibre-polymer interface.

Droplets exhibit lowered T_g (~ 20-60℃) below the bulk material T_g [314]), higher Young's modulus and reduced yield point compared to the bulk network. This is due to evaporation/vaporisation and diffusion of the hardener (up to 40% [314]) and/or hydrolysis of the hardener in the initial stages of curing [320]. Beam-bending experiments on conventional epoxy revealed imperceptible stresses within the curing reaction and also the initial cooldown up to the T_g. However, it induced internal stresses upon cooling below T_g [328] due to its departure from the thermodynamic equilibrium [328,329]. Contrarily, for acrylate systems, 2/3 of the total residual stresses were due to cooling above T_g [328]. The physical ageing can have a pronounced effect on the polymer viscoelastic properties below their T_g. Mendels et al. [329], comparing freshly cured and aged epoxy droplets on GFs, reported that the polymeric matrix physical ageing had no significant influence on the IFSS and IFFT in the microbond tests.

The interfacial properties are affected by cure kinetics. The volumetric shrinkage of the resin during the cool-down results in residual compressive stress on the fibre. A larger temperature difference results in higher compressive stress and hence a larger IFSS. Thomason and Yang [330] evaluated the temperature dependence of the $IFSS_{app}$ in a GF-PP system by performing the microbond test under controlled temperature in a thermo-mechanical analyser. They reported an inverse dependency of the $IFSS_{app}$ with the testing temperature, explained by the higher radial residual compressive stress at lower testing temperatures.

The effects of fibre sizing removal and the addition of coupling agents on the $IFSS_{app}$ enhancement were investigated in [287] for a range of recycled CF-PP systems. Lastly, to envision the workload, the number of tested specimens for each matrix material ranged from 50 to 151 [285,313,331], and the reported success rates were 51% (excluding the specimens that failed through fibre failure) [287], 95%, 72%, 38% for the l_{emb} = 60-99 μm, 100-139 μm and 140-179 μm, respectively [285]. This underlines the significance of controlling l_{emb} in specimen preparation.

5.3. Data reduction schemes

5.3.1. Basic approach

A simplistic apparent (also known as overall, mean, or average) IFSS is defined as:

$$IFSS_{app} = \tau_{app} = \frac{F_{max}}{2\pi r_f l_{emb}} \tag{13}$$

where F_{max} is the maximum load. Alternatively, the debond force, F_d, could be used: $\tau_{app} = F_d/2\pi r_f l_{emb}$ [331]. The $IFSS_{app}$, as a comparative identification of a weak or strong interface, assumes a constant interfacial shear stress and indicates an abrupt failure by ignoring debond propagation. The $IFSS_{app}$ decreases with increasing A_{emb}, however, the A_{emb} requires a severalfold increase to yield a

discernible reduction in the $IFSS_{app}$ values for CF- and GF-epoxy systems [307]. This was attributed to the non-uniform shearing force over the A_{emb} and its concentration within the upper part of the droplet. The dependency of this conventional $IFSS_{app}$ on l_{emb}, triggered the development of energy-based or 'local' IFSS approaches as interfacial failure criteria [331]. Fig. 24 illustrates the consecutive stages of the load-displacement diagram of a microbond test. The initiation stage detection, inferred by the slope change (stage 2 in Fig. 24), is demanding.

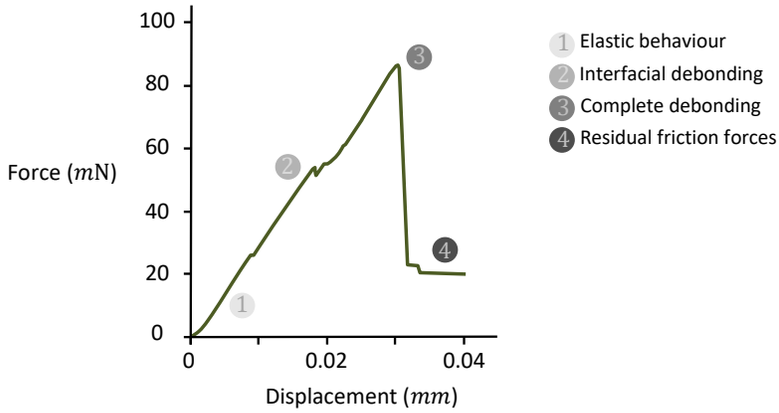

Fig. 24. A typical microbond force-displacement curve indicating the four stages of the test [332]. *The peak force at stage 3 is used to calculate $IFSS_{app}$ (adapted from* [287]*).*

In addition to the probable fibre break (leading to a sharp peak succeeded by a force drop), droplet slippage is another likely undesired incident within the experiments, displaying frictional resistance with no sharp peak on the $F-\delta$ curve [285]. Note that the initial tension, i.e. friction-induced load as the shearing plates move down the fibre prior to contact with the droplet, does not affect the calculated $IFSS_{app}$ [307].

The $F-\delta$ curves obtained by pull-out tests and microbond tests are similar, except that the length over which the frictional sliding occurs reduces over further loading in the pull-out case, while it remains constant for microbond. The initial kink between the slopes of the $F-\delta$ curve (see stage 2 in Fig. 24) indicates the debond initiation. Following the kink and preceding F_{max}, the debond propagation is stabilised by friction in the debonded regions [333]. As the crack length extends, the frictional force grows approximately proportional to the debonded area, and the cohesive contribution gradually decreases [334]. High frictional stress stabilises crack propagation [302]. F_{max} solely represents the start of the unstable crack propagation and is affected by the friction in debonded sites [303]. The strong influence of the interfacial friction on the debonding process and the F_{max} is confirmed in [302].

5.3.2. Other stress- and energy-based approaches

Reportedly [331], provided that the d_f is the same for all microbond specimens, the stress-based and energy-based failure criteria are equivalent; the discrepancy emerges only when specimens with different d_fs are compared. Zhandarov et al. [319,331,332] used a 1D SLM to investigate the applicability of the energy- or stress-based approaches for debond initiation and propagation. Scheer and Nairn [335] adopted variational mechanics analysis and a modified SLM by incorporating the thermal residual stresses. However, they assumed a frictionless interface and an elastic matrix. Accordingly, the energy-based equation for the debonding initiation stress, σ_d, was expressed by:

$$\sigma_d = -\frac{D_{3s}\Delta T}{C_{33s}} + \sqrt{\frac{2G_{ic}}{r_f C_{33s}} + \frac{\Delta T^2}{C_{33s}}\left(\frac{{D_{3s}}^2}{C_{33s}} - \frac{{D_3}^2}{C_{33}}\right)} \tag{14}$$

Rearranging leads to IFFT (the corrected version, as given in [336], includes both friction and thermal residual stresses) for debond initiation:

$$G_{ic} = \frac{r_f}{2}\left[C_{33s}\sigma_d^2 + 2D_{3s}\sigma_d\Delta T + \left(\frac{{D_3}^2}{C_{33}} + \frac{V_m(\alpha_{fT} - \alpha_m)^2}{V_f A_0}\right)\Delta T^2\right] \quad (15)$$

and the shear-lag analysis leads to [335]:

$$\sigma_d = -\frac{D_{3s}\Delta T}{C_{33s}} + \sqrt{\frac{2G_{ic}}{r_f C_{33s}}} \quad (16)$$

The interfacial friction was later included in G_{ic} in [336]. Using Eq. 13 and the equation below:

$$\sigma_d = \frac{F_d}{\pi {r_f}^2} \quad (17)$$

the IFSS_{app} becomes:

$$\tau_{app} = -\frac{D_{3s}\Delta T r_f}{2C_{33s}l_{emb}} + \frac{1}{l_{emb}}\sqrt{\frac{G_{ic}r_f}{C_{33s}}} \quad (18)$$

All the debuted parameters with their definitions can be found in the Appendix (Eq. 13.A-18.A).

The deficiency of the τ_{app} as an interfacial failure criterion is due to the dependency on l_{emb} and susceptibility to μ_i [324]). Thereby, the concept of an ultimate IFSS, $\tau_{ult} = \lim_{l_{emb}\to 0} \tau_{app}(l_{emb})$, was conceived. As a stress-based criterion, τ_{ult} factors in the stress within the matrix induced by both thermal stresses and external load [337]. The concept of local and/or ultimate IFSS was proposed by Gorbatkina and Khazanovich [338]. The local IFSS, τ_d, defined as the stress at which the local interfacial debonding occurs, is not necessarily equal to the ultimate IFSS [339,340], while some authors [337] have reported $\tau_{ult} = \tau_d$. However, near the debond tip, at the moment of debond initiation, the local IFSS equals the ultimate IFSS [284]. The main assumption is that the interfacial debonding initiates when the local interfacial shear stress at a point reaches the ultimate value (τ_{ult}). Following the ultimate IFSS criterion, shear-lag analysis with a stress-based debonding [335], the derived equations with their definitions are given in Appendix Eq. 19.A-Eq. 24.A.

Concerning the effect of friction throughout debond propagation, cohesive and frictional components of the microbond test were extracted by both stress- and energy-based criteria in [332]. Both frictional and residual thermal stresses regulate stable crack propagation. An energy-based debonding criterion ($G_{ic} =$ constant), unlike the stress-based approach, is incompatible with an unstable (catastrophic) debond propagation prediction at high debond lengths ($G_{ic} \neq$ constant throughout the test). However, post-debonding interfacial friction is best described by the energy-based approach [332].

The most eminent inconsistency between different analyses of the microbond/pull-out tests is concerned with the point where the fibre enters the matrix (see Fig. 25). A linear-elastic FEM yields a singularity at this point [341]; variational mechanics gives zero shear stress [335,342]; SLM estimations fall in between. However, a bit farther from this point, at a distance of l_m, all the three approaches yield analogous interfacial shear stress values.

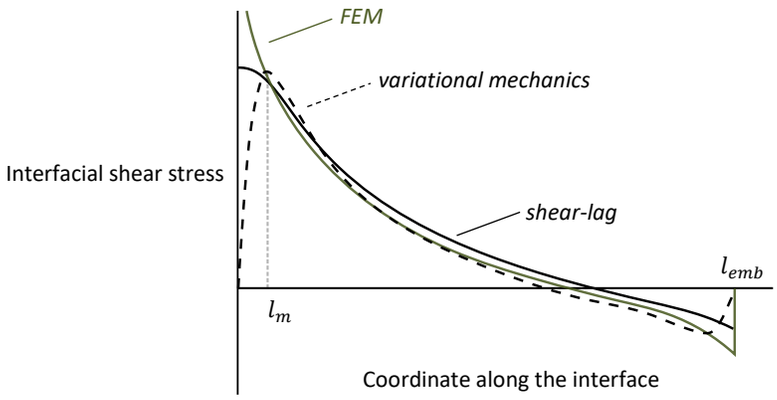

Fig. 25. Interfacial shear stress profiles along the fibre embedded length in a microbond test, predicted by three different approaches – the l_m (located at a distance of a few fibre diameters from the fibre end) is the point where the results of the three models converge ($l_m \ll l_{emb}$) (redrawn from [243]*, with permission from Elsevier).*

An alternative to the τ_{app} approach is to exploit some of the numerous analytical models established for the classical pull-out test, even though the experimental configuration is different. For a ductile interfacial fracture, the τ_{app} is reported to be uniform along the interface, thus affirming the applicability of Eq. 13 (e.g. for GF-PPS system [309]). However, according to LRS [343], photoelastic analysis [300], and FEM [304,344–346], the interfacial shear stress is not constant but varies both circumferentially and axially, and manifests a peak at a 0.1-1d_f away from the droplet top [347]**.** For a brittle interfacial failure, the shear stress diverges from the τ_{app} approach, and using the shear-lag analysis, leads to a stress-based criterion as in the work of Greszczuk [247]:

$$\tau_{ult} = \frac{F_{max}}{2\pi r_f}\sqrt{\frac{2G_{int.}}{b_i r_f E_f}}\coth\left(\sqrt{\frac{2G_{int.}}{b_i r_f E_f}}\,l_{emb}\right) = \tau_{app}\sqrt{\frac{2G_{int.}}{b_i r_f E_f}}\coth\left(\sqrt{\frac{2G_{int.}}{b_i r_f E_f}}\,l_{emb}\right) \tag{19}$$

This expression pertains to particular interface parameters, which restricts its applicability (in its current form) as these variables are typically unknown. To circumvent this issue, b_i (width of the matrix under shear stress or the interface effective thickness) and $G_{int.}$ (the interface shear modulus) are typically presumed to be $r_f \ln\frac{R_m}{r_f}$ and G_m, respectively [258]. Greszczuk's model and τ_{app} provide analogous trends. The microbond test is reported to provide mixed-mode properties and not exclusively a mode II interfacial toughness or IFSS. Consequently, energy-based approaches were preferred over stress-based models [224,347] due to severe interfacial stress field heterogeneities. Following an energy-based approach (total energy criterion, i.e. the energy per unit length equals the G_{ic}), Piggott [224] concluded:

$$F_{max} = 2\pi r_f\sqrt{E_f G_{ic} l_{emb} n \tanh\left(\frac{n l_{emb}}{r_f}\right)} \tag{20}$$

Penn and Lee [348] used a more precise energy-based criterion by considering a pre-crack (negligible compared to l_{emb}):

$$F_{max} = \frac{2\pi r_f \sqrt{r_f G_{ic} E_f}}{\sqrt{1 + \operatorname{csch}^2\left(\frac{n l_{emb}}{r_f}\right)}} \tag{21}$$

with

$$n = \sqrt{\frac{E_m}{E_f(1+\nu_m)\ln\frac{R}{r_f}}} \tag{22}$$

where R is an axial distance at which $\tau_m = 0$. However, both approaches exhibit an incomplete energy balance (residual stresses being excluded). Additionally, all the above-mentioned models inaccurately adopt a linear elastic behaviour for the droplet, leading to an overestimated G_{ic}. The theoretical analysis must be reviewed to incorporate the energy dissipation via plastic flow (e.g., via the J-integral criterion) [347]. The inclusion of residual stresses, affecting the mechanical part of the interfacial bond, must not be overlooked. The eligibility of six theoretical models (τ_{app}, Greszczuk, Piggott, Penn and Lee, Scheer and Nairn shear-lag, and variational mechanics) was investigated in [347]. The Scheer and Nairn model [335] was appointed as the most authoritative model. The quality of fitting the experimental data by energy-based approaches can be graphically appreciated in Fig. 26.

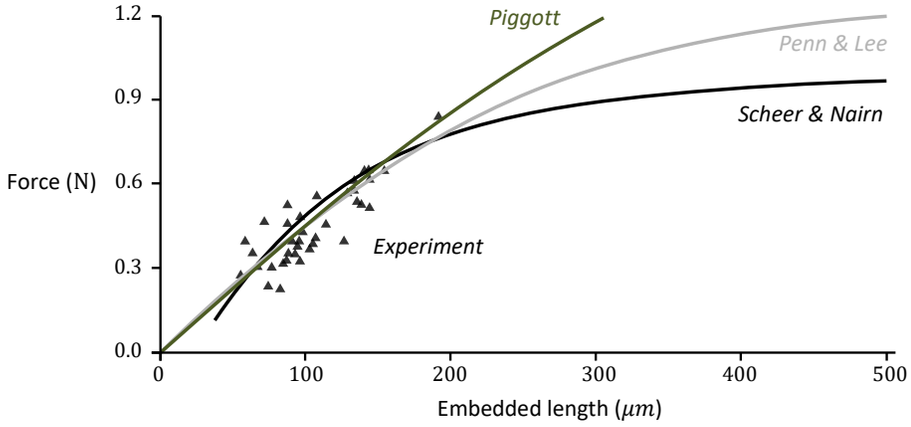

Fig. 26. Comparison of the energy-based models predictions of the force-embedded length with the experimental data for the microbond test of GF-epoxy (redrawn from [347]*, with permission from Elsevier).*

The three different methods of determining G_{ic} in a microbond test are [334]:

- the "traditional" method based on F_{max} and F_d (debonding force, see Fig. 27),
- the "alternative" method based on F_{max} and F_b (initial post-debonding force, Fig. 27),
- the "indirect" method based on F_{max} as a function of l_{emb}.

The interfacial parameters (τ_d and/or G_{ic}) and the interfacial frictional stress in the debonded surfaces, τ_f, can be determined 'indirectly' by F_{max} values. This is feasible, provided that the peak forces were recorded versus l_{emb} over an adequately wide interval of l_{emb} (e.g., $0 < l_{emb} \leq 1\ mm$ with increments of 5 μm [339,340]). Analytical models have been proposed that relate F_{max} to l_{emb} within stress-based [339] or energy-based approaches [340]. Despite providing more accurate re-calculation of the interfacial properties from old microbond (or pull-out) tests that merely contain $F_{max}(l_{emb})$, this indirect approach may be inaccurate [284]. This imprecision stems from underestimating the τ_f values, particularly when for individual specimens: $\tau_f \ll \tau_d$, and accordingly marginally overestimated τ_d values. The results acquired by force-displacement curves of individual specimen (not for a specimen set as for the indirect method) are more precise, and therefore, the indirect method is exclusively recommended when F_d and F_b are unachievable [349].

Since F_d is unaltered by the interfacial friction, it is the main experimentally obtained value whereby the τ_{ult} can be directly deduced (as in [331]). However, for some fibre-matrix systems, F_d, emerging as a 'kink' in the force-displacement curve, cannot be reliably measured since their curves yield a barely perceptible kink(s). The kink emergence requires a very stiff specimen and test set-up. An alternative method was proposed for quantifying the local IFSS [349] and G_{ic} [334] in pull-out and microbond tests. This method uses F_{max} and F_b, obviating the need for F_d. Mostly on the force-displacement curves, the transition point from debonding to post-debonding is barely perceptible. Using three different methods of data reduction schemes, Zhandarov and Mäder [349] demonstrated that the results of this new method are very similar to the traditional one. Thus, it can be recommended as an alternative technique when the F_d is indistinguishable. The "alternative" method was extended to an energy-based approach to estimate the G_{ic}, and the τ_f [334].

The τ_f (segment CD in Fig. 27), for a pull-out test can be obtained via:

$$\tau_f = \frac{F_b}{2\pi r_f (l_{emb} - l_b)} \tag{23}$$

and for the microbond test ($l_{emb} \gg l_b$), via:

$$\tau_f = \frac{F_b}{2\pi r_f l_{emb}} \tag{24}$$

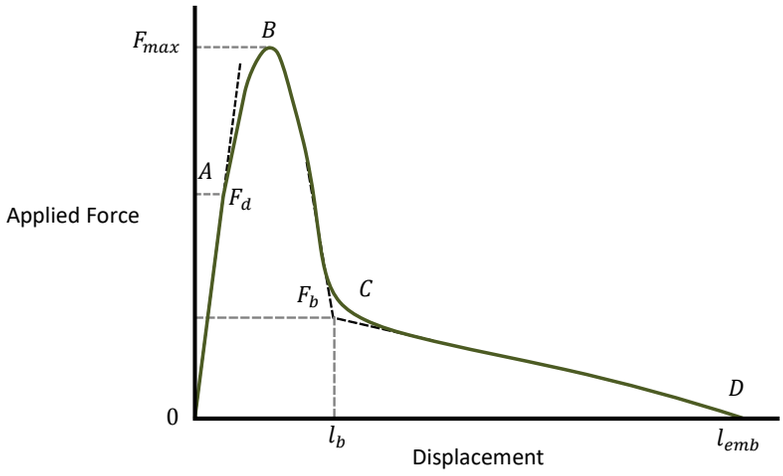

Fig. 27. An idealised force-displacement curve of a pull-out test. Segment OA corresponds to an intact interface, and the interfacial debonding initiates at A and terminates at C, while meeting the peak force at B. The 'tail' force (segment CD) is due to the interfacial friction. In the microbond test at this stage, the contact length between the fibre and the matrix is constant, and the measured force also remains constant, i.e., segment CD is horizontal (redrawn from [349]*, with permission from Elsevier).*

The typical values of τ_f are $<$ 4 MPa for E-glass-PP systems and $<$ 18 MPa for CF-PA6,6 systems [349].

Zhandarov et al. [339] assessed the correlation between the F_{max} and the l_{emb} to separately determine the interfacial adhesion and friction. The stress-based portrayal of theoretical curves of $F_{max}(l_{emb})$, accounting for the local IFSS, τ_d, and the interfacial friction, τ_f, is [316,339]:

$$F_{max}(l_{emb}) = \begin{cases} \dfrac{2\pi r_f}{\beta}\left[\tau_d \tanh(\beta l_{emb}) - \tau_T \tanh(\beta l_{emb}) \tanh\left(\dfrac{\beta l_{emb}}{2}\right)\right] \\ \dfrac{2\pi r_f}{\beta}\left[\tau_d \dfrac{u}{\sqrt{(u^2+1)}} - \tau_T\left(1 - \dfrac{1}{\sqrt{(u^2+1)}}\right) + \tau_f\left[\beta l_{emb} - \ln(u + \sqrt{(u^2+1)})\right]\right] \end{cases} \quad (25)$$

where β can be equalised to β_{Nayfeh} (see Eq. 23.A). Using the definition of $IFSS_{app}$ in Eq. 13, $\tau_{app}(l_{emb})$ is achieved as [316]:

$$\tau_{app}(l_{emb}) = \begin{cases} \dfrac{2\pi r_f}{\beta}\left[\tau_d \dfrac{\tanh(\beta l_{emb})}{(\beta l_{emb})} - \tau_{thermal} \dfrac{\tanh(\beta l_{emb})}{(\beta l_{emb})} \tanh\left(\dfrac{\beta l_{emb}}{2}\right)\right] \\ \dfrac{\tau_d}{\beta l_{emb}} \dfrac{u}{\sqrt{(u^2+1)}} - \dfrac{\tau_{thermal}}{\beta l_{emb}}\left(1 - \dfrac{1}{\sqrt{(u^2+1)}}\right) + \dfrac{\tau_f}{\beta l_{emb}}\left[\beta l_{emb} - \ln(u + \sqrt{(u^2+1)})\right] \end{cases} \quad (26)$$

with

$$u = \frac{\sqrt{\tau_{thermal}^2 + 4\tau_f(\tau_d - \tau_f)} - \tau_{thermal}}{2\tau_f} \quad (27)$$

If $\beta l_{emb} < \ln(u + \sqrt{(u^2+1)})$, the debonding is catastrophic (unstable and $\tau_f = 0$), while for $\beta l_{emb} \geq \ln(u + \sqrt{(u^2+1)})$ cases, the debond propagation is stable [316]. The effects of specimen geometry and l_{emb} on u are addressed in [316]. These theoretical curves, with two fitting parameters τ_d and τ_f and a non-linear least-squares method [339], were compared to the experimental microbond (and pull-out) data in [316,339]. Similarly, as a sequel to their work, an energy-based analysis [340] was developed, which exhibited a better fit for larger l_{emb}.

The Nairn analytical model for the pull-out and the microbond test [281], representing the $G(l_d)$ (energy release rate as a function of debonded length) is:

$$G(l_d) = \frac{r_f}{2}\Bigg\{C_{33s}\bar{\sigma}^2 + 2D_{3s}\bar{\sigma}\Delta T + \left(\frac{D_3^2}{C_{33}} + \frac{V_m(\alpha_{fT} - \alpha_m)^2}{V_f A_0}\right)(\Delta T)^2 - \left[\frac{\sigma_0}{2}\left(\frac{1}{E_{fL}} - \frac{1}{E_m}\right) + D_{3s}\Delta T\right] \times \left[kC_T(l_d) - \left(\bar{\sigma} + \frac{(1+m)D_3\Delta T}{C_{33}}\right)\acute{C}_T(l_d)\right]\Bigg\} \quad (28)$$

where

$$\bar{\sigma} = \sigma - kl_d - \frac{\sigma_0 E_{fL}}{V_f E_{fL} + V_m E_m} \quad (29)$$

with $\sigma = F/\pi r_f^2$ (tensile stress on fibre), $\sigma_0 = \sigma V_f(1-m)$ as the net axial stress and $k = 2\tau_f/r_f$ being the frictional stress transfer rate (for frictionless case: $k = 0$). A_0, C_{33}, C_{33s}, D_3 and D_{3s}, dependent on the properties of the constituents, are given in the Appendix of [281]. Although $C_{33} \approx C_{33s}$ and $D_3 \approx D_{3s}$ in many cases, it is recommended to distinguish between them [281]. For the pull-out test, $m = 0$ and for the microbond test, $m = 1$. Using an SLM, the Liu and Nairn [336] approach for evaluating the cumulative stress transfer function, $C_T(l_d)$, led to:

$$C_T(l_d) = \frac{1}{\beta_{Nayfeh}} \tanh \frac{\beta_{Nayfeh}(l_{emb} - l_d)}{2} \quad (30)$$

$$\acute{C}_T(l_d) = -\frac{1}{2}\operatorname{sech}^2 \frac{\beta_{Nayfeh}(l_{emb} - l_d)}{2} \quad (31)$$

Considering $G(l_d) = G_{ic} = const.$, the applied force as a function of the debond length [340] becomes:

$$F(l_d) = \pi r_f^2 \left[-\frac{c_1(l_d)}{2c_2(l_d)} + \sqrt{(\frac{c_1(l_d)}{2c_2(l_d)})^2 - \frac{c_0(l_d) - G_{ic}}{c_2(l_d)}} \right] \quad (32)$$

This is the corrected version which is given in [334]. The equations of $\tau(l_d)$ and $G(l_d)$ (variations of τ and G with the debonded length that build τ- and R-curves), given in [319], satisfactorily characterised the fibre-matrix interface in microbond tests [319]. Regarding the correct inclusion of V_f in these calculations, it should be pointed out that V_f depends on the l_{emb} (not in the case of cylindrical droplets) and consequently, β, $\tau_{thermal}$ and u also are functions of the l_{emb} [316]. Exclusive V_f calculations for different geometries (microbond and pull-out tests) are presented in [339].

5.3.3. Adhesion pressure

The interfacial normal (radial) strength (IFNS, σ_{ult}, σ_d, $\sigma_{rr}^{critical}$, or the adhesion pressure) as a stress-based failure criterion (considering the debond initiation to be mode I) predicts the debond initiation and the early stage of the debond propagation. Although this criterion is unsuited for larger debond lengths (mode II dominant stage) in the microbond tests [324], it provides a better estimate for the interfacial work of adhesion, W_A, if the l_{emb} is sufficiently long ($\beta l_{emb} \gg 1$) [324]. W_A is sum of the works of van der Waals (dispersion) forces and acid-base interactions, and can be measured by inverse gas chromatography [350]. In other words, W_A is the work required to separate the two neighbouring molecular layers of the fibre and the matrix, and is expressed as $W_A = \int_{-x_0}^{+\infty} \sigma_{rr}(x)\mathrm{d}x$, where x_0 is the equilibrium interatomic distance in the absence of external loads, x is the current separation between the centres of atoms in the contacting layers, and σ_{rr} is the current interfacial normal stress. This equation can be modified to $W_A = \sigma_d.\lambda$. This shows a linear correlation between the work of adhesion W_A (fundamental adhesion) and the adhesion pressure σ_d (practical adhesion) [350], with λ denoting the effective normal displacement between the contacting surfaces required for their separation (also known as proportionality coefficient, depends on the chemical nature of the constituents).

The untangled algorithm for determining the σ_d based on [335] is described in [350] for the microbond test (denoted by σ_{ult}). The σ_d (i.e. the critical σ_{rr} value at the onset of the debond initiation) reportedly depends on the specimen geometry, ΔT and the debond force, F_d [324]. By determining the σ_d from a microbond test, it is possible to estimate the W_A in actual fibre-matrix systems [350]. Some reported values for the σ_d and W_A are given in Table 1.

Table 1: Reported values for adhesion pressure and work of adhesion [350].

Fibre-Matrix System	σ_d **[MPa]**	W_A **[mJ/m^2]**
T300 CF-PA 6,6	132.4	93.3
E GF-PA 6,6	208.2	108.8
E-GF-epoxy	326	142.1

Bear in mind that the σ_d is only valid as a debond initiation criterion [243] and suggests that the debond initiation is in mode I. This is based on FEM/experimental analysis, such as [341,351] for pull-out, and also the Scheer and Nairn 3D variational mechanics (analytical expression for σ_{rr}) [335] as shown in Fig. 28.

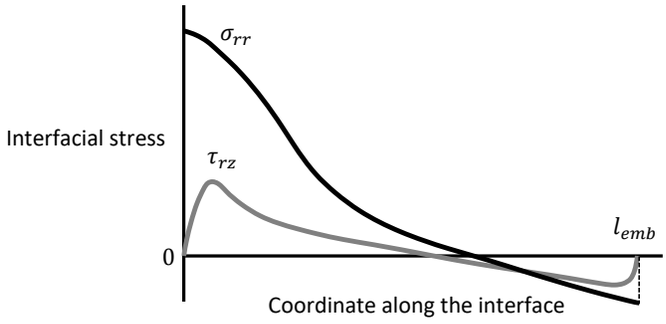

Fig. 28. Interfacial stress state along the embedded length in the variational mechanics model [335] *for the intact interface up until the debond initiation: at the point of entry, the shear stress, τ_{rz}, is zero and the radial stress, σ_{rr}, is maximum (redrawn from* [284]*, with permission from Elsevier).*

An imperfect interface (two-stage debonding) presumably occurs when there is no confined debonding front (i.e. no sharp crack tip), and the full debonding occurs after this fuzzy region formation [351]. Based on a multilinear bond law [352,353] and its modified version [354], the force-displacement curve of an imperfect interface can be modelled and compared to the experimental force-displacement curves. These models are the most comprehensive but experimentally impractical ones, as they contain an excessive number of fitting parameters (up to 5) [284].

5.3.4. Numerical methods

Theoretically, the debond initiation in the microbond test occurs in pure mode I (same as the variational mechanics approach prediction [335]: $\tau(0) = \tau(l_{emb}) = 0$), while the propagation is in a mixed mode, manifestly outweighed by mode II [335]. Reportedly, the damage initiation was in mode II and occurred in close proximity of the fibre entry to the droplet (and not at the exact entry point as predicted analytically [284]), and it was affected by the microvise opening (narrower openings cause lower initiation loads) [304]. Subsequent to the initiation, the damage promptly becomes mixed-mode and then gradually switches back to mode II near the full debond [304]. However, in the presence of thermal residual stresses, [305] reports a mixed-mode damage initiation succeeded by a mode II dominant damage propagation.

Concerning the effect of meniscus and blade separation (microvise angle) on the stress distribution, Ash et al. [286] developed an axisymmetric FE model. Rather than a cylindrical, spherical or elliptical configuration, a more accurate representation of the droplet geometry (Carroll's method [291]) was fed into the model. Altering the droplet geometry and microvise angle caused a substantial change in the stress distribution at the contact point but not much in the average IFSS. The yield zone along the interface shrinks as the gap width (see Fig. 20) widens, confirming the experimental results with overestimated IFSS values when the gap width is too wide [355].

Tailoring the droplet geometry to a cylinder (with the same volume and length), based on SLM, inaccurately describes the shear stress by reaching a non-zero value at the end of the matrix cylinder [342]. The variational mechanics approach overcame this problem by employing a cylindrical geometry and an adjustable parameter [342]. The FEM approach with either an ellipsoid [345] or a spherical geometry [300] provided a realistic representation of the interfacial stress state but was hampered by the substantial time required to generate a mesh for a droplet. Solving for interfacial shear stress, Mendels et al. [356] equivalent cylinder analytical solution was identical to the numerical discretisation of the droplet profile method if the analytical embedded cylinder length is confined to the two inflexion points of the droplet profile. Both approaches were based on a 2D stress transfer model elaborated in, similar to the Cox model but did not require any adjustable parameter [299]. The equivalent cylinder radius, R_{eq}, is:

$$R_{eq} = \sqrt{\frac{V_{droplet}}{\pi L} + r_f^2} \tag{33}$$

where the droplet volume, $V_{droplet}$, is given in [299].

Pandey et al. [346] in their 2D (axisymmetric) and simplified 3D (no interphase region) FEMs, assessed the major effects of blade separation and geometry (i.e. blade tip radius) on the interfacial stress distribution. The 2D model results in an axisymmetric stress distribution along the interface and incorrectly represents the loading by a droplet being pulled through a circular hole in a plate rather than against two blade edges (as in the 3D model). Moreover, the implemented friction between the blade and the droplet surfaces in the 3D model did not affect the stress distribution, but the maximum stress was 5% above that in the frictionless 3D model. For an elastic droplet, the 2D model was favoured over the 3D model owing to being less resource-intensive yet adequately accurate. However, for an elastic-perfectly plastic droplet case, the 2D model overestimated the stress outside the contact area [346].

Kang et al. [313] experimentally showed that the apparent IFSS increases with increasing l_{emb} (evident in the plots of F_{max}-l_{emb}, $l_{emb} \leq l_c$). Intrinsically, smaller l_{emb} (or droplet size, as a short l_{emb} represents small droplet diameters) lowers the probability of the presence of micro-defects in the stress concentration site and along the crack propagation path, thus leading to a higher strength. The interfacial shear stress profiles exhibit patterns with dual peaks and a single valley along the interface. The valley phenomenon was accredited to the minimisation of the shear stress as the tensile stress beneath the micro-vise tips shifts to compressive stress above the tips [313,321]. In their 2D axisymmetric FEM to study the interfacial shear stress distribution, a compensation factor (0.90-1.25) for τ_{app} is proposed to derive the 'real' IFSS based on the average octahedral shear stress (von Mises criterion) calculated with the distortional energy per unit volume [313].

An 'enhanced' microbond test, by integrating Fibre Bragg Grating (FBG) sensors to monitor local fibre strain, enables outputting the strain on top of the conventional test output, F_{max} [357]. For the FBG optical fibre embedded with multiple epoxy droplets of varying configurations, the accurate interfacial fracture toughness and critical traction value (for an individual droplet) can be determined by the peak strain, peak force, and the first derivative of the force-strain profile. Consequently, a bilinear CZM traction-separation law, required for the FEM interface definition, can be fitted per droplet, defined as an elastoplastic material with kinematic hardening in their 3D FEM [357]. The interfacial failure was also simulated by an Embedded Process Zone model (EPZ), based on the Dugdale assumption [358]: the maximum traction remains constant in the EPZ, i.e. uniform traction over the crack surface [296]. The EPZ is less sensitive to the FE mesh size than the bilinear CZM, which incorporates a softening behaviour after damage initiation (see Fig. 9) [359].

Schuller et al. [302], simulating the debonding by a 2D linear-elastic axisymmetric FEM, highlighted the significant effect of the interfacial friction on the peak load and crack propagation stabilisation. A comprehensive FEM, highlighting the significance of considering the thermal residual stresses and interfacial friction throughout the debond propagation and upon post-debonding, was developed in [305] with an elastic matrix and a bilinear mixed-mode CZM. Their results reveal that the F_{max} increases by extending the l_{emb}. Moreover, the frictional sliding stress increases as the thermally induced radial compressive stresses increase with the droplet length [305]. Analogously, an axisymmetric FE model with linear elastic constituents and a CZM that combines interfacial debonding, frictional sliding and their coupling was developed in [360]. It is reported that interfacial stiffness (K_i in Fig. 9), as a numerical parameter, has a significant effect on the initial slope of the force-displacement curve [360]. In their 3D FEM with a surface-based CZM and a frictional post-debond behaviour (ignoring thermal residual stresses), Minnicino et al. [304] investigated the effects of microvise opening, fibre free length and d_f on the debonding behaviour. The affecting parameters on the IFSS of a ternary composite (PES fibre-hollow glass microballoon-epoxy) are addressed through microbond testing and an FE model in [361].

To summarise, although meticulous FE models are promptly essential to the field, the recent FE models, although missing some features, have been useful in providing guidelines for practical executions.

5.3.5. Laser Raman Spectroscopy

LRS was applied to HM CF-epoxy microbond specimens (HM CF exhibits a distinct Raman spectrum), and the results were compared to those of the conventional microbond tests in [343]. The stress-induced Raman band shifts enable precise acquisition of the strain variation along the fibre embedded in epoxy. The interfacial shear stress profiles were obtained using the fibre axial strain distributions, $\varepsilon(x)$, assuming that the fibre and matrix merely undergo tension and shear stresses, respectively, as:

$$\tau_i = \frac{E_f r_f}{2}\left(\frac{\mathrm{d}\varepsilon}{\mathrm{d}x}\right) \tag{34}$$

Thereafter, the maximum interfacial shear stress obtained from LRS (τ_{max}^{LRS}), was suggested by Gu et al. [343] for interface characterisation. LRS was carried out on CF-epoxy pull-out specimens in [362], confirming that the τ_{max}^{LRS} is well-suited for interfacial characterisation.

5.4. Conclusions

The key advantage of the microbond test, apart from its applicability to almost any fibre-matrix system, is the possibility to evaluate the force upon debonding. The cohesive or adhesive nature of the interfacial failure can be ascertained via SEM examination of the fibre surface after failure. As a major drawback, the stress state in the droplet alters both with its size and the position of the contact points between the loading blades and the droplet. Moreover, the debonding force is a function of the fibre embedded length, and with thin fibres such as CF, GF, and Kevlar (d_f = 5-50 μm) the maximum viable embedded lengths are within 0.05-1.0 mm. The meniscus region severely affects the interfacial stresses, and premature failure by virtue of tensile stresses could lead to premature debonding [300]. Despite convenient sample preparation, the data reduction schemes and experimental interpretation are far more complex compared to a pull-out test due to the complications, such as mixed-mode loading state and the susceptibility to droplet shape and size, location of contact points and the knife edge gap [302].

The reliability of the F_{max}-based $\mathrm{IFSS_{app}}$ is debatable, with some authors labelling it as inaccurate [334,347]. This applies if the F_{max} from a single test is considered; however evaluating a wide range of droplet sizes and determining the slope of $F_{max} - A_{emb}$ offers a good approximation of the true interfacial properties, without requiring more complex data reduction methods [301]. Recent technical developments can facilitate more efficient and plenteous tests. For instance, a total of 1500 individual measurements with ~40 droplets deposited on each GF (overall 50 fibres) were carried out in [301] through their state-of-the-art microbond device.

Typically, the microbond method gives lower IFSS values than other test methods, such as the SFFT, as reported in [300] (26-37% less). This is explained by either meniscus failure [286] or altered droplet mechanical properties compared to the bulk polymer. The latter occurs through the loss of the curing agent (hardener) by diffusion and evaporation/vaporisation in the case of thermosetting matrices (lowered T_g, partially cured) [314]. This loss at high temperatures was reduced by prolonged curing at room temperature ahead of post-curing [314,347]. However, the microbond $\mathrm{IFSS_{app}}$ values were higher than the pull-out test results. This was attributed to the smaller embedded surface area and the dominant presence of mode II failure over mode I within debonding force [307].

Table 4.A summarises the reported interfacial properties acquired by the microbond tests. The variation in the reported properties stems from a wide range of issues, including:

- the intrinsic discrepancy of the fibre surfaces [288,307],
- the geometry of the droplet [344],
- inaccuracy of the measuring equipment (in measuring force, displacement, and fibre diameter),
- position of the loading knives (separation distance or gap width/size from the fibre surface) [288,296,355],
- loading speed [312,318],
- micro-size effects in the contact region with the microvise tip [313],
- size of the meniscus region [286,313],
- fibre-matrix contact angle [315],
- droplet cure cycle and the volatility of the hardener [314],
- fibre roving section [301],
- uncertainty in determining the embedded length (surface) [301].

At the initial stage of the pull-out or microbond tests, the failure mechanism involves normal separation (mode I) of the matrix from the fibre and a fuzzy failure front propagation [8,96,214,363,364]. Consequently, the resulting high IFSS values can conceivably be compared with the tensile strength of the polymer matrix.

It is of utmost importance to exercise meticulous caution to ascertain that any observed effects in the microbond test truly reflect the real characteristics of interface behaviour, rather than being distorted by scaling issues during specimen preparation and testing. The literature has previously documented microscale curing challenges in thermosetting resin systems even prior to the introduction of the microbond test [365]. These concerns have been acknowledged as areas for improvement in some of the earliest critical reviews of microbond [326] and micromechanical [300] testing methods. However, there has been limited substantial effort to directly address this issue, despite the growing adoption of the microbond test. Bryce et al. [366] have presented compelling evidence of substantially lower levels of curing in microdroplets of various epoxy systems. As a result, it has become impractical to perform the microbond test on specimens with identical curing histories as macroscale FRPs. For instance, obtaining representative microdroplet specimens has only been achievable through resin curing conducted under an inert atmosphere. Consequently, great care must be taken to ensure that the observed effects in the microbond test genuinely reflect the characteristics of the real material rather than artefacts stemming from specimen preparation [367].

Typically, the IFFT and friction force can be approximated from the load-crack length or load-displacement hysteresis curves in the presence of a constant friction shear stress and for load-controlled crack growth. Moreover, the results obtained for IFSS may vary due to the degradation in thermoplastics [368], relatively small changes in testing temperature [369,370] and slight variations in the stoichiometry in thermoset systems [371]. There is no singular standardised remedy for these challenges, and each fibre-matrix combination may encounter unforeseen and unpublished specimen preparation artefacts that can have a far more substantial impact on the obtained IFSS values than any material-related effects being investigated [367].

Determining a mixed-mode dependent IFFT is challenging. Reportedly [280], for the microbond test and not-too-small crack lengths, the mode-mixity remains nearly constant and corresponds to a dominating interface shear load which shifts towards mode I loading by a larger ratio of friction load to the applied load. Nevertheless, it appears that it is not feasible to modify the mixed-mode angle to a predetermined value.

6. Push-in/-out tests

6.1. Push-in test

The push-in/-out test, also referred to as fibre push-down, micro-compression, indentation, micro-indentation or nanoindentation test [372], is an *in-situ* micromechanical test for interfacial characterisation of the multi-fibre composites. This method is based on axially pushing down a single fibre over its cross-section with a micro-/nano-indenter (see Fig. 29). These indenters only differ by the size of the indenter tip (see Fig. 36) and the sensitivity of the measurement system [373]. Interfacial failure will occur due to high shear stresses, owing to the elastic and thermal mismatches between the constituents. This test is susceptible to the matrix material properties and the constraint introduced by the adjacent fibres [374] and is less frequent than the aforementioned single-fibre test methods. This test is suitable for use on actual FRP laminates, either prior to or following degradation while in service.

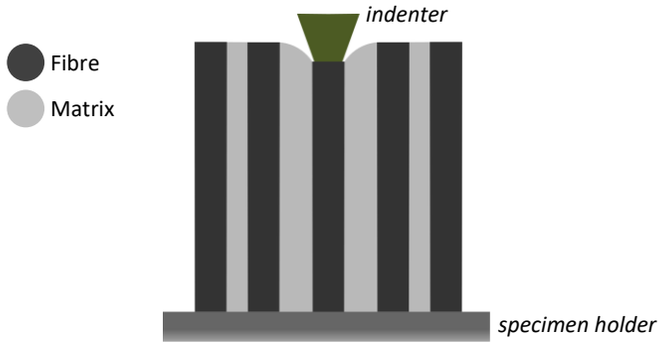

Fig. 29. Schematics of fibre push-in test.

6.2. Push-in data reduction schemes

The argument on the relevance of the interfacial testing method to a "real" composite laminate overshadows the single-fibre composite ("model" composite) tests, such as the SFFT, pull-out, and microbond tests. The interfacial stress state of the debonding fibre is affected and complexified by the presence of the neighbouring fibres. The deficient resemblance of the single-fibre tests highlights the bulk composite test methods for evaluating the interfacial parameters in the presence of the adjacent fibres.

To improve the accuracy of the push-in test, Kalinka et al. (1997) [375] designed a highly stiff test apparatus featuring an indenter with a high positioning resolution ($< 1\ \mu m$), axial displacement resolution ($< 0.1\ \mu m$), and force acquisition precision ($< 1\ m$N). They extended the original Marshall-Oliver model (1987, Fig. 30a) [376] for the continuous push-in test by including the matrix elastic energy but neglecting the matrix plastic deformation [377], as:

$$\mathrm{d}U = \mathrm{d}U_e + \mathrm{d}U_f + \mathrm{d}U_l + \mathrm{d}U_{G_i} + \mathrm{d}U_m \tag{35}$$

where $\mathrm{d}U_e$ is the change of the elastic energy inside the fibre, $\mathrm{d}U_f$ is the work of friction in the interface, $\mathrm{d}U_l$ the potential energy of the loading system, $\mathrm{d}U_{\mathrm{G}_i}$ the debonding energy associated with the new debonded area, and $\mathrm{d}U_m$ the change in matrix elastic energy. Fig. 30 demonstrates the original and the extended versions. The frictional sliding stress, τ_f, in between the debonded surfaces is:

$$\tau_f = \frac{1}{m4\pi^2 r_f^3 E_f} \tag{36}$$

and the debonding energy, G_{ic}, is calculated with:

$$G_{ic} = -\frac{\tau_f}{2}\left(u + \frac{\tau_f r_f}{2G_m}\ln\frac{r_m}{r_f}\right) \tag{37}$$

where r_f and r_m are the prescribed fibre and matrix radius, and the value of m $(= \Delta u/\Delta({F_s}^2))$ is acquired from the slope of the u against ${F_s}^2$ plot, with F_s being the shear force. An inherent challenge within the push-in tests is the direct determination of u. An indirect valuation of u can be achieved with an estimated system stiffness using the deviation from the highest slope in the force-displacement curve [375]. Pinpointing the debonding load level due to insignificant discontinuity in the load-displacement curve as debonding occurs is demanding.

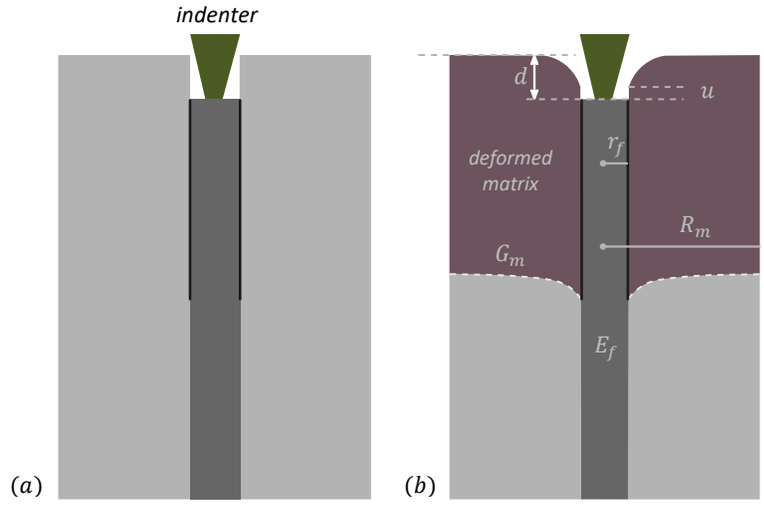

Fig. 30. Schematic diagrams of (a) the original Marshall-Oliver model [376,378,379]*, and (b) the extended model* [375]*. The parameter d is the displacement of the indenter (redrawn from* [375]*, with permission from Elsevier)*

Kharrat et al. [380] attained "reduced" indentation curves where the elastoplastic indentation of the fibre surface, u_{ep}, gets subtracted from the total recorded displacement throughout the test, u, thus:

$$u_f = u - u_{ep} \tag{38}$$

where u_f is the fibre surface displacement due to the fibre compression. The u_{ep} can be spotted by the residual mark left on the fibre cross-section (residual indentation depth) after the test and can be simply assumed to follow:

$$u_{ep} = KP^m \tag{39}$$

for loading, and:

$$u_{ep} = \alpha + \beta P + \gamma P^2 \tag{40}$$

for unloading, where K, m, α, β and γ are obtained by fitting these equations to indentation curves for bulk fibre material (bulk E-glass in their case), and P is the applied normal load [380].

In the absence of debonding, the initial load-displacement response is linear (can be confirmed by unloading at the end of the suspected range), and the transition towards non-linearity indicates debonding initiation and/or matrix plastic deformation. Following a stress-based approach, generally, a simplified SLM [380,381] can be used for analysing the results. Therefore,

$$u_f = \frac{P}{n\pi r_f E_f} \tag{41}$$

can provide the linear relation between the displacement of the fibre surface and the applied load, with n being a dimensionless parameter depending on the matrix elastic properties, the configuration, and the

constraint of the adjacent fibres (local V_f). The shear-lag analysis disregards the interfacial and matrix radial stresses and misjudges the total fibre surface area as the loaded area [382]. Accordingly, these models consider only the restrictive influence of the surrounding fibres in a basic manner. However, the neighbouring fibres are positioned in uneven patterns, and there is no solution for the stress distribution around an indented fibre in a non-axisymmetric layout. The axisymmetric models used rely on an average distance to the closest neighbouring fibres, which are generally regarded as perfectly rigid [380,381]. Therefore, the parameters derived to consider the impact of neighbouring fibres are still somewhat arbitrary [383].

Molina-Aldareguia et al. [383] proposed a micromechanical FE model of the push-in test with interfacial cohesive elements. They revealed that the prevalent analytical models are valid when the indented fibre is relatively far from the adjacent fibres ($R_e/r_f > 3$, with R_e being the distance from the indented fibre to the ring of neighbouring fibres; an obscure parameter, particularly in a real FRP with randomly packed fibres). For closely packed fibres ($R_e/r_f < 3$), the SLM overpredicts the constraining effect of the neighbouring fibres but can be appropriate if R_e/r_f and n can be determined from the initial linear part of $P-u$ curve [380,383] as:

$$n^2 = \frac{2G_m}{E_f \ln(R_e/r_f)} \tag{42}$$

or according to [384,385]:

$$n = \frac{S_0}{\pi r E_L^f} \tag{43}$$

where S_0 is the slope of the linear region, indicating elastic deformation of the fibre and matrix (see Fig. 31) and E_L^f is the longitudinal fibre modulus. The IFSS or τ_{max} can then be computed as [380]:

$$IFSS = \tau_{max}^{SLM} = \frac{nP_c}{2\pi r^2} \tag{44}$$

where P_c (occasionally denoted as P_d, the debonding load) stands for the critical load at the debond initiation. Evidently, the local stiffness (the initial slope of the loading curves) is higher for the closed-packed fibre arrangements compared to isolated fibres (at least $1d_f$ distant from the next nearest fibre) [386]. However, the IFSS obtained with this approach (classical SLM) is underestimated by a factor of ~ 2 [384]. This is particularly the case for composites with a large V_f ($> 50\%$), owing to disregarding the accurate constraint of the adjacent fibres, CF anisotropy, thermal residual stresses and interfacial friction. In their parametrical 3D FE study, Rodriguez et al. [384] were able to significantly enhance the accuracy of the push-in technique by explaining the impact of localised environment and curing stresses on IFSS measurement in a typical CF-epoxy FRP. They included all the parameters mentioned earlier in a closely packed hexagonal fibre configuration (six orderly adjacent fibres around an indented CF) and assigned cohesive surfaces to the interface. Based on their FE results and using Eq. 43 and Eq. 44, the "actual IFSS, τ_{max}^{act}" was obtained as:

$$\tau_{max}^{act} = A\tau_{max}^{SLM} - B\Delta T \tag{45}$$

where ΔT is the temperature drop due to the cool-down and A and B are fitting parameters. In their case for CF-epoxy, $A = 1.92$ and $B = 0.085\ 1/℃$ ($\tau_{max}^{SLM} \approx 0.52\tau_{max}^{act}$), indicating that the interface strength derived from P_c using the classical SLM underestimated the more precisely predicted interfacial strength (by a factor of ≈ 2) by excluding the effect of fibre anisotropy and curing stresses.

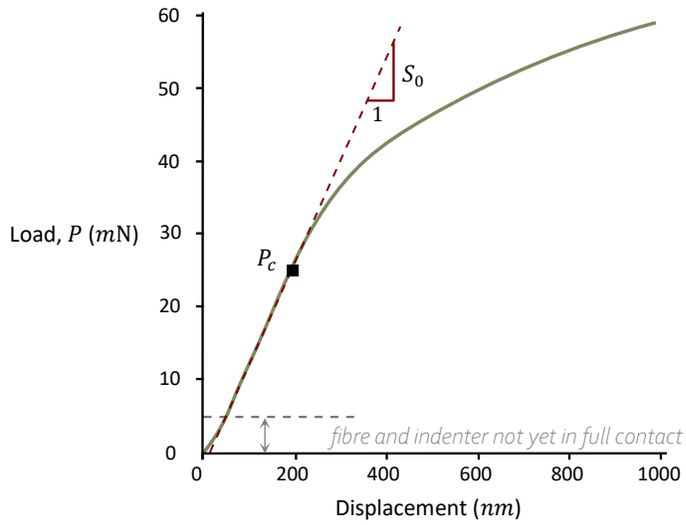

Fig. 31. Typical (ideal) load-displacement curve of a push-in test of a CF-epoxy composite. Succeeding the initial region, corresponding to the zone with imperfect contact between the indenter and the fibre, the linear segment (with stiffness S_0) is due to the elastic deformation of fibre and matrix, which terminates with the debond initiation (redrawn from [384]*, with permission from Elsevier).*

To consolidate the simplified FEM of Rodriguez et al. [384] (indented CF amid six adjacent fibres), Wang et al. [387], similarly in their 3D RVE of randomly packed fibres, assessed the effect of fibre and matrix thermo-elastic mismatches on the indentation response and the quantified IFSS. The FEM-assisted calibration of the standard SLM by including thermal and elastic mismatch leads to:

$$IFSS = \tau_{max} = \lambda\tau_{max}^{SLM} - \alpha\tau_{max,th}^{s} \tag{46}$$

where $\tau_{max,th}^{s}$ is the maximum residual shear stress. The parameter λ signifies the effect of fibre distribution and elastic mismatch, and α acts as a correction coefficient for the interfacial residual shear stress. For CF-epoxy, $\lambda = 1.39$ and $\alpha = 0.78$ ($\tau_{max}^{SL} \approx 0.72\tau_{max}^{act}$). These calibrated models provide a general approach to improve the precision of the IFSS estimation based on the standard push-in test by correcting the elastic and thermal mismatches between fibre and matrix [387]. The importance of including matrix plasticity for higher local V_f in FE models of push-in test is highlighted in [383].

Reportedly [386], for single fibre push-in for CF-epoxy composite slices of about 300 μm thick, the initial damage (possibly matrix plastic deformation) and interfacial failure did not rely heavily on the local fibre density. Moreover, the quantification of interfacial toughness is, however, difficult from the push-in tests, as the debonded area cannot be quantified at the failure loads. Tests on thinner CFRP slices (thickness ~ 30 μm) had resulted in full debonding and fibre push-out without fibre failure. However, in thicker slices, the fibres showed initial indenter imprints on their surface and the load-displacement curves exhibited an increasing hysteretic behaviour before debonding. Furthermore, analysing the cyclic load-displacement curves can furnish information on the elastic-plastic and hysteretic (debonding) energy contributions. [386].

Desaeger and Verpoest [382] examined the push-in test's credibility, limits and possibilities. Presuming that debonding occurs when the interface crack is larger than a quarter of the fibre circumference, valid experiments were those with $R_i/r_f < 0.3$, where R_i is the indentation position to the fibre centre. The debonding load was specified as the load with a debonding probability of 50% (further details of the procedure can be found in [382]). The selected debond detection technique must be substantiated alongside other methods. These methods include optical microscopy, SEM, and experiments performed by using hold segments (the indenter force is kept constant) or load-displacement

gradient [382]. The push-in test is reported to be more suitable for interfacial characterisation of high modulus/strength composites with a low fibre-matrix adhesion level and comparatively thick fibres [375]. However, for a delicate interface, such as GF-PP, SEM observations confirmed that surface polishing during sample preparation could already debond the interface [382].

It is beneficial to track and analyse the interfacial changes rigorously. A time-lapse X-ray CT scanning can elucidate the progress of composite degradation. Watanabe et al. [388] used nanoscopic synchrotron radiation X-ray computed tomography to investigate the crack initiation and propagation in CFRPs under a push-in test at a spatial resolution of 50 nm. Reportedly, the crack propagation in thin matrix regions is mainly through interfacial debonding (brittle behaviour). However, in resin-rich areas, the debond initiation and propagation are rather ductile (plastic deformation of the resin). These nanoscale mechanisms are pivotal for mechanical modelling and multiscale analysis.

6.3. Push-out test

The push-out (or push-through) test was instigated by Marshall [378] to assess the interfacial properties of ceramic matrix composites (CMC). The push-out test is to micro-indentation what the microbond test is to the pull-out test [258]. In a push-out test, an individual fibre of a thin ($\sim 50\ \mu m$) polished composite specimen is pressed down by a rigid indenter tip (see Fig. 32). This results in a force-displacement curve with an initial linear part followed by a second region with a lower slope, corresponding to elastic fibre deformation and the progressive interfacial debonding, respectively. As a third stage, a plateau emerges once the debonding is complete. Finally, the slope increases again when the indenter comes into contact with the matrix (see Fig. 33a). This test is suitable for fibres that can carry compressive loads such as GF, CF, and ceramic fibres but it is unsuitable for aramid fibres.

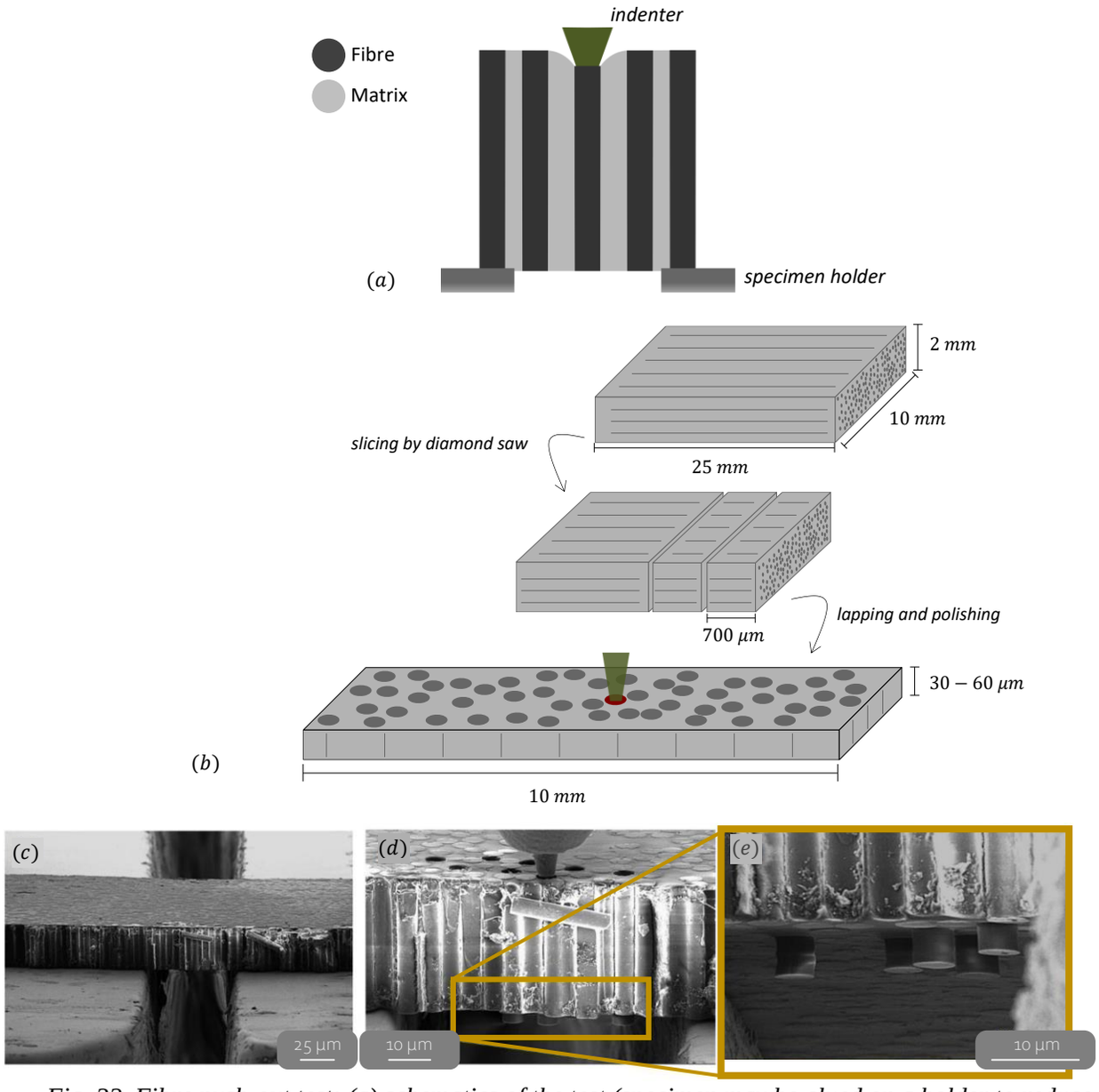

Fig. 32. Fibre push-out test: (a) schematics of the test (specimen may be glued on a holder to reduce the compliance in the load-displacement curve and mitigate the specimen bending during testing), (b) the three-stage mechanical preparation process of the specimens (redrawn from [377]*, with permission from Elsevier), SEM images of the specimen (c) before the test, and (d) and (e) after the test (taken from* [389]*, with permission from Elsevier).*

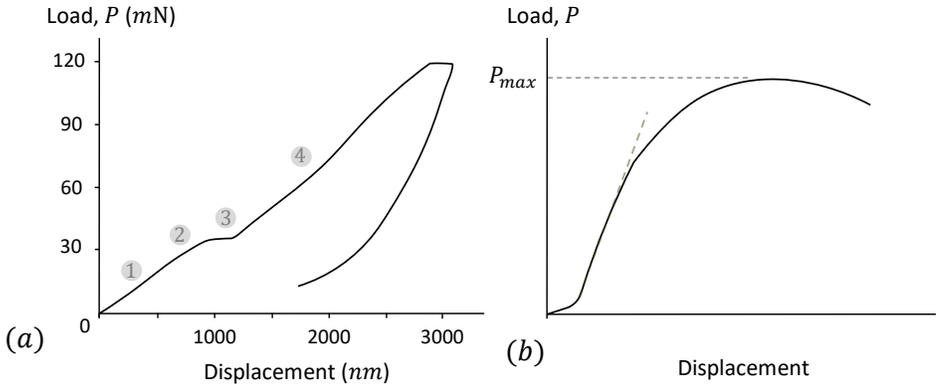

Fig. 33. Load-displacement curve for a push-out test: (a) with distinct four stages: 1 *elastic fibre deformation,* 2 *progressive interfacial debonding,* 3 *plateau appearance after debonding completion (or fibre splitting* [382]*), and* 4 *load increase as the indenter reaches the matrix (recreated by the digitised data from* [390]*), and (b) another reported schematic for a fibre-reinforced composite (redrawn from* [391]*, with permission from Elsevier).*

The individual fibres should be selected randomly (a minimum of 20 fibres with similar cross-sectional areas) for each push-out specimen [377]. However, if the matrix material is poorly translucent, e.g., in the case of CF-PPS, the fibre selection might be practically challenging [392]. Furthermore, to minimise the effect of polishing on the results, a similar polishing quality has to be achieved for all specimens [382]. There are two main specimen preparation routes. The conventional push-out test specimens, using a lapping/polishing method (also known as free-standing samples), exhibit excessive geometric nonlinearities (rather than material nonlinearity), significant compliant response, and large scatter and boundary conditions irregularities. In addition, this sample preparation approach is likely to lead to fracture during the grinding step. Although thickening the sample may reduce the compliance artefacts, it can lead to unintended failure modes such as fibre breakage. Alternatively, femtosecond laser-machined specimens (cave specimens) are free of such flaws and are more suitable for an *in-situ* SEM-based push-out test. Reportedly [393], femtosecond laser machining reduces the heat diffusion into the adjacent material, resulting in high-quality machining with minimal heat-affected zone or microstructural disruption.

Furthermore, the FEM force-displacement curves are more in line with those of the cave specimens. This is due to complications in achieving precise contact boundary conditions in free-standing specimens, while cave specimens exhibit consistent boundary conditions that can be more realistically replicated in an FEM [389]. A sensitivity study [393] for the CF push-out test indicated that a membrane thickness below 20 μm leads to excessive bending, while a 40 μm thick membrane might reveal fibre breakage. Therefore, the membrane thickness is suggested to be in the range of 20-30 μm, enabling a clean pushed-out fibre and the exclusion of the redundant failure modes.

Reportedly [394], the slope of the test is dominated by the position of the fibre inside its bundle or, in a broader sense, by the stiffness of the surrounding material. The deviation from the initial linear behaviour in the load-displacement curves (see Fig. 34), associated with the debonding onset, could emerge at different load levels depending primarily on the loading rate and the temperature. This non-linear region, governed by the viscoelastic phenomena, is classified as the intermediate regime that separates the cohesive-dominated and the frictional regimes [395]. Regarding the effect of loading rate and temperature on the push-out test of CF-epoxy systems, both IFSS and stiffness increase with increased loading rate and decrease with increased temperature. The time-dependent response is more evident for experiments performed at high loading rates or elevated temperatures [396].

6.4. Push-out data reduction schemes

The two main methods to assess the interfacial bond quality are extracting the stress-based IFSS [378] or following an energy-based approach in determining the IFFT [279,375,376,392,397]. The mean stress analysis yields constant interfacial shear stress as:

$$IFSS = \frac{F_d}{2\pi r_f w} \tag{47}$$

where w is the specimen thickness (or the fibre length).

Ideally, for a comprehensive model for interfacial debonding, the debonding energy and the energy associated with friction are separated. The frictional energy part can, in certain cases, persist, whereas the debonding energy disappears when the fibre is fully debonded. For instance, the debonding energy ($GBCD$ area in Fig. 34) and the frictional stress can be estimated using the force-displacement curve as [392]:

$$G_{ic} = \frac{\Delta x(F_{max} - F_{fric.,max})}{4\pi r_f w} \tag{48}$$

$$\tau_f = \frac{F_{fric.,max}}{2\pi r_f w} \tag{49}$$

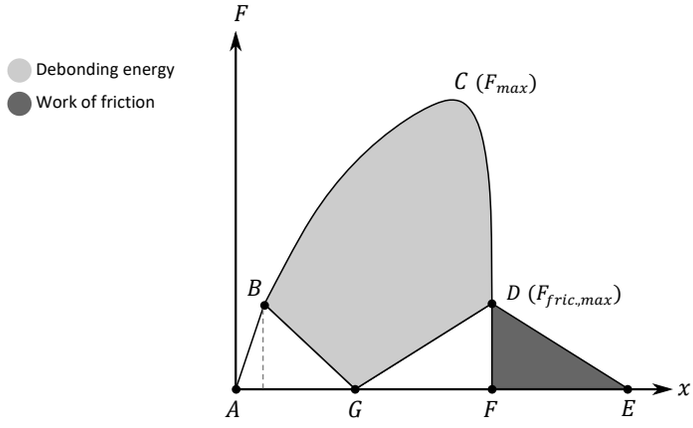

Fig. 34. Representation of the estimated debonding energy (light) and work of friction (dark) on the force-displacement curve of a push-out test. A stable crack growth takes place between phases $B-C$. At C, the stable crack growth transfers into an unstable crack growth. Phase $C-D$ is characterised by complete interfacial debonding, and after that, only fibre push-out happens against frictional stress (redrawn from [392]*, with permission from Elsevier).*

The standard loading scheme (displacement-controlled loading up to push-out) solely enables a qualitative estimation of the fibre push-out event in FRPs. Jäger et al. [391] underlined the importance of considering the matrix plastic deformation as one of the energy contributors in an energy-based analysis, emerging as the slope change in the force-displacement curve after the linear-elastic portion. Therefore, this deviation from the initial linear response, particularly for ductile matrices, should not be misinterpreted as an indication of debond initiation [391]. A cyclic push-out test can effectively determine the IFFT by the acquired dissipated crack energy and the stable crack propagation area. This sequential unloading-reloading till interface fails, as an alternative to the standard loading method, is based on the adaptation of the Mueller et al. approach for CMCs [398] to the FRPs [377,381,391]. These successive unloading-reloading cycles allow a segregated evaluation of the dissipative (fibre, matrix, and interface plastic deformation energy plus work of friction, $\Delta E_{plastic} + \Delta E_{friction}$) and the non-dissipative (elastic deformation energy of the fibre, matrix and bending of the specimen, $\Delta E_{elastic}$) energy contributions. Fig. 35 depicts the integration of the individual contributors [377]. The fracture toughness can be simply calculated as:

$$\text{IFFT} = \frac{total\ separation\ energy}{cylindrical\ fibre\ surface\ area} \tag{50}$$

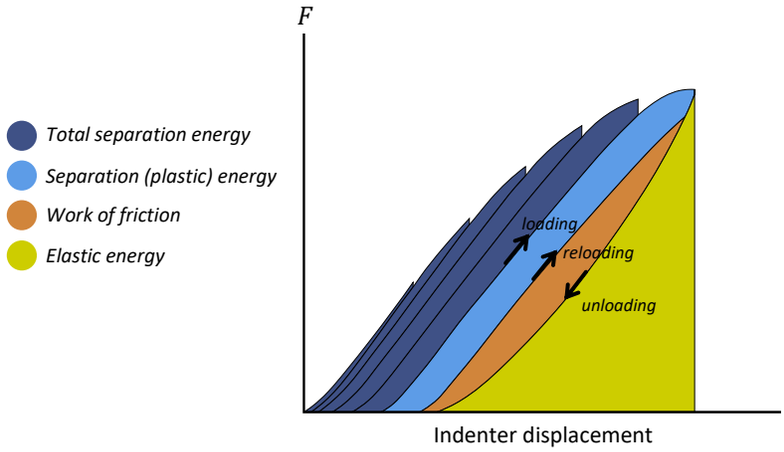

Fig. 35. Various energy contributions to a cyclic push-out test for determination of the IFFT: the elastic energy corresponds to the integral of the unloading curve, the work of friction is determined by the area enclosed between the unloading and reloading curves, the plastic separation energy is represented by the area between the loading curve and the subsequent reloading curve, and the total separation energy refers to the cumulative energy input into stable crack growth (redrawn from [377,394]*, with permission from Elsevier).*

The influence of residual thermal stresses on IFFT was evaluated for CF-PPS systems in [377]. Annealing this composite above the T_g of PPS minimises these thermal residual stresses. This alters the failure behaviour from a brittle interface failure (stable + unstable crack propagation along the sample thickness) to a quasi-ductile (stable crack growth) failure and consequently leads to a 2.4-fold increase in IFFT [377].

During the push-out test, the interfacial debonding occurs through mode II crack propagation [279]. The crack initiation and propagation in a push-out test were modelled using a CZM in an axisymmetric model [399]. A bilinear traction-separation law was used to describe the frictional sliding arising between the crack faces based on the Coulomb friction law. Such an approach implicitly captures the frictional sliding behaviour within the traction-separation law rather than explicitly modelling it through contact algorithms. This prohibits the development of new crack faces and may not be fully representative of the physically observed frictional sliding between the debonded surfaces [399]. Assuming an elastoplastic material for epoxy resin yields a better agreement between experimental and numerical force-indenter displacement curves than the linear-elastic matrix model [391].

6.5. Indenter tip geometry

Fig. 36 illustrates the typical indenter tip geometries for the push-in and push-out tests. Mueller et al. [398] carried out SEM and AFM on the front and backside of the samples in their interrupted ceramic matrix composites push-out tests. The overestimated interfacial properties using a Berkovich (pyramidal) indenter tip were justified by the premature loading of the matrix adjacent to the fibre prior to the push-out development. This can be avoided by using a geometrically viable flat-end indenter tip [398]. Desaeger and Verpoest [382] reported occasional and frequent splitting of GF and CF, respectively, by a pyramidal tip. This was avoided by replacing it with a round semi-spherical tip. Generally, indenter tips with a larger radius of curvature than r_f are advised against. The splitting, due to the stress concentrations underneath the indenter tip and CF anisotropy, is governed by the position of the tip relative to the fibre centre, d_f, V_f, transverse strength of the fibre and the matrix properties [382]. The splitting is accelerated for fibres with low transverse strength and those situated in resin-rich regions. Emerging as a horizontal plateau on the load-displacement curve, splitting might also trigger interfacial debonding [382].

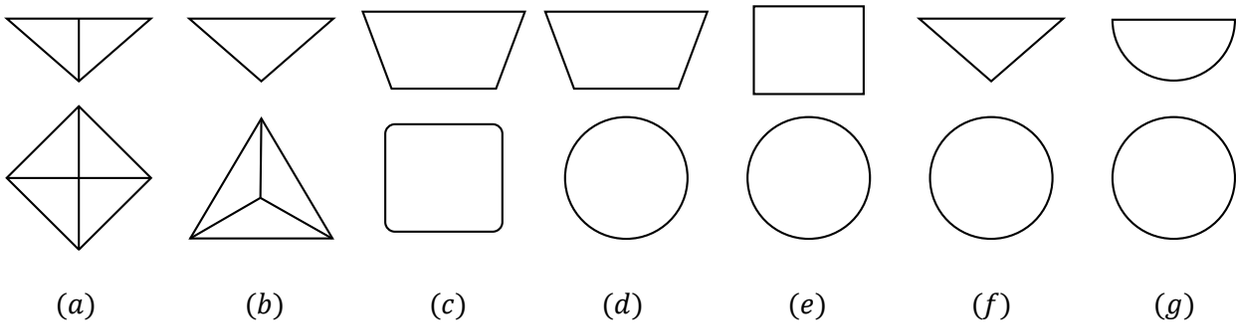

Fig. 36. Schematics of the side and bottom view of typical indenter tips for indentation tests: (a) Vickers, (b) Berkovich, (c) flat-end [398]*, (d) flat-cone* [391]*, (e) cylindrical flat punch* [400]*, (f) conical* [400]*, and (g) spherical (redrawn from* [401]*).*

Sakharova et al. [400], in their 3D numerical simulations, concluded that force-indenter displacement responses are independent of the friction coefficient value (0.04-0.30) between the various indenters and the indented material. The hardness and modulus were varied by a maximum of 1.3% in models with and without friction [401]. To determine the indented specimen's elastic modulus and hardness, one might encounter the geometrical correction factor, $\beta_{geom.}$, which depends on the indenter geometry. Some advantages of the flat-ended punch indenter are that the parameter $\beta_{geom.} = 1$, the applied axial compression is uniform and that the contact area does not change with the indentation depth. The reported correction factors are $\beta_{geom.} = 1.034$, 1.081 and 1.055 for the conical, Berkovich pyramidal and the Vickers pyramidal indenter, respectively [373,400].

Based on the geometrical limitation of the indenter, the expected push-out protrusion length can be identified, e.g., 1-1.2 μm for a Berkovich indenter [396]. Beyond this displacement threshold, the indenter comes in contact with the adjacent material and scrapes the fibres. Therefore, only the $F - \delta$ response below this threshold is representative of the actual single fibre push-out [396].

6.6. Comparison of the two methods

For both push-in and push-out tests, a nanoindenter axially pushes an individual fibre in the cross-section of a specimen until interfacial debonding occurs. Regarding the sample preparation, the push-out test involves laborious effort in fabricating a thin membrane of the composite (thickness of ~50 μm [383,394], 30-60 μm, or commonly ~3-5 times the CF diameter [385]) and polishing of both transverse surfaces (see Fig. 32b), while the push-in test solely requires the polishing of one surface. Depending on the membrane thickness, the test setup can yield different failure modes. In thicker slices (~300 μm), the fibre partially debonds and subsequently fails under compressive stress. However, interpreting the push-in test results is somewhat tricky since the debonded interface length (and consequently the debonding area) is undisclosed. Conversely, for the push-out test, the complete debonding process is perceptible, and the corresponding area can be identified, enabling the quantification of the IFFT [386].

Some studies have compared the results of both methods for identical material systems. Ramanathan et al. [392] investigated the effect of surface modification on the interfacial frictional stress and the debond energy for various CFs via both push-in/-out tests (see Table 4). Their results show that surface-activated CFs with basic oxides, produced by the thermal treatment method, yield higher IFFT values than acidic or unmodified CFs. Medina et al. [385] have reported analogous values of the IFSS in GF-epoxy (+ CNT) composites evaluated by both push-in and push-out tests.

6.7. Conclusions

The application of the nanoindentation method in FRPs has been rapidly growing since the early 2000s [373]. The theoretical models governing both pull- and push-out tests share similarities, except that due to Poisson's effect, lateral contraction of the fibre is observed during pull-out tests while lateral expansion of the fibre is observed during push-out tests. The small size of the nanoindenter tip enables direct measurement of the elastic properties of the constituents. For instance, the matrix behaviour can be directly assessed in the matrix-rich regions of the prepared specimen, where the influence of neighbouring fibres is negligible. In addition to the axial and radial properties of individual constituents, their interfacial properties can be determined. It is a better practice to prepare the specimens from the "real" (i.e. *in-situ*) composite due to the higher resemblance to the polymerisation and manufacturing history of actual FRPs [394]. With this method, the interface degradation can be studied for composites which have already been in service [86].

However, for some fibre-matrix systems, interface fracture is extremely difficult to detect; some fibres split before interface fracture and locating the indenter in the middle of the fibre of interest requires a very accurate positioning system. More optimised and contemporary testing procedures must be established (similar to [382]). Moreover, the success of the tests is closely linked to the polishing quality of the specimens. Continuous stiffness measurement within the instrumentation is crucial for materials with time-dependent properties, such as polymers.

One of the main limitations of the fibre push-out method is the lack of in-situ observations, as the fibre is fully embedded in the matrix. Consequently, there is limited knowledge about how defects in the matrix, such as voids, inclusions, and chemical segregations, or on the fibre, such as surface roughness, non-uniform coatings, and premature oxidation, affect the variability of interfacial property measurements. Even if tested in an SEM, direct visualisation of crack propagation or the dominant failure mechanism is not possible. Additionally, traditional fibre push-out tests often yield a high degree of data variability, which can be better understood and mitigated through the use of innovative in-situ techniques [402]. Moreover, studies on the development of piezoelectric push-out devices have primarily focused on device production, with insufficient attention given to assessing the accuracy and analysing material failure. The accuracy of piezoelectric push-out devices still requires further examination and confirmation [403].

Further studies are required to quantify the IFSS of nanotube-reinforced polymers through push-in/-out techniques [373]. Additionally, surface roughness and adhesive effects between the indenter tip and the specimen surface need to be assessed for their significance. Reportedly [404], the IFSS almost doubled with the surface treatment as measured with SFFT, while the micro-indentation technique reflected only a 17% increase due to the surface treatment. This clearly shows that more work is needed to address this discrepancy. To date, an FE model-assisted push-in/-out technique, considering the intricate interplay of the constituents, has proven to be a more appropriate method for measuring interfacial properties since the test is carried out in-situ on FRP bulks.

Table 5.A presents the reported interfacial properties of CF or GF in thermoset or thermoplastic matrices measured through both push-in/-out methods. Overall, the push-in/-out yields slightly higher IFSS values compared to the previous three micromechanical tests. This can be related to the existing neighbouring fibres, different residual stress states or inherent to the indentation test setup.

7. Infrequent test methods

The methods described earlier are the most widely used ones. However, there are also some lesser-known yet notable alternatives that stand out due to their distinctiveness. Note that *Broutman* and *Outwater-Murphy* tests provide information on transverse debonding, which sets them apart from other interfacial shear tests.

In the **fibre-bundle pull-out test** (which might be considered a macroscopic characterisation method), fibre bundles instead of individual fibres are pulled out from the matrix. Reportedly, the interfacial failure in the fibre-bundle pull-out test is more realistic [405] since fractography reveals that fibre bundles are often pulled out from the matrix rather than single fibres [406]. Interface modification through CNT-coated GF-epoxy, evaluated by this method, led to a significant increase in IFSS due to increased fibre surface roughness and resin wettability [405]. A variant of the fibre-bundle pull-out specimen is *double-end* specimen, with the matrix on either end of the free bundle length [407]. Another pull-out-like test is the **three-fibre method** (1983) [365,408,409], in which a vertical fibre (fibre of interest) is held between two horizontal fibres (support fibres), and the droplet is formed at the three fibres' intersection (see Fig. 37a). The IFSS can be estimated using Gorbatkina [410], Greszczuk [247] or Zhandarov et al. [337] models. This method, being experimentally challenging in the case of thermoplastic matrices, reportedly eliminates the microdrop slippage throughout the slit, featuring a uniform interfacial loading contrary to the microbond test, with the pulled-out fibre surface being matrix-free [215].

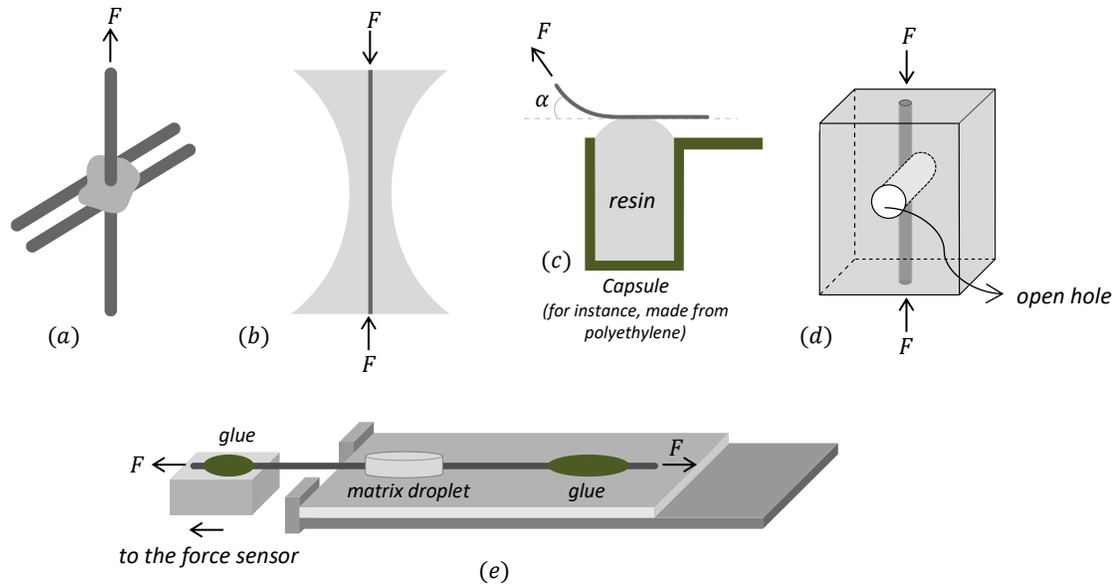

Fig. 37. Schematics of the infrequent test methods: (a) three-fibre test [409]*, (b) Broutman test* [411]*, (c) single-fibre peel test* [412]*, (d) Outwater-Murphy test* [413]*, and (e) fibre-stretching test* [333]*. Note that by not applying a glue droplet on the right side of the fibre in (e), the configuration will portray the microbond test setup used in* [243] *(subfigures are redrawn from* [284] *for (a) and (b), from* [412] *for (c), from* [413] *for (d), and from* [333] *for (e), with permissions from Elsevier).*

The **Broutman test** (1969) [414] consists of a double-notched single-fibre specimen, as shown in Fig. 37b. The application of a compressive load to the neck-shaped specimen results in significant compressive stresses in the smallest cross-section, which in turn cause Poisson's expansion in the transverse direction. As the Poisson's ratio of the matrix, ν_m, is larger than that of the fibre, ν_f, a transverse interfacial debonding stress is induced. Debonding appears in the middle of the specimen where the transverse stress is maximum, and not at the fibre ends. Furthermore, the shear stresses are eliminated in the centre due to specimen symmetry [415]. The interfacial tensile stress, σ_i, that leads to debonding in the centre of the specimen is estimated with:

$$\sigma_i = \frac{\sigma_0(\nu_m - \nu_f)E_f}{(1+\nu_m)E_f + (1-\nu_f-2\nu_f^2)E_m} \quad (51)$$

where σ_0 is the axial stress at the minimum cross-section of the specimen. Acoustic emission and photoelasticity techniques can be used to detect interfacial debonding [416]. Recently, Vogtmann et al. [417] investigated the compression-induced fracture patterns in post-mortem single CF-epoxy Broutman specimens via X-ray CT. Their detailed analysis, coupled with a basic FEM, reveals that the compressive stress is stored in the matrix and suddenly releases to the CF at the moment of a fibre break. This leads to a higher number of fracture pieces between single fragments in a toughened system compared to a non-toughened one.

Another unconventional test is the **single-fibre peel test**. This test was developed in the 1980s as an alternative to the more complex and time-consuming fibre pull-out test. Apart from evaluating the interfacial adhesion between the single fibre and the matrix, it allows evaluating the effect of different interfacial treatments, such as sizing and coatings, and assessing the effectiveness of adhesion promoters or coupling agents. In this test, small capsules are filled with resin and allowed to gel based on the gel time of the resin (Fig. 37c). Afterwards, a fibre is delicately placed over the surface of the resin and put in the oven till the fibre sinks approximately by half its diameter. One of the challenges associated with this test lies in the precise control of the embedding depth of fibres in the resin [412]. For the test to be successful, at least 60% (or half d_f, as suggested in [418]) of the fibre cross-section must stay out. Once the specimen is cured, this is checked with a microscope. The fibre is then peeled, at a controlled rate, using a tensile tester. Peel tests may be conducted at various peel angles; however, it is recommended to carry out the tests with a peel angle of 30° or more [412]. Because of the high stiffness of CFRPs, it is not possible to perform the peel test at peel angles > 60° [419]. The actual peel angle in this test can be evaluated similarly to those outlined in the Appendix of [420]. Provided that the fibre is fully elastic during the peel, the work of fracture, supposedly, is simply the mean peel force divided by $2d_f$ [412]. The key feature of this test and the Broutman test, unlike all the other micromechanical tests, is an induced mode I-dominated failure rather than a mode II-dominated failure. McDaniel et al. [418] quantified the mode I and mode II peel energy release rates for ultra-high molecular weight polyethene fibres in epoxy by variable angle single fibre peel test. Testing at different angles was facilitated through the use of a variable angle fixture.

Outwater and Murphy (1970) [421] measured the interfacial strength by a rectangular-shaped matrix specimen with a single fibre embedded longitudinally through the centre, as shown in Fig. 37d. A hole is then drilled through the specimen thickness, piercing the fibre. The compressive loading of the matrix block produces interfacial shear at the fibre ends near the hole due to discontinuity. The load is increased until debonding is observed optically. Moreover, the specimen lengths should be kept short to avoid buckling [421]. The interface can be characterised in terms of debonding fracture energy by [421]:

$$G_{ic} = \frac{\varepsilon_f^2 E_f d_f}{8} \quad (52)$$

or [413,422]:

$$G_{ic} = \frac{P_c^2 E_f V_f}{2\pi d_f w^2 (E_m V_m)^2} \quad (53)$$

with ε_f as the fibre strain [421], P_c the critical debond load, and w^2 the cross section area of a square specimen.

The **fibre-stretching test** (2000) [333] consists of tensile loading of a fibre in microbond test geometry *at both ends* (see Fig. 37e). This method offers a slow and stable debond propagation for any embedded length and was precise even for long fibre ends since the compliance of the setup does not alter the results) [333]. Reportedly, the cracks always start at the points of the fibre entry in the matrix, almost simultaneously from both ends, and grow symmetrically towards the middle of the sample. The

variational mechanics stress analysis for the microbond test can also be applied to this test, which enables determining G_{ic}, τ_{ult} and τ_f [333].

Lastly, during a **single-fibre push-back test** [423,424], a fully debonded pushed-out fibre is pushed back in the reverse direction beyond its original position. Therefore, information on the interfacial sliding of the frictional surfaces can be obtained. Since the contact area between the fibre and the matrix increases during the fibre push-back, an increase in maximal force is expected. A substantial decrease in sliding friction is observed upon passing through the origin. This reduction can potentially be attributed to the abrasion of the frictional surfaces during the fibre push-back. This so-called "seating drop" (or reseating) phenomenon presumably results from the fibre seating back into its original position, where the surface roughness of the fibre matches the surface of the matrix [424].

This phenomenon enables a distinction between the friction associated with interfacial roughness and that due to the residual stresses. The substantial size of the seating drop indicates that interfacial roughness can account for a large portion of the frictional sliding [425]. This sort of information is particularly beneficial for analysing the debonding conditions and, more precisely, what happens just behind the debond crack tip [426]. No seating drop was observed for CF-PEEK in [427], suggesting a plastic deformation and abrasion of the frictional surfaces during push-back, drastically reducing the topological matching at the initial fibre position. The single-fibre push-back test is predominantly used for CMCs and metal matrix composites.

8. Concluding remarks and outlook

The mechanical properties of FRPs are closely related to the fibre-matrix interfacial properties. Numerous micromechanical test methods have been proposed to characterise the fibre-matrix interface. Still, there is an ongoing debate as to which method is the most precise, reliable and relevant. Uncertainties in the obtained interface characteristics and interlaminar shear strength lead to unreasonably high load safety factors and overweight structures, diminishing the value FRPs provide [428]. It is noteworthy that the interfacial properties of the same material system obtained via different test methods are not comparable. This is primarily due to the fact that the local stress fields brought about by a particular test arrangement are not identical and are not considered accordingly in the respective data reduction schemes. Fig. 38a-b demonstrates the spread and skewness of the reported IFSS values for carbon-epoxy and glass-epoxy systems, respectively. The reported high IFSS values from SFFT, microbond or pull-out test, exceeding the matrix shear strength (outliers in Fig. 38), presumedly were correlated with a complicated interfacial failure pattern rather than pure interfacial shear failure. Fig. 39a indicates that a stronger adhesion at the fibre-matrix interface tends to increase the fracture toughness values in carbon-epoxy systems. However, for glass-epoxy systems, the existing scatter in the reported values (Fig. 39b) prohibits drawing conclusive judgements. Moreover, the inconsistency among various tests also reveals itself in the IFSS ratio of treated to untreated fibre. This indicates that each technique reacts differently to the conditions prevailing at the interface/interphase. Furthermore, controlling the test environment to avoid any influence of external factors such as temperature and humidity and the need for advanced imaging techniques are among the common challenges faced by all the discussed methods.

There is a scarcity of literature that discusses a quantitative process utilising basic SFFT or MFFT data to estimate the fracture toughness of a UD laminate (the transition from micro- to mesoscale). Micromechanical models for interlaminar and translaminar fracture toughness would require the IFFT and friction coefficient, but such models remain rare. Varandas et al. [429] is the only micromechanical model for mode I interlaminar fracture, but unfortunately does not predict the mode I interlaminar fracture toughness and just focuses on crack migration. Pimenta and Pinho [430] developed a micromechanical model to predict the translaminar fracture toughness, and they indeed revealed that IFFT and friction coefficient are vital parameters. To the best of our knowledge, no micromechanical models exist for the mode II or III interlaminar fracture toughness. We, however, believe the

development of such models is now possible and will start appearing in the coming years thanks to the increased computational power available for FE analysis.

An extensive set of investigations have been conducted to determine the relevance of fragmentation testing to real FRPs. These studies have revealed that even a slight change in the interface, which may account for only 1% of the total weight of an FRP, can lead to significant differences in compressive strength and notched fatigue life, with variations of up to 50% and two orders of magnitude, respectively [431]. Furthermore, it is envisaged that the interface greatly influences the long-term performance of such systems, especially life and retained strength under cyclic loading and/or in the presence of aggressive environments such as high temperature and corrosive chemicals [432–434].

Further complications arise when attempts are made to correlate the results of the fragmentation test with the mechanical performance of high V_f FRPs (macrocomposites) since the stress profiles are quite different in each FRP. During micromechanical testing of FRPs, it is assumed that a particular trend in the values of IFSS with different surface treatments reflected by the micromechanical testing will be observed during the macromechanical tests also. However, this correlation is difficult to prove. Different macromechanical properties show differing sensitivities towards the fibre-matrix adhesion measured using the fragmentation test. The ultimate aim of interfacial studies is to provide the knowledge which enables the mechanical and/or hygrothermal properties and hence the reliability of an FRP structure to be ascertained. After seven decades of research in fibre-matrix interface characterisation, it might be opportune to integrate numerous methodologies into a unified, comprehensive model for the fibre-matrix interface and fibre-fibre stress transfer that explains the macroscopic behaviour of FRPs. FE models are deemed to be superior as they are the only models that rely on minimal assumptions.

While the reviewed methods may not give an absolute value, they can elucidate the interfacial failure mechanisms/characteristics and reinforce our comprehension of FRPs' failure. Accordingly, frequent collaborations and multidisciplinary round-robin tests are required to assess the deficiencies in interfacial studies. Absent or inadequate standards are another contributing factor to the observed discrepancies. It is difficult to strengthen the interface reliably without a reliable interfacial characterisation method. Numerically, coupling molecular dynamic simulation, FEM and DEM for multi-scale interfacial investigations would be worthwhile. Some novel tools, such as digital volume correlation on *in-situ* synchrotron radiation computed tomograms, which have proven their practicality in FRP failure analysis, can be exploited for quantifying the full-field volumetric displacements/strain fields in composites.

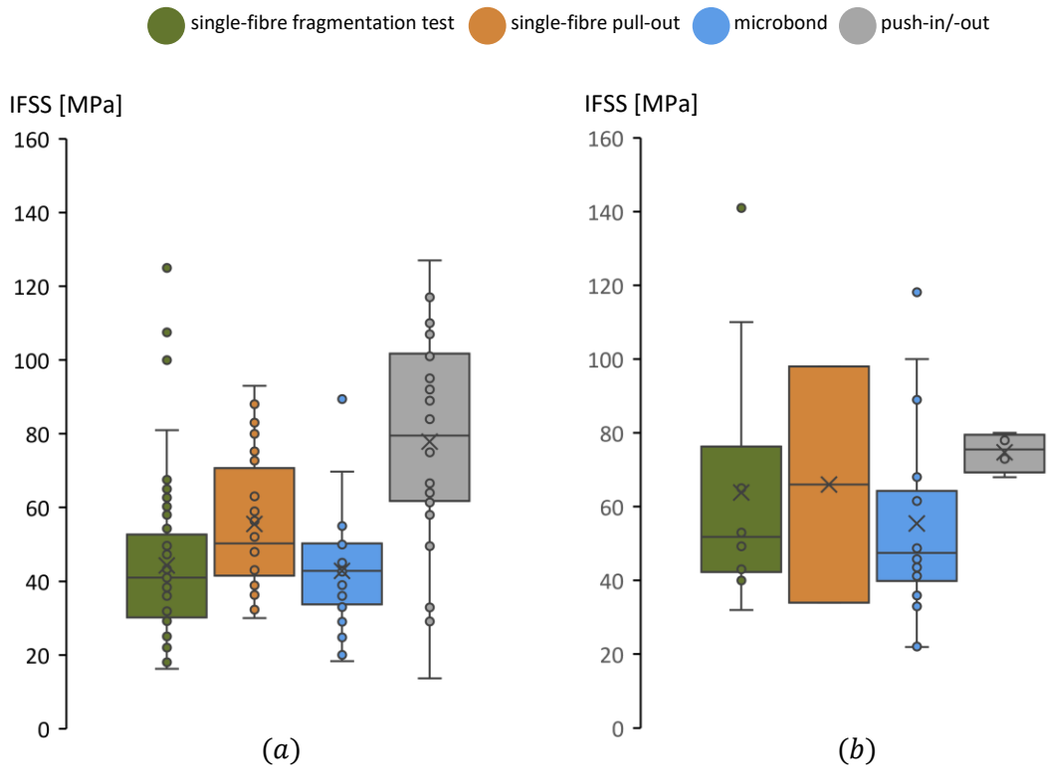

Fig. 38. Reported IFSS from microscale interfacial characterisation tests: (a) for carbon fibre-epoxy systems, and (b) for glass fibre-epoxy systems. The cross within the box indicates the mean, and the vertical line shows the median.

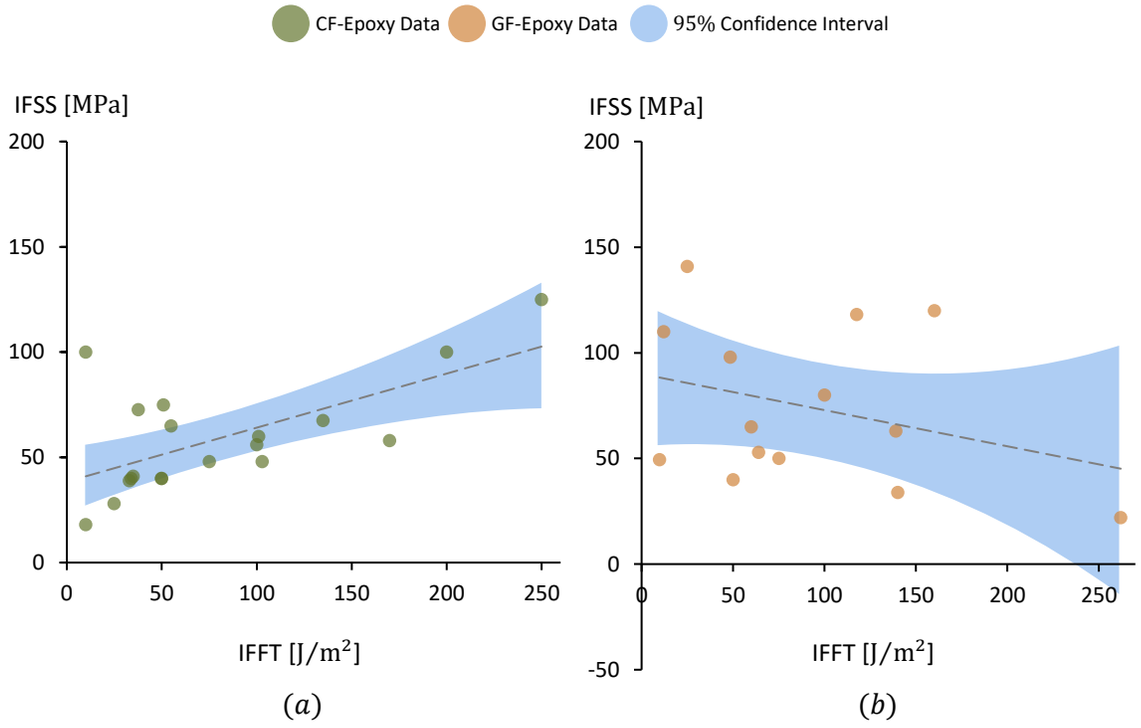

Fig. 39. Interfacial shear strength versus interfacial fracture toughness (only considering references which report both values) for: (a) carbon fibre-epoxy systems [101,133,176,190,216,266,384,387,435]*, and (b) glass fibre-epoxy systems* [102,145,190,216,239,243,304,305,319,320,329,383,436].

There are several gaps in current knowledge about the fibre and matrix interface characterisation in FRPs that could be addressed by future research. Here are some thoughts and suggestions for such research:

(1) Developing new characterisation techniques: Current characterisation techniques have limitations in terms of their sensitivity. Developing new techniques that can provide more detailed information about the interface would be valuable. For example, advanced microscopy techniques such as high-resolution transmission electron microscopy (HRTEM) and scanning transmission electron microscopy (STEM) can provide detailed information about the interface structure, chemistry, and bonding. To obtain scientifically valid and statistically significant results from a large number of specimens, it is essential to have customised equipment for preparing, testing, and analysing the specimens. Automated processes in these areas are expected to expedite fragmentation testing, eliminate manual errors, and help establish a standard protocol for measuring IFSS [203].

(2) Investigating the effect of interface properties on mechanical behaviour: While it is well-established that the fibre-matrix interface plays a critical role in determining the mechanical properties of composite materials, the relationship between interface properties and mechanical behaviour is not well understood. Future research could focus on investigating the effect of interface properties such as interfacial bonding strength, adhesion, and interfacial chemistry on mechanical behaviour.

(3) Developing new materials for the interface: The properties of the fibre-matrix interface are strongly influenced by the chemistry and structure of the interface region. Developing new materials that can enhance the interface properties, such as coupling agents and interphase materials, could improve the overall mechanical performance of FRPs.

(4) The key focus of future developments in CT for interfacial studies in FRPs is expected to comprise: improved imaging technology and resolution, more advanced algorithms for image reconstruction and processing, and increased collaboration between experimental and computational researchers. Another area of interest is the use of in situ CT, which allows for the observation of dynamic processes occurring at the interface under various loading and environmental conditions. This will require the development of specialised experimental setups that can withstand these conditions and maintain the necessary imaging quality [437].

(5) Developing improved micromechanical models to accurately predict interlaminar and translaminar fracture toughness. By combining these models with other micromechanical models for transverse cracking, it is possible to provide mesoscale models with the necessary information to predict the macroscopic behaviour of multidirectional laminates.

Acknowledgements

The effort that has been put into this research is within the framework of the HyFiSyn project, which has received funding from the European Union's Horizon 2020 research and innovation programme under the Marie Skłodowska-Curie grant agreement No. 765881. M. Mehdikhani would like to acknowledge his FWO Postdoc Fellowship, project ToughImage (1263421N).

Disclosure statement

The authors report that there are no competing interests to declare.

References

[1] Kim J-K, Mai Y-W. *Characterization of interfaces*. In the Proceedings of the Engineered Interfaces in

Fiber Reinforced Composites; **1998**.
[2] Nath RB, Fenner DN, Galiotis C. *Finite element modelling of interfacial failure in model carbon fibre-epoxy composites*. Journal of Materials Science **1996**; 31:2879–83.
[3] Hughes JDH. *The carbon fibre/epoxy interface-A review*. Composites Science and Technology **1991**; 41:13–45.
[4] McCarthy ED, Soutis C. *Determination of interfacial shear strength in continuous fibre composites by multi-fibre fragmentation: A review*. Composites Part A: Applied Science and Manufacturing **2019**; 118:281–92.
[5] Mamalis D, Murray JJ, McClements J, Tsikritsis D, Koutsos V, McCarthy ED, Ó Brádaigh CM. *Novel carbon-fibre powder-epoxy composites: Interface phenomena and interlaminar fracture behaviour*. Composites Part B: Engineering **2019**; 174.
[6] İnal O, Katnam KB, Potluri P, Soutis C. *Progress in interlaminar toughening of aerospace polymer composites using particles and non-woven veils*. The Aeronautical Journal **2022**; 126:222–48.
[7] Zeng L, Liu X, Chen X, Soutis C. *π - π Interaction Between Carbon Fibre and Epoxy Resin for Interface Improvement in Composites*. Composites Part B: Engineering **2021**; 220:108983.
[8] Piggott MR. *Why interface testing by single-fibre methods can be misleading*. Composite Science and Technology **1997**; 57:965–74.
[9] Martinez GM, Piggott MR, Bainbridge DMR, Harris B. *The compression strength of composites with kinked, misaligned and poorly adhering fibres*. Journal of Materials Science **1981**; 16:2831–6.
[10] Piggott MR, Xiong Y (June). *Visualization of debonding of fully and partially embedded glass fibres in epoxy resins*. Composites Science and Technology **1994**; 52:535–40.
[11] Sockalingam S, Nilakantan G. *Fiber-Matrix Interface Characterization through the Microbond Test*. International Journal of Aeronautical and Space Sciences **2012**; 13:282–95.
[12] Sethi S, Ray BC. *Environmental effects on fibre reinforced polymeric composites: Evolving reasons and remarks on interfacial strength and stability*. Advances in Colloid and Interface Science **2015**; 217:43–67.
[13] Huang S, Fu Q, Yan L, Kasal B. *Characterization of interfacial properties between fibre and polymer matrix in composite materials – A critical review*. Journal of Materials Research and Technology **2021**; 13:1441–84.
[14] *ASTM D2344/D2344M-13: Standard Test Method for Short-Beam Strength of Polymer Matrix Composite Materials and Their Laminates*. ASTM International **2016**; 15.03.
[15] ISO 14130:1998: fibre-reinforced plastic composites - determinations of apparent laminar shear strength by short-beam method. Geneva, Switzerland; **1998**.
[16] *ASTM D7264/D7264M-07: Standard Test Method for Flexural Properties of Polymer Matrix Composite Materials*. ASTM International **2015**; 15.03.
[17] *ISO 14125:1998 Fibre-reinforced plastic composites -Determination of flexural properties*. **1998**.
[18] Pupurs A, Krasnikovs A, Varna J. *Energy release rate based fiber/matrix debond growth in fatigue. Part II: Debond growth analysis using Paris law*. Mechanics of Advanced Materials and Structures **2013**; 20:288–96.
[19] Kohler S, Cugnoni J, Amacher R, Botsis J. *Transverse cracking in the bulk and at the free edge of thin-ply composites: Experiments and multiscale modelling*. Composites Part A: Applied Science and Manufacturing **2019**; 124:105468.
[20] Herráez M, Mora D, Naya F, Lopes CS, González C, Llorca J. *Transverse cracking of cross-ply laminates: A computational micromechanics perspective*. Composites Science and Technology **2015**; 110:196–204.
[21] Sørensen BF, Lilholt H. *Fiber pull-out test and single fiber fragmentation test - analysis and modelling*. IOP Conference Series: Materials Science and Engineering, 37th Risø International Symposium on Materials Science **2016**; 139.
[22] Pitkethly MJ, Favre JP, Gaur U, Jakubowski J, Mudrich SF, Caldwell DL, Drzal LT, Nardin M, Wagner HD, Di Landro L, Hampe A, Armistead JP, Desaeger M, Verpoest I. *A round-robin programme on interfacial test methods*. Composite Science and Technology **1993**; 48:205–14.
[23] Inkson BJ. Scanning Electron Microscopy (SEM) and Transmission Electron Microscopy (TEM) for Materials Characterization. **2016**.
[24] Ismail Y, Sheng Y, Yang D, Ye J. *Discrete element modelling of unidirectional fibre-reinforced polymers under transverse tension*. Composites Part B: Engineering **2015**; 73:118–25.
[25] París F, Correa E, Canas J. *Micromechanical view of failure of the matrix in fibrous composite materials*. Composites Science and Technology **2003**; 63:1041–52.
[26] Xiong QL, Meguid SA. *Atomistic investigation of the interfacial mechanical characteristics of carbon nanotube reinforced epoxy composite*. European Polymer Journal **2015**; 69:1–15.
[27] Xiao Y, Xian G. *Effects of moisture ingress on the bond between carbon fiber and epoxy resin investigated*

with molecular dynamics simulation. Polymer Composites **2018**; 39:E2074–83.
[28] Tam L ho, He L, Wu C. *Molecular dynamics study on the effect of salt environment on interfacial structure, stress, and adhesion of carbon fiber/epoxy interface*. Composite Interfaces **2019**; 26:431–47.
[29] Zheng H, Zhang W, Li B, Zhu J, Wang C, Song G, Wu G, Yang X, Huang Y, Ma L. *Recent advances of interphases in carbon fiber-reinforced polymer composites: A review*. Composites Part B: Engineering **2022**; 233:109639.
[30] Johnson AC, Hayes SA, Jones FR. *The role of matrix cracks and fibre/matrix debonding on the stress transfer between fibre and matrix in a single fibre fragmentation test*. Composites Part A **2012**; 43:65–72.
[31] Nath RB, Fenner DN, Galiotis C. *Elasto-plastic finite element modelling of interfacial failure in model Kevlar 49 fibre-epoxy composites*. Composites Part A **1996**; 27:821–32.
[32] Nath RB, Fenner DN, Galiotis C. *The progressional approach to interfacial failure in carbon reinforced composites: Elasto-plastic finite element modelling of interface cracks*. Composites Part A **2000**; 31:929–43.
[33] Guild FJ, Vlattas C, Galiotis C. *Modelling of stress transfer in fibre composites*. Composite Science and Technology **1994**; 50:319–32.
[34] Feih S, Wonsyld K, Minzari D, Westermann P, Lilholt H. Testing procedure for the single fiber fragmentation test. **2004**.
[35] Paipetis A, Galiotis C. *Effect of fibre sizing on the stress transfer efficiency in carbon/epoxy model composites*. Composites Part A: Applied Science and Manufacturing **1996**; 27:755–67.
[36] Ten Busschen A, Selvadurai APS. *Mechanics of the segmentation of an embedded fiber, Part I: Experimental investigations*. Journal of Applied Mechanics **1995**; 62:87–97.
[37] Mullin JV, Mazzio VF, Mehan RL. Basic failure mechanisms in advanced composites, NASw-2093, NASA. **1971**.
[38] Thomason JL. *Glass fibre sizing: A review*. Composites Part A **2019**; 127.
[39] Huang Y, Young RJ. *Analysis of the fragmentation test for carbon-fibre/epoxy model composites by means of Raman spectroscopy*. Composites Science and Technology **1994**; 52:505–17.
[40] Tuinstra F, Koenig JL. *Characterization of Graphite Fiber Surfaces with Raman Spectroscopy*. Journal of Composite Materials **1970**; 4:492–9.
[41] Liu F, Wang D, Liu J, Wei H, Zhang H, Xu J, Li S, Qin Z, Wang R, Jia H, Zhang J. *Reviews on Interfacial Properties of the Carbon Fiber Reinforced Polymer Composites*. Journal of Physics: Conference Series 8th Annual International Conference on Material Science and Engineering (ICMSE) **2020**; 1637.
[42] Lacroix T, Keunings R, Desaeger M, Verpoest I. *A new data reduction scheme for the fragmentation testing of polymer composites*. Journal of Materials Science **1995**; 30:683–692.
[43] Desaeger M, Reis MJ, Botelho Do Rego AM, Lopes Da Silva JD, Verpoest I. *Surface characterization of poly(acrylonitrile) based intermediate modulus carbon fibres*. Journal of Materials Science **1996**; 31:6305–15.
[44] Thomason JL, Adzima LJ. *Sizing up the interphase: An insider's guide to the science of sizing*. Composites Part A: Applied Science and Manufacturing **2001**; 32:313–21.
[45] Yuan H, Zhang S, Lu C, He S, An F. *Improved interfacial adhesion in carbon fiber/polyether sulfone composites through an organic solvent-free polyamic acid sizing*. Applied Surface Science **2013**; 279:279–84.
[46] Yue ZR, Jiang W, Wang L, Gardner SD, Pittman Jr CU. *Surface characterization of electrochemically oxidized carbon fibers*. Carbon **1999**; 37:1785–96.
[47] Severini F, Formaro L, Pegoraro M, Posca L. *Chemical modification of carbon fiber surfaces*. Carbon **2002**; 40:735–41.
[48] Chen X, Farber M, Gao Y, Kulaots I, Suuberg EM, Hurt RH. *Mechanisms of surfactant adsorption on non-polar, air-oxidized and ozone-treated carbon surfaces*. Carbon **2003**; 41:1489–500.
[49] Xing L, Liu L, Xie F, Huang Y. *Mutual irradiation grafting on indigenous aramid fiber-3 in diethanolamine and epichlorohydrin and its effect on interfacially reinforced epoxy composite*. Applied Surface Science **2016**; 375:65–73.
[50] Liu L, Huang YD, Zhang ZQ, Nie J. *Ultrasonic modification of aramid fiber-epoxy interface*. Journal of Applied Polymer Science **2001**; 81:2764–8.
[51] Zheng L, Wang Y, Qin J, Wang X, Lu R, Qu C, Wang C. *Scalable manufacturing of carbon nanotubes on continuous carbon fibers surface from chemical vapor deposition*. Vacuum **2018**; 152:84–90.
[52] Boccaccini AR, Cho J, Roether JA, Thomas BJC, Jane Minay E, Shaffer MSP. *Electrophoretic deposition of carbon nanotubes*. Carbon **2006**; 44:3149–60.
[53] Zhao M, Meng L, Ma L, Ma L, Yang X, Huang Y, Ryu JE, Shankar A, Li T, Yan C, Guo Z. *Layer-by-layer grafting CNTs onto carbon fibers surface for enhancing the interfacial properties of epoxy resin*

composites. Composites Science and Technology **2018**; 154:28–36.
[54] Montes-Morán MA, Van Hattum FWJ, Nunes JP, Martínez-Alonso A, Tascón JMD, Bernardo CA. *A study of the effect of plasma treatment on the interfacial properties of carbon fibre-thermoplastic composites*. Carbon **2005**; 43:1795–9.
[55] Drzal LT, Rich MJ, Lloyd PF. *Adhesion of Graphite Fibers to Epoxy Matrices: I. The Role of Fiber Surface Treatment*. The Journal of Adhesion **1982**; 16:1–30.
[56] Schadler LS, Laird C, Figueroa JC. *Interphase behaviour in graphite-thermoplastic monofilament composites - Part I monotonic behaviour*. Journal of Materials Science **1992**; 27:4024–34.
[57] Drzal LT, Rich MJ, Koenig MF, Lloyd PF. *Adhesion of Graphite Fibers to Epoxy Matrices: II. The Effect of Fiber Finish*. The Journal of Adhesion **1983**; 16:133–52.
[58] Lv P, Feng YY, Zhang P, Chen HM, Zhao N, Feng W. *Increasing the interfacial strength in carbon fiber/epoxy composites by controlling the orientation and length of carbon nanotubes grown on the fibers*. Carbon **2011**; 49:4665–73.
[59] Zhang J, Bai JB, Wagner HD, Wiesel E. *Interfacial studies of carbon fiber/epoxy composites using single fiber fragmentation test*. In the Proceedings of the 15th European Conference on Composite Materials; Venice, Italy; **2012**.
[60] Qian H, Bismarck A, Greenhalgh ES, Kalinka G, Shaffer MSP. *Hierarchical composites reinforced with carbon nanotube grafted fibers: The potential assessed at the single fiber level*. Chemistry of Materials **2008**; 20:1862–9.
[61] Liu Q, Lomov S V., Gorbatikh L. *When does nanotube grafting on fibers benefit the strength and toughness of composites?*. Composites Science and Technology **2020**; 188:107989.
[62] Godara A, Gorbatikh L, Kalinka G, Warrier A, Rochez O, Mezzo L, Luizi F, van Vuure AW, Lomov S V., Verpoest I. *Interfacial shear strength of a glass fiber/epoxy bonding in composites modified with carbon nanotubes*. Composites Science and Technology **2010**; 70:1346–52.
[63] Warrier A, Godara A, Rochez O, Mezzo L, Luizi F, Gorbatikh L, Lomov S V., VanVuure AW, Verpoest I. *The effect of adding carbon nanotubes to glass/epoxy composites in the fibre sizing and/or the matrix*. Composites Part A: Applied Science and Manufacturing **2010**; 41:532–8.
[64] Terrones M, Martín O, González M, Pozuelo J, Serrano B, Cabanelas JC, Vega-Díaz SM, Baselga J. *Interphases in graphene polymer-based nanocomposites: Achievements and challenges*. Advanced Materials **2011**; 23:5302–10.
[65] Gnanasekar P, Chen H, Tratnik N, Feng M, Yan N. *Enhancing performance of phosphorus containing vanillin-based epoxy resins by P – N non-covalently functionalized graphene oxide nanofillers*. Composites Part B **2021**; 207.
[66] Lerf A, He H, Forster M, Klinowski J. *Structure of Graphite Oxide Revisited*. The Journal of Physical Chemistry B **1998**; 102:4477–82.
[67] Hussain S, Yorucu C, Ahmed I, Hussain R, Chen B, Khan MB, Siddique NA, Ur I. *Surface modification of aramid fibres by graphene oxide nano-sheets for multiscale polymer composites*. Surface & Coatings Technology **2014**; 258:458–66.
[68] Thomason JL, Nagel U, Yang L, Bryce D. *A study of the thermal degradation of glass fibre sizings at composite processing temperatures*. Composites Part A **2019**; 121:56–63.
[69] Ivens J, Wevers M, Verpoest I. *Influence of carbon fibre surface treatment on composite UD strength*. Composites **1994**; 25:722–8.
[70] Hoecker F, Karger-Kocsis J. *Effects of the interface on the mechanical response of CF/EP microcomposites and macrocomposites*. Composites **1994**; 25:729–38.
[71] Tripathi D, Jones FR. *Review: Single Fibre Fragmentation Test for Assessing Adhesion in Fibre Reinforced Composites*. Journal of Materials Science **1998**; 33:1–16.
[72] ElKhoury L, Berg JC. *The effect of curing schedules on fiber-matrix adhesion in carbon fiber-epoxy resin composites*. Journal of Composite Materials **2022**; 56:699–712.
[73] Campana C, Leger R, Sonnier R, Ferry L, Ienny P. *Effect of post curing temperature on mechanical properties of a flax fiber reinforced epoxy composite*. Composites Part A: Applied Science and Manufacturing **2018**; 107:171–9.
[74] Haider M, Hubert P, Lessard L. *Cure shrinkage characterization and modeling of a polyester resin containing low profile additives*. Composites Part A: Applied Science and Manufacturing **2007**; 38:994–1009.
[75] Li W, Lee LJ. *Shrinkage control of low-profile unsaturated polyester resins cured at low temperature*. Polymer **1998**; 39:5677–87.
[76] Wang H, Yang W, Yu H, Sun W-M. *Assessment of Residual Stresses During Cure and Cooling of Epoxy Resins*. Polymer Engineering and Science **1995**; 35:1895–8.

[77] Wang X, Xu D, Liu HY, Zhou H, Mai YW, Yang J, Li E. *Effects of thermal residual stress on interfacial properties of polyphenylene sulphide/carbon fibre (PPS/CF) composite by microbond test*. Journal of Materials Science **2016**; 51:334–43.
[78] Cottrell AH. *Strong solids*. Proceedings of the Royal Society A **1964**; 282:2–9.
[79] Kelly A, Tyson WR. *Tensile properties of fibre-reinforced metals: Copper/tungsten and copper/molybdenum*. Journal of the Mechanics and Physics of Solids **1965**; 13:329–38.
[80] Gao YC, Mai YW, Cotterell B. *Fracture of fiber-reinforced materials*. Journal of Applied Mathematics and Physics **1988**; 39:550–72.
[81] Hutchinson JW, Jensen HM. *Models of fibre debonding and pullout in brittle composites with friction*. Mechanics of Materials **1990**; 9:139–63.
[82] Graciani E, Mantič V, París F, Varna J. *Numerical analysis of debond propagation in the single fibre fragmentation test*. Composites Science and Technology **2009**; 69:2514–20.
[83] Kim BW, Nairn JA. *Observations of Fiber Fracture and Interfacial Debonding Phenomena Using the Fragmentation Test in Single Fiber Composites*. Journal of Composite Materials **2002**; 36:1825–58.
[84] Kelly A, Tyson WR. *Tensile properties of fibre reinforced metals: copper/tungsten and copper/molybdenum*. Journal of the Mechanics and Physics of Solids **1965**; 13:329–50.
[85] Wood JR, Wagner HD, Marom G. *The compressive fragmentation phenomenon: Using microcomposites to evaluate thermal stresses, single fibre compressive strengths, Weibull parameters and interfacial shear strengths*. Royal Society A: Mathematical, Physical and Engineering Sciences **1996**; 452:235–52.
[86] Verpoest I, Desaeger M, Keunings R. *Critical Review of Direct Micromechanical Test Methods for Interfacial Strength Measurements in Composites*. In the Proceedings of the 3rd International Conference on Composite Interfaces (ICCI-III); Cleveland, Ohio, USA; **1990**.
[87] Netravali AN, Li ZF, Sachse W, Wu HF. *Determination of fibre/matrix interfacial shear strength by an acoustic emission technique*. Journal of Materials Science **1991**; 26:6631–8.
[88] Netravali AN, Topoleski LTT, Sachse WH, Phoenix SL. *An Acoustic Emission Technique for Measuring Fiber Fragment Length Distributions in the Single-Fiber- Composite Test*. **1989**; 35:13–29.
[89] Yilmaz YI. *Analyzing Single Fiber Fragmentation Test Data by Using Stress Transfer Model*. Journal of Composite Materials **2002**; 36:537–51.
[90] Lodeiro MJ. Single-Fibre Fragmentation Test for the Characterisation of Interfacial Phenomena in PMCs. **2001**.
[91] Khan RA, Parsons AJ, Jones IA, Walker GS, Rudd CD, Khan RA, Parsons AJ, Jones IA, Walker GS, Rudd CD. *Interfacial Properties of Phosphate Glass Fiber/Poly(caprolactone) System Measured Using the Single Fiber Fragmentation Test*. Composite Interfaces ISSN: **2011**; 18:77–90.
[92] Ohsawa T, Nakayama A, Miwa M, Hasegawa A. *Temperature dependence of critical fiber length for glass fiber-reinforced thermosetting resins*. Journal of Applied Polymer Science **1978**; 22:3203–12. https://doi.org/10.1002/app.1978.070221115.
[93] Feillard P, Désarmot G, Favre JP. *Theoretical Aspects of the Fragmentation test*. Composite Science and Technology **1994**; 50:265–79.
[94] Figueroa JC, Carney TE, Schadler LS, Laird C. *Mieromeehanics of Single Filament Composites*. Composite Science and Technology **1991**; 42:77–101.
[95] Drzal LT, Rich MJ, Camping JD, Park WJ. *Interfacial Shear Strength and Failure Mechanisms in Graphite Fiber Composites*. In the Proceedings of the 35th Annual Technical Conference Reinforced Plastics/Composites Institute, The Society of the Plastics Industry, Inc.; New Orleans, USA; **1980**.
[96] Tripathi D, Chen F, Jones FR. *The effect of matrix yield strain on the data reduction technique of the single-filament fragmentation test*. Composites Part A **1996**; 27:709–15.
[97] Tripathi D, Turton T, Chen F, Jones FR. *A new method to normalize the effect of matrix properties on the value of interfacial shear strength obtained from the fragmentation test*. Journal of Materials Science **1997**; 32:4759–65.
[98] Lodeiro MJ, Maudgal S, McCartney LN, Morrell R, Roebuck B. Project CPD3 - Report 1 Interface Characterisation and Behaviour: Critical Review of Interface Testing Methods for Composites. **1998**.
[99] Rich MJ, Drzal LT, Hunston D, Holmes GA, McDonough W. *Round Robin Assessment Of The Single Fiber Fragmentation Test*. In the Proceedings of the American Society for Composites 17th Technical Conference; Purdue University, West Lafayette, Indiana; **2002**.
[100] Galiotis C. *A Study of mechanisms of stress transfer in continuous- and discontinuous-fibre model composites by laser raman spectroscopy*. Composite Science and Technology **1993**; 48:15–28.
[101] Nishikawa M, Okabe T, Takeda N, Curtin WA. *Micromechanics of the fragmentation process in single-fiber composites*. Modelling and Simulation in Materials Science and Engineering **2008**; 16:1–19.
[102] van der Meer FP, Raijmaekers S, Rocha IBCM. *Interpreting the single fiber fragmentation test with*

numerical simulations. Composites Part A **2019**; 118:259–66.
[103] Bowyer WH, Bader MG. *On the re-inforcement of thermoplastics by imperfectly aligned discontinuous fibres*. Journal of Materials Science **1972**; 7:1315–21.
[104] Bader MG, Bowyer WH. *An improved method of production for high strength fibre-reinforced thermoplastics*. Composites **1973**; 4:150–6.
[105] Aliotta L, Lazzeri A. *A proposal to modify the Kelly-Tyson equation to calculate the interfacial shear strength (IFSS) of composites with low aspect ratio fibers*. Composites Science and Technology **2020**; 186:107920.
[106] Cox HL. *The elasticity and strength of paper and other fibrous materials*. British Journal of Applied Physics **1952**; 3:72–9.
[107] Lacroix T, Tiimans B, Keunings R, Desaeger M, Verpoest I. *Modelling of critical fibre length and interfacial debonding in the fragmentation testing of polymer composites*. Composite Science and Technology **1992**; 43:379–87.
[108] Mendels DA. Analysis of the single-fibre fragmentation test, NPL Report MATC(A)17. Teddington, Middlesex (UK); **2001**.
[109] Nairn JA. *On the Use of Shear-Lag Methods for Analysis of Stress Transfer in Unidirectional Composites*. Mechanics of Materials **1997**; 26:63–80.
[110] Nayfeh AH. *Thermomechanically induced interfacial stresses in fibrous composites*. Fibre Science and Technology **1977**; 10:195–209.
[111] McCartney L. *Analytical models of stress transfer in unidirectional composites and cross-ply laminates and their applications to the prediction of matrix/transverse cracking, local mechanics concepts for composite material systems*. In the Proceedings of the IUTAM Symposia (International Union of Theoretical and Applied Mechanics); **1992**.
[112] Nairn JA. *Generalized Shear-Lag Analysis Including Imperfect Interfaces*. Advanced Composites Letters **2004**; 13:263–74.
[113] Camanho PP, Hallett SR, editors. Numerical Modelling of Failure in Advanced Composite Materials (A Volume in Woodhead Publishing Series in Composites Science and Engineering). **2015**.
[114] Landis CM, McGlockton MA, McMeeking RM. *An Improved Shear Lag Model for Broken Fibers in Composite Materials*. Journal of Composite Materials **1999**; 33:667–80.
[115] Okabe T, Takeda N. *Elastoplastic shear-lag analysis of single-fiber composites and strength prediction of unidirectional multi-fiber composites*. Composites Part A: Applied Science and Manufacturing **2002**; 33:1327–35.
[116] Landis CM, McMeeking RM. *A Shear-Lag Model for a Broken Fiber Embedded in a Composite with a Ductile Matrix*. Composite Science and Technology **1999**; 59:447–57.
[117] Balacó De Morais A. *Stress distribution along broken fibres in polymer-matrix composites*. Composites Science and Technology **2001**; 61:1571–80.
[118] Okabe T, Takeda N, Kamoshida Y, Shimizu M, Curtin WA. *A 3D shear-lag model considering micro-damage and statistical strength prediction of unidirectional fiber-reinforced composites*. Composites Science and Technology **2001**; 61:1773–87.
[119] Yang Z, Zhang BM, Zhao L, Sun XY. *Stress transfer around a broken fiber in unidirectional fiber-reinforced composites considering matrix damage evolution and interface slipping*. Science China: Physics, Mechanics and Astronomy **2011**; 54:296–302.
[120] Landis CM, Beyerlein IJ, M. McMeeking R. *Micromechanical Simulation of the Failure of Fiber Reinforced Composites*. Journal of the Mechanics and Physics of Solids **2000**; 48:621–48.
[121] Beyerlein IJ, Leigh Phoenix S. *Statistics of fracture for an elastic notched composite lamina containing Weibull fibers -Part I. Features from Monte-Carlo simulation*. Engineering Fracture Mechanics **1997**; 57:241–65.
[122] Drzal LT. *The Effect of Polymeric Matrix Mechanical Properties on the Fiber-Matrix Interfacial Shear Strength*. Materials Science and Engineering **1990**; 126:289–93.
[123] Okabe T, Takeda N. *Estimation of strength distribution for a fiber embedded in a single-fiber composite: experiments and statistical simulation based on the elasto-plastic shear-lag approach*. Composites Science and Technology **2001**; 61:1789–800.
[124] Zhao FM, Okabe T, Takeda N. *Effect of matrix yield properties on fragmentation behavior of single fiber composites*. Composite Interfaces **2002**; 9:289–308.
[125] Whitney JM, Drzal LT. *Axisymmetric stress distribution around an isolated fiber fragment*. Toughened Composites, ASTM STP 937, American Society for Testing and Materials **1987**:179–96.
[126] Nairn JA. *A variational mechanics analysis of the stresses around breaks in embedded fibers*. Mechanics of Materials **1992**; 13:131–54.

[127] Wu W, Desaeger M, Verpoest I, Varna J. *An Improved Analysis of the Stresses in a Single-Fibre Fragmentation Test: I. Two-Phase Model*. Composite Science and Technology **1997**; 57:809–19.
[128] Tripathi D, Chen F, Jones FR. *A Comprehensive Model to Predict the Stress Fields in a Single Fibre Composite*. Journal of Composite Materials **1996**; 30:1514–38.
[129] Wu W, Jacobs E, Verpoest I, Varna J. *Variational approach to the stress-transfer problem through partially debonded interfaces in a three-phase composite*. Composite Science and Technology **1999**; 59:519–35.
[130] Johnson AC, Hayes SA, Jones FR. *An improved model including plasticity for the prediction of the stress in fibres with an interface/interphase region*. Composites Part A **2005**; 36:263–71.
[131] Piggott MR. Load-Bearing Fibre Composites (International Series on the Strength and Fracture of Materials and Structures). 1st ed. London, United Kingdom; **1980**.
[132] Piggott MR. *Failure processes in the fibre-polymer interphase*. Composites Science and Technology **1991**; 42:57–76.
[133] Yallee RB, Young RJ. *Evaluation of interface fracture energy for single-fibre composites*. Composites Science and Technology **1998**; 58:1907–16.
[134] Nardone VC, Prewo KM. *On the strength of discontinuous silicon carbide reinforced aluminum composites*. Scripta Metallurgica **1986**; 20:43–8.
[135] Ji S, Zhao P. *Location of tensile fracture within rigid-brittle inclusions in a ductile flowing matrix*. Tectonophysics **1993**; 220:23–31.
[136] Chen Z, Yan W. *A shear-lag model with a cohesive fibre-matrix interface for analysis of fibre pull-out*. Mechanics of Materials **2015**; 91:119–35.
[137] Xiong X, Shen SZ, Hua L, Li X, Wan X, Miao M. *Predicting tensile behaviors of short flax fiber-reinforced polymer–matrix composites using a modified shear-lag model*. Journal of Composite Materials **2018**; 52:3701–13.
[138] Tucker N, Lindsey K. An Introduction to Automotive Composites. Shawbury, Shrewsbury, Shropshire, UK; **2002**.
[139] Nairn JA, Liu YC. *On the use of energy methods for interpretation of results of single-fiber fragmentation experiments*. Composite Interfaces **1996**; 4:241–61.
[140] Detassis M, Frydman E, Vrieling D, Zhou XF, Wagner HD. *Interface toughness in fibre composites by the fragmentation test*. Composites Part A **1996**; 27:769–73.
[141] Zhou X, Nairn JA, Wagner HD. *Fiber-matrix adhesion from the single-fiber composite test: nucleation of interfacial debonding*. Composites Part A **1999**; 30:1387–400.
[142] Zhuang L, Pupurs A, Varna J, Ayadi Z. *Fiber/matrix debond growth from fiber break in unidirectional composite with local hexagonal fiber clustering*. Composites Part B: Engineering **2016**; 101:124–31.
[143] Pupurs A, Varna J. *Energy release rate based fiber/matrix debond growth in fatigue. Part I: Self-similar crack growth*. Mechanics of Advanced Materials and Structures **2013**; 20:276–87.
[144] Wagner HD, Nairn JA, Detassis M. *Toughness of Interfaces from Initial Fiber-Matrix Debonding in a Single Fiber Composite Fragmentation Test*. Applied Composite Materials **1995**; 2:107–17.
[145] Graciani E, Varna J, Manti V, Blázquez A, París F. *Evaluation of interfacial fracture toughness and friction coefficient in the single fiber fragmentation test*. Procedia Engineering **2011**; 10:2478–83.
[146] Kim BW, Nairn JA. *Experimental verification of the effects of friction and residual stress on the analysis of interfacial debonding and toughness in single fiber composites*. Journal of Materials Science **2002**; 37:3965–72.
[147] Nairn JA. *Fracture mechanics of composites with residual stresses, traction-loaded cracks, and imperfect interfaces*. International Journal of Fracture **2000**; 105:243–71.
[148] Sørensen BF. *Micromechanical model of the single fiber fragmentation test*. Mechanics of Materials **2017**; 104:38–48.
[149] Budiansky B, Hutchinson JW, Evans AG. *Matrix fracture in fiber-reinforced ceramics*. Journal of the Mechanics and Physics of Solids **1986**; 34:167–89.
[150] Sørensen BF, Lilholt H. *Fiber pull-out test and single fiber fragmentation test - analysis and modelling*. IOP Conference Series: Materials Science and Engineering, 37th Risø International Symposium on Materials Science **2016**; 139.
[151] Budiman BA, Takahashi K, Inaba K, Kishimoto K. *A new method of evaluating interfacial properties of a fiber/matrix composite*. Journal of Composite Materials **2015**; 49:465–75.
[152] Turon A, Dávila CG, Camanho PP, Costa J. *An engineering solution for mesh size effects in the simulation of delamination using cohesive zone models*. Engineering Fracture Mechanics **2007**; 74:1665–82.
[153] Alfano G, Crisfield MA. *Finite element interface models for the delamination analysis of laminated composites: mechanical and computational issues*. International Journal for Numerical Methods in

Engineering **2001**; 50:1701–36.
[154] Harper PW, Hallett SR. *Cohesive zone length in numerical simulations of composite delamination*. Engineering Fracture Mechanics **2008**; 75:4774–92.
[155] Ghosh G, Duddu R, Annavarapu C. *A stabilized finite element method for delamination analysis of composites using cohesive elements*. ArXiv:200809015v1 **2020**.
[156] Daudeville L, Allix O, Ladevèze P. *Delamination analysis by damage mechanics: Some applications*. Composites Engineering **1995**; 5:17–24.
[157] Zou Z, Reid SR, Li S, Soden PD. *Modelling Interlaminar and Intralaminar Damage in Filament-Wound Pipes under Quasi-Static Indentation*. **2002**; 36:477–99.
[158] Camanho PP, Davila C, Moura M De. *Numerical Simulation of Mixed-mode Progressive Delamination in Composite Materials*. Journal of Composite Materials **2003**; 37:1415–38.
[159] Yuan H, Li X. *Effects of the cohesive law on ductile crack propagation simulation by using cohesive zone models*. Engineering Fracture Mechanics **2014**; 126:1–11.
[160] Zhao L, Gong Y, Zhang J, Chen Y, Fei B. *Simulation of delamination growth in multidirectional laminates under mode I and mixed mode I / II loadings using cohesive elements*. Composite Structures **2014**; 116:509–22.
[161] Turon A, Camanho PP, Costa J, Renart J. *Accurate simulation of delamination growth under mixed-mode loading using cohesive elements : Definition of interlaminar strengths and elastic stiffness*. Composite Structures **2010**; 92:1857–64.
[162] Turon A, González E V, Sarrado C, Guillamet G, Maimí P. *Accurate simulation of delamination under mixed-mode loading using a cohesive model with a mode-dependent penalty stiffness*. Composite Structures **2018**; 184:506–11.
[163] Budiman BA, Takahashi K, Inaba K, Kishimoto K. *Evaluation of interfacial strength between fiber and matrix based on cohesive zone modeling*. Composites Part A: Applied Science and Manufacturing **2016**; 90:211–7.
[164] Ramirez FA, Carlsson LA, Acha BA. *A method to measure fracture toughness of the fiber/matrix interface using the single-fiber fragmentation test*. Composites Part A: Applied Science and Manufacturing **2009**; 40:679–86.
[165] Dávila CG, Rose CA, Camanho PP. *A procedure for superposing linear cohesive laws to represent multiple damage mechanisms in the fracture of composites*. International Journal of Fracture **2009**; 158:211–23.
[166] Varna J, Joffe R, Berglund LA. *Interfacial toughness evaluation from the single-fiber fragmentation test*. Composites Science and Technology **1996**; 56:1105–9.
[167] Swolfs Y. *Hybridisation of self-reinforced composites: Modelling and verifying a novel hybrid concept (PhD Thesis)* (PhD Thesis). KU Leuven, **2015**.
[168] Xia Z, Curtin WA, Okabe T. *Green's function vs. shear-lag models of damage and failure in fiber composites*. Composites Science and Technology **2002**; 62:1279–88.
[169] Xia Z, Okabe T, Curtin WA. *Shear-lag versus finite element models for stress transfer in fiber-reinforced composites*. Composites Science and Technology **2002**; 62:1141–9.
[170] Babaei R, Farrokhabadi A. *Prediction of debonding growth in two-dimensional RVEs using an extended interface element based on continuum damage mechanics concept*. Composite Structures **2020**; 238:111981.
[171] Cundall PA, Strack ODL. *A discrete numerical model for granular assemblies*. Geotechnique **1979**; 29:47–65.
[172] Le BD, Dau F, Charles JL, Iordanoff I. *Modeling damages and cracks growth in composite with a 3D discrete element method*. Composites Part B: Engineering **2016**; 91:615–30.
[173] Sheng Y, Yang D, Tan Y, Ye J. *Microstructure effects on transverse cracking in composite laminae by DEM*. Composites Science and Technology **2010**; 70:2093–101.
[174] Yang D, Sheng Y, Ye J, Tan Y. *Discrete element modeling of the microbond test of fiber reinforced composite*. Computational Materials Science **2010**; 49:253–9.
[175] Le BD, Dau F, Pham DH, Tran TD. *Discrete element modeling of interface debonding behavior in composite material: Application to a fragmentation test*. Composite Structures **2021**; 272.
[176] Ahmadvashaghbash S, Breite C, Mehdikhani M, Swolfs Y. *Longitudinal debonding in unidirectional fibre-reinforced composites: Numerical analysis of the effect of interfacial properties*. Composites Science and Technology **2021**.
[177] AhmadvashAghbash S, Fazlali B, Mehdikhani M, Swolfs Y. *Finite element analysis of the effect of longitudinal debonding on stress redistributions around fibre breaks in randomly packed fibres*. Composites Science and Technology **2022**; 227:109586.

[178] Galiotis C, Batchelder DN. *Strain dependences of the first- and second-order Raman spectra of carbon fibres*. Journal of Materials Science Letters **1988**; 7:545–7.
[179] Robinson IM, Zakikhani M, Day RJ, Young RJ, Galiotis C. *Strain dependence of the Raman frequencies for different types of carbon fibres*. Journal of Materials Science Letters **1987**; 6:1212–4.
[180] Schadler LS, Galiotis C. *Fundamentals and applications of micro raman spectroscopy to strain measurements in fibre reinforced composites*. International Materials Reviews **1995**; 40:116–34.
[181] Galiotis C, Read RT, Yeung PHJ, Young RJ, Chalmers IF, Bloor D. *High-Modulus Polydiacetylene Single-Crystal Fibers*. Journal of polymer science Part A-2, Polymer physics **1984**; 22:1589–606.
[182] Galiotis C, Young RJ, Batchelder DN. *The solid-state polymerization and physical properties of bis(ethyl urethane) of 2,4-hexadiyne-1,6-diol. II. Resonance Raman spectroscopy*. Journal of Polymer Science: Part A-2, Polymer Physics **1983**; 21:2483–94.
[183] Galiotis C. *Interfacial studies on model composites by laser Raman spectroscopy*. Composites Science and Technology **1991**; 42:125–50.
[184] Jahankhani H, Galiotis C. *Interfacial Shear Stress Distribution in Model Composites, Part 1: A Kevlar 49® Fibre in an Epoxy Matrix*. Journal of Composite Materials **1991**; 25:609–31.
[185] Melanitis N, Galiotis C. *Interfacial micromechanics in model composites using laser Raman spectroscopy*. Proceedings of the Royal Society of London Series A: Mathematical and Physical Sciences **1993**; 440:379–98.
[186] Galiotis C, Paipetis A, Mansion C. *Unification of fibre/matrix interfacial measurements with Raman microscopy*. Journal of Raman Spectroscopy **1999**; 30:899–912.
[187] Montes-Morán MA, Young RJ. *Raman spectroscopy study of high-modulus carbon fibres: Effect of plasma-treatment on the interfacial properties of single-fibre-epoxy composites. Part II - Characterisation of the fibre-matrix interface*. Carbon **2002**; 40:857–75.
[188] Wagner HD. *Interface Mechanics in Fiber Composites: A Short Tutorial (FiBreMoD School Lectures, Day 1, Lecture 1-KU Leuven, Belgium)*. **2019**.
[189] van den Heuvel PWJ, Peijs T, Young RJ. *Failure phenomena in two-dimensional multifibre microcomposites: 2. A Raman spectroscopic study of the influence of inter-fibre spacing on stress concentrations*. Composite Science and Technology **1997**; 57:899–911.
[190] Zhu M, Wang Y, Wang C, Chen F, Liu Q. *An improved analytical model for inversely determining multiple interfacial parameters from single fiber micro-Raman and fragmentation tests*. Composites Science and Technology **2021**:108983.
[191] Kim BW, Nairn JA. *Observations of Fiber Fracture and Interfacial Debonding Phenomena Using the Fragmentation Test in Single Fiber Composites*. Journal of Composite Materials **2002**; 36:1825–58.
[192] Li ZF, Grubb DT, Phoenix SL. *Fiber interactions in the multi-fiber composite fragmentation test*. Composites Science and Technology **1995**; 54:251–66.
[193] Yamamoto G, Onodera M, Koizumi K, Watanabe J, Okuda H, Tanaka F, Okabe T. *Considering the stress concentration of fiber surfaces in the prediction of the tensile strength of unidirectional carbon fiber-reinforced plastic composites*. Composites Part A: Applied Science and Manufacturing **2019**; 121:499–509.
[194] Wagner HD, Amer MS, Schadler LS. *Fibre interactions in two-dimensional composites by micro-Raman spectroscopy*. Journal of Materials Science **1996**; 31:1165–73.
[195] van den Heuvel PWJ, Peijs T, Young RJ. *Failure phenomena in two-dimensional multi-fibre microcomposites: 2. A Raman spectroscopic study of the influence of inter-fibre spacing on stress concentrations*. Composites Science and Technology **1997**; 57:899–911.
[196] Schadler LS, Amer MS, Iskandarani B. *Experimental measurement of fiber/fiber interaction using micro raman spectroscopy*. Mechanics of Materials **1996**; 23:205–16.
[197] Paipetis A, Galiotis C, Liu YC, Nairn JA. *Stress Transfer from the Matrix to the Fibre in a Fragmentation Test: Raman Experiments and Analytical Modeling*. Journal of Composite Materials **1999**; 33:377–99.
[198] Piggott MR. *Expressions governing stress-strain curves in short fibre reinforced polymers*. Journal of Materials Science **1978**; 13:1709–16.
[199] Grubb DT, Li ZF, Phoenix SL. *Measurement of stress concentration in a fiber adjacent to a fiber break in a model composite*. Composites Science and Technology **1995**; 54:237–49.
[200] Nairn JA. *On the use of shear-lag methods for analysis of stress transfer in unidirectional composites*. Mechanics of Materials **1997**; 26:63–80.
[201] Wagner HD, Steenbakkers LW. *Microdamage analysis of fibrous composite monolayers under tensile stress*. Journal of Materials Science **1989**; 24:3956–75.
[202] Jones KD, DiBenedetto AT. *Fiber fracture in hybrid composite systems*. Composites Science and Technology **1994**; 51:53–62.

[203] Mccarthy ED, Kim JH, Heckert NA, Leigh SD, Gilman JW, Holmes GA. *The fiber break evolution process in a 2-D epoxy/glass multi-fiber array*. Composite Science and Technology **2015**; 121:73–81.
[204] Kim JH, Hettenhouser JW, Moon CK, Holmes GA. *A fiber placement device and methodology for preparing 2-D and 3-D combinatorial microcomposites*. Journal of Materials Science **2009**; 44:3626–32.
[205] Netravali AN, Topoleski LTT, Sachse WH, Phoenix SL. *An acoustic emission technique for measuring fiber fragment length distributions in the single-fiber-composite test*. Composites Science and Technology **1989**; 35:13–29.
[206] Goutianos S, Peijs T, Galiotis C. *Mechanisms of stress transfer and interface integrity in carbon/epoxy composites under compression loading part I: Experimental investigation*. International Journal of Solids and Structures **2002**; 39:3217–31.
[207] Goutianos S, Peijs T. *Experimental and numerical investigation into fatigue damage mechanisms in multif ibre microcomposites*. Plastics, Rubber and Composites Processing and Applications **2001**; 30:222–32.
[208] Pupurs A, Varna J. *Fracture mechanics analysis of debond growth in a single-fiber composite under cyclic loading*. Mechanics of Composite Materials **2011**; 47:109–24.
[209] Littell J, Ruggeri C, Goldberg R, Roberts G, Arnold W, Binienda W. *Measurement of Epoxy Resin Tension, Compression, and Shear Stress–Strain Curves over a Wide Range of Strain Rates Using Small Test Specimens*. Journal of Aerospace Engineering **2008**; 21:162–73.
[210] Fiedler B, Hojo M, Ochiai S, Schulte K, Ando M. *Failure behavior of an epoxy matrix under different kinds of static loading*. Composites Science and Technology **2001**; 61:1615–24.
[211] Hsieh TH, Kinloch AJ, Masania K, Taylor AC, Sprenger S. *The mechanisms and mechanics of the toughening of epoxy polymers modified with silica nanoparticles*. Polymer **2010**; 51:6284–94.
[212] Morelle XP, Chevalier J, Bailly C, Pardoen T, Lani F. *Mechanical characterization and modeling of the deformation and failure of the highly crosslinked RTM6 epoxy resin*. Mechanics of Time-Dependent Materials **2017**; 21:419–54.
[213] Breite C. *Aligning Fibre Break Models for Composites with the Observable Micro-Scale Material Behaviour (PhD Thesis)* (PhD Thesis). KU Leuven, **2021**.
[214] Tripathi D, Chen F, Jones FR. *The Effect of Matrix Plasticity on the Stress Fields in a Single Filament Composite and the Value of Interfacial Shear Strength Obtained from the Fragmentation Test*. Royal Society of London Series A: Mathematical, Physical and Engineering Sciences **1996**; 452:621–53.
[215] Pisanova E V., Zhandarov SF. *On the mechanism of failure in microcomposites consisting of single glass fibres in a thermoplastic matrix*. Composites Science and Technology **1997**; 57:937–43.
[216] Piggott MR, Chua PS, Andison D. *The interface between glass and carbon fibres and thermosetting polymers*. Polymer Composites **1985**; 6:242–8.
[217] Chua PS, Piggott MR. *The Glass Fibre-Polymer Interface: II-Work of Fracture and Shear Stresses*. Composite Science and Technology **1985**; 22:107–19.
[218] Melanitis N, Galiotis C, Tetlow PL, Davies CKL. *Interfacial Shear Stress Distribution in Model Composites Part 2: Fragmentation Studies on Carbon Fibre/Epoxy Systems*. Journal of Composite Materials **1992**; 26:574–610.
[219] Shiriajeva GV, Andreevskaya GD. *No Title*. Soviet Plastics **1962**; 4:40.
[220] Favre JP, Perrin J. *Carbon fibre adhesion to organic matrices*. Journal of Materials Science **1972**; 7:1113–8.
[221] Hampe A. *Grundlegende Untersuchungen an faserverstärkten Polymeren*. Amts und Mitteilungsblatt der BAM **1988**; 18:3–7.
[222] Hampe A, Kalinka G, Meretz S, Schulz E. *An advanced equipment for single-fibre pull-out test designed to monitor the fracture process*. Composites **1995**; 26:40–6.
[223] Chua PS, Piggott MR. *The glass fibre-polymer interface: I-theoretical consideration for single fibre pull-out tests*. Composites Science and Technology **1985**; 22:33–42.
[224] Piggott MR. *Debonding and friction at fibre-polymer interfaces. I: Criteria for failure and sliding*. Composites Science and Technology **1987**; 30:295–306.
[225] DiFrancia C, Ward TC, Claus RO. *The single-fibre pull-out test. 1: review and interpretation*. Composites: Part A **1996**; 27:597–612.
[226] Jiang KR, Penn LS. *Improved analysis and experimental evaluation of the single filament pull-out test*. Composites Science and Technology **1992**; 45:89–103.
[227] Kelly A. *Interface effects and the work of fracture of a fibrous composite*. Royal Society of London Series A, Mathematical and Physical Science **1970**; 319:95–116.
[228] Takaku A, Arridge RGC. *The effect of interfacial radial and shear stress on fibre pull-out in composite materials*. Journal of Physics D: Applied Physics **1973**; 6:2038–47.
[229] Piggott MR. *The single-fibre pull-out method: its advantages, interpretation and experimental realization*.

Composite Interfaces **1993**; 1:211–23.
[230] Bannister DJ, Andrews MC, Cervenka AJ, Young RJ. *Analysis of the single-fibre pull-out test by means of Raman spectroscopy: Part II. Micromechanics of deformation for an aramid/epoxy system*. Composites Science and Technology **1995**; 53:411–21.
[231] Wang C. *Fracture mechanics of single-fibre pull-out test*. Journal of Materials Science **1997**; 32:483–90.
[232] Leung CKY, Li VC. *A new strength-based model for the debonding of discontinuous fibres in an elastic matrix*. Journal of Materials Science **1991**; 26:5996–6100.
[233] Noda NA, Chen D, Zhang G, Sano Y. *Single-fiber pull-out analysis comparing the intensities of singular stress fields (ISSFs) at fiber end/entry points*. International Journal of Mechanical Sciences **2020**; 165:105196.
[234] Piggott MR, Xiong Y (June). *Visualization of debonding of fully and partially embedded glass fibres in epoxy resins*. Composites Science and Technology **1994**; 52:535–40.
[235] Zhou L-M, Kim J-K, Mai Y-W. *On the single fibre pull-out problem: effect of loading method*. Composites Science and Technology **1992**; 45:153–60.
[236] Mäder E, Mörschei U, Effing M. *Quality assessment of composites*. JEC Composites Magazine **2016**; 53:49–51.
[237] Chua PS, Piggott MR. *The Glass Fibre-Polymer Interface: III- Pressure and Coefficient of Friction*. Composites Science and Technology **1985**; 22:185–96.
[238] Tsai K-H, Kim K-S. *The micromechanics of fibre pull-out*. Journal of the Mechanics and Physics of Solids **1996**; 44:1147–77.
[239] Zhandarov SF, Edith M, Schef C, Kalinka G, Poitzsch C, Fliescher S. *Investigation of interfacial strength parameters in polymer matrix composites : Compatibility and reproducibility*. Advanced Industrial and Engineering Polymer Research **2018**; 1:82–92.
[240] Deng S, Ye L, Mai YW. *Measurement of interfacial shear strength of carbon fibre/epoxy composites using a single fibre pull-out test*. Advanced Composite Materials **1998**; 7:169–82.
[241] Patrikis AK, Andrews MC, Young RJ. *Analysis of the single-fibre pull-out test by the use of Raman spectroscopy. Part I: Pull-out of Aramid fibres from an epoxy resin*. Composite Science and Technology **1994**; 52:387–96.
[242] Gu XH, Young RJ, Day RJ. *Deformation micromechanics in model carbon fiber reinforced composites, Part I The single-fibre pull-out test*. Journal of Materials Science **1995**; 30:1409–19.
[243] Pisanova E, Zhandarov SF, Mäder E, Ahmad I, Young RJ. *Three techniques of interfacial bond strength estimation from direct observation of crack initiation and propagation in polymer-fibre systems*. Composites Part A: Applied Science and Manufacturing **2001**; 32:435–43.
[244] Zhong W, Pan N. *A Computer Simulation of Single Fiber Pull Out Process in a Composite*. Journal of Composite Materials **2003**; 37:1951–69.
[245] Delfolie C, Depecker C, Lefebvre JM. *Interfacial phenomena in glass fibre reinforced polyester resin with low profile additives. Part I Micromechanical evaluation by pull out testing*. Journal of Materials Science **1999**; 34:481–95.
[246] Greszczuk LB. *Interfaces in Composites*. ASTM STP **1969**; 452:42–58.
[247] Greszczuk LB. *Theoretical Studies of the Mechanics of the Fiber-Matrix Interface in Composites*. Interface in Composites **1969**:42–58.
[248] Pitkethly MJ, Doble JB. *Characterizing the fibre/matrix interface of carbon fibre-reinforced composites using a single fibre pull-out test*. Composites **1990**; 21:389–95.
[249] Lawrence P. *Some theoretical considerations of fibre pull-out from an elastic matrix*. Journal of Materials Science **1972**; 7:1–6.
[250] Zhang XB, Aljewifi H, Li J. *Failure Mechanism Investigation of Continuous Fibre Reinforced Cementitious Composites by Pull-out Behaviour Analysis*. Procedia Materials Science **2014**; 3:1377–82.
[251] Hsueh CH. *Interfacial debonding and fiber pull-out stresses of fiber-reinforced composites, III. With residual radial and axial stresses*. Materials Science and Engineering A **1991**; 149:1–9.
[252] Hsueh CH. *Interfacial debonding and fiber pull-out stresses of fiber-reinforced composites, X: with an elastic interfacial coating*. Materials Science and Engineering A **1991**; 165:189–95.
[253] Zhang X, Liu H, Mai Y, Diao X. *On steady-state fibre pull-out: I The stress field*. Composite Science and Technology **2006**; 59:2179–89.
[254] Fu SY, Yue CY, Hu X, Mai YW. *Analyses of the micromechanics of stress transfer in single-and multi-fiber pull-out tests*. Composites Science and Technology **2000**; 60:569–79.
[255] Marotzke C, Qiao L. *Interfacial crack propagation arising in single-fiber pull-out tests*. Composites Science and Technology **1997**; 57:887–97.
[256] Griffith AA. *The phenomena of rupture and flow in solids*. Philosophical Transactions of the Royal Society

of London Series A, Containing Papers of a Mathematical or Physical Character **1920**; 221:163–8.
[257] Outwarter JD, Murphy MC. *On the fracture energy of unidirectional laminates*. In the Proceedings of the 24th Annual Technical Conference of the Reinforced Plastics Composites Institute, SPI; New York; **1969**.
[258] Teklal F, Djebbar A, Allaoui S, Hivet G, Joliff Y, Kacimi B. *A review of analytical models to describe pull-out behavior – Fiber/matrix adhesion*. Composite Structures **2018**; 201:791–815.
[259] Piggott MR, Sanadi A, Chua PS, Andison D. *Mechanical interactions in the interphasial region of fibre reinforced thermosets*. Composite Interfaces **1986**:109–21.
[260] Penn LS, Chou CT. *Identification of Factors Affecting Single Filament Pull-Out Test Results*. ASTM International, American Society for Testing and Materials **1990**.
[261] Penn LS, Lee SM. *Interpretation of experimental results in the single pull-out filament test*. Journal of Composites, Technology and Research **1989**; 11:23–30.
[262] Zhou L-M, Mai Y-W. *On the single fibre pullout and pushout problem: Effect of fibre anisotropy*. ZAMP Zeitschrift für angewandte Mathematik und Physik **1993**; 44:769–75.
[263] Liu H-Y, Zhou L-M, Mai Y-W. *On fibre pull-out with a rough interface*. Philosophical Magazine A: Physics of Condensed Matter, Structure, Defects and Mechanical Properties **1994**; 70:359–72.
[264] Kim J, Zhou L, Bryan SJ, Mai Y-W. *Effects of fibre volume fraction on the stress transfer in fibre pull-out tests*. Composites **1994**; 25:470–5.
[265] Zhou L-M, Kim J-K, Mai Y-W. *Interfacial debonding and fibre pull-out stresses, Part II A new model based on the fracture mechanics approach*. Journal of Materials Science **1994**; 27:3155–66.
[266] Kim J-K, Baillie C, Mai Y-W. *Interfacial debonding and fibre pull-out stresses, Part I critical comparison of existing theories with experiments*. Journal of Materials Science **1991**; 27:3143–54.
[267] Hsueh CH. *Theoretical comparison of two loading methods in fiber pull-out tests*. Materials Science and Engineering A **1990**; 130:11–5.
[268] Kim JK, Zhou L, Mai YW. *Stress transfer in the fibre fragmentation test - Part I An improved analysis based on a shear strength criterion*. Journal of Materials Science **1993**; 28:6233–45.
[269] Atkinson C, Avila J, Betz E, Smelser RE. *The rod pull out problem, theory and experiment*. Journal of the Mechanics and Physics of Solids **1982**; 30:97–120.
[270] Beckert W, Lauke B. *Critical discussion of the single-fibre pull-out test: Does it measure adhesion?*. Composites Science and Technology **1998**; 57:1689–706.
[271] Sun W, Lin F. *Computer modeling and FEA simulation for composite single fiber pull-out*. Journal of Thermoplastic Composite Materials **2001**; 14:327–43.
[272] Tsai JH, Patra A, Wetherhold R. *Finite element simulation of shaped ductile fiber pullout using a mixed cohesive zone/friction interface model*. Composites Part A: Applied Science and Manufacturing **2005**; 36:827–38.
[273] Jia YY, Yan W, Liu H-Y. *Numerical study on carbon fibre pullout using a cohesive zone model*. In the Proceedings of the International Conferences on Composite Materials; Jeju Island, South Korea; **2011**.
[274] Jia Y, Yan W, Liu H-Y. *Carbon fibre pullout under the influence of residual thermal stresses in polymer matrix composites*. Computational Materials Science **2012**; 62:79–86.
[275] Hoppe L. *Numerical simulation of fiber-matrix debonding in single fiber pull-out tests*. GAMM Archive for Students **2020**; 2:21–35.
[276] Bheemreddy V, Chandrashekhara K, Dharani LR, Hilmas GE. *Modeling of fiber pull-out in continuous fiber reinforced ceramic composites using finite element method and artificial neural networks*. Computational Materials Science **2013**; 79:663–73.
[277] Piggott MR, Chua PS. *Recent Studies of the Glass Fiber-Polymer Interphase*. Industrial and Engineering Chemistry Research **1987**; 26:672–7.
[278] Liu H, Zhang X, Mai Y, Diao X. *On steady-state fibre pull-out: II Computer simulation*. Composite Science and Technology **2006**; 59:2191–9.
[279] Kerans RJ, Parthasarathy TA. *Theoretical Analysis of the Fiber Pullout and Pushout Tests*. Journal of the American Ceramic Society **1991**; 74:1585–96.
[280] Kessler H, Schüller T, Beckert W, Lauke B. *A fracture-mechanics model of the microbond test with interface friction*. Composites Science and Technology **1999**; 59:2231–42.
[281] Nairn JA. *Analytical fracture mechanics analysis of the pull-out test including the effects of friction and thermal stresses*. Advanced Composites Letters **2000**; 9:373–83.
[282] Wu W, Verpoest I, Varna J. *Prediction of energy release rate due to the growth of an interface crack by variational analysis*. Composites Science and Technology **2000**; 60:351–60.
[283] Sørensen BF, Lilholt H. *Fiber pull-out test and single fiber fragmentation test - analysis and modelling*. IOP Conference Series: Materials Science and Engineering, 37th Risø International Symposium on Materials Science **2016**; 139.

[284] Zhandarov SF, Mäder E. *Characterization of fiber/matrix interface strength: Applicability of different tests, approaches and parameters*. Composites Science and Technology **2005**; 65:149–60.
[285] Miller B, Muri P, Rebenfeld L. *A microbond method for determination of the shear strength of a fiber/resin interface*. Composites Science and Technology **1987**; 28:17–32.
[286] Ash JT, Cross WM, Svalstad D, Kellar JJ, Kjerengtroen L. *Finite element evaluation of the microbond test: Meniscus effect, interphase region, and vise angle*. Composites Science and Technology **2003**; 63:641–51.
[287] Burn DT, Harper LT, Johnson M, Warrior NA, Nagel U, Yang L, Thomason J. *The usability of recycled carbon fibres in short fibre thermoplastics: interfacial properties*. Journal of Materials Science **2016**; 51:7699–715.
[288] Miller B, Gaur U, Hirt DE. *Measurement and mechanical aspects of the microbond pull-out technique for obtaining fiber/resin interfacial shear strength*. Composites Science and Technology **1991**; 42:207–19.
[289] van Oss CJ, Chaudhury MK, Good RJ. *Interfacial Lifshitz-van der Waals and Polar Interactions in Macroscopic Systems*. Chemical Reviews **1988**; 88:927–41.
[290] Lu C, Wang J, Lu X, Zheng T, Liu Y, Wang X, Zhang D, Seveno D. *Wettability and Interfacial Properties of Carbon Fiber and Poly(ether ether ketone) Fiber Hybrid Composite*. ACS Applied Materials and Interfaces **2019**; 11:31520–31.
[291] Carroll BJ. *Accurate measurement of contact angle, phase contact areas, drop volume, and Laplace excess pressure in drop-on-fibre systems*. Journal of Colloid and Interface Science **1976**; 57:488–95.
[292] Yamaki JI, Katayama Y. *New method of determining contact angle between monofilament and liquid*. Journal of Applied Polymer Science **1975**; 19:2897–909.
[293] Song B, Bismarck A, Tahhan R, Springer J. *A generalized drop length-height method for determination of contact angle in drop-on-fiber systems*. Journal of Colloid and Interface Science **1998**; 197:68–77.
[294] Wu XF, Dzenis YA. *Droplet on a fiber: Geometrical shape and contact angle*. Acta Mechanica **2006**; 185:215–25.
[295] Wagner HD, Gallis HE, Wiesel E. *Spreading of liquid droplets on cylindrical surfaces: Accurate determination of contact angle*. Journal of Applied Physics **1990**; 67:1352–5.
[296] Nishikawa M, Okabe T, Hemmi K, Takeda N. *Micromechanical modeling of the microbond test to quantify the interfacial properties of fiber-reinforced composites*. International Journal of Solids and Structures **2008**; 45:4098–113.
[297] Yamaguchi A, Hashimoto T, Uematsu H, Urushisaki M, Sakaguchi T, Takamura A, Sasaki D. *Investigation of interfacial adhesion of telechelic polypropylenes for carbon fiber-reinforced plastics*. Polymer Journal **2020**; 52:413–9.
[298] Ash JT, Cross WM, Svalstad D, Kellar JJ, Kjerengtroen L. *Finite element evaluation of the microbond test: meniscus effect, interphase region, and vise angle*. Composite Science and Technology **2003**; 63:641–51.
[299] Mendels DA, Leterrier Y, Månson JAE. *The influence of internal stresses on the microbond test - I: Theoretical analysis*. Journal of Composite Materials **2002**; 36:347–63.
[300] Herrera-Franco PJ, Drzal LT. *Comparison of methods for the measurement of fibre/matrix adhesion in composites*. Composites **1992**; 23:2–27.
[301] Laurikainen P, Kakkonen M, von Essen M, Tanhuanpää O, Kallio P, Sarlin E. *Identification and compensation of error sources in the microbond test utilising a reliable high-throughput device*. Composites Part A: Applied Science and Manufacturing **2020**; 137:105988.
[302] Schüller T, Bahr U, Beckert W, Lauke B. *Fracture mechanics analysis of the microbond test*. Composites Part A: Applied Science and Manufacturing **1998**; 29:1083–9.
[303] Hampe A, Marotzke C. *The energy release rate of the fiber/polymer matrix interface: Measurement and theoretical analysis*. Journal of Reinforced Plastics and Composites **1997**; 16:341–52.
[304] Minnicino MA, Santare MH. *Modeling the progressive damage of the microdroplet test using contact surfaces with cohesive behavior*. Composites Science and Technology **2012**; 72:2024–31.
[305] Sockalingam S, Dey M, Gillespie JW, Keefe M. *Finite element analysis of the microdroplet test method using cohesive zone model of the fiber/matrix interface*. Composites Part A: Applied Science and Manufacturing **2014**; 56:239–47.
[306] Choi NS, Park JE, Kang SK. *Quasi-disk type microbond pull-out test for evaluating fiber/matrix adhesion in composites*. Journal of Composite Materials **2009**; 43:1663–77.
[307] Gaur U, Miller B. *Microbond method for determination of the shear strength of a fiber/resin interface: Evaluation of experimental parameters*. Composites Science and Technology **1989**; 34:35–51.
[308] Zykaite R, Purgleitner B, Stadlbauer W, Burgstaller C. *Microdebond test development and interfacial shear strength evaluation of basalt and glass fibre reinforced polypropylene composites*. Journal of

Composite Materials **2017**; 51:4091–9.
[309] Gonon L, Momtaz A, Van Hoyweghen D, Chabert B, Gérard JF, Gaertner R. *Physico-chemical and micromechanical analysis of the interface in a poly(phenylene sulfide)/glass fiber composite - A microbond study*. Polymer Composites **1996**; 17:265–74.
[310] Gaur U, Besio G, Miller B. *Measuring fiber/matrix adhesion in thermoplastic composites*. Plastics Engineering **1989**:43–5.
[311] Yang L, Thomason JL. *Development and application of micromechanical techniques for characterising interfacial shear strength in fibre-thermoplastic composites*. Polymer Testing **2012**; 31:895–903.
[312] Liu B, Liu Z, Wang X, Zhang G, Long S, Yang J. *Interfacial shear strength of carbon fiber reinforced polyphenylene sulfide measured by the microbond test*. Polymer Testing **2013**; 32:724–30.
[313] Kang SK, Lee DB, Choi NS. *Fiber/epoxy interfacial shear strength measured by the microdroplet test*. Composites Science and Technology **2009**; 69:245–51.
[314] Rao V, Herrera-Franco P, Ozzello AD, Drzal LT. *A Direct Comparison of the Fragmentation Test and the Microbond Pull-out Test for Determining the Interfacial Shear Strength*. The Journal of Adhesion **1991**; 34:65–77.
[315] Hodzic A, Kalyanasundaram S, Lowe A, Stachurski ZH. *The microdroplet test: Experimental and finite element analysis of the dependence of failure mode on droplet shape*. Composite Interfaces **1999**; 6:375–89.
[316] Zhandarov SF, Mäder E. *Peak force as function of the embedded length in pull-out and microbond tests: effect of specimen geometry*. Journal of Adhesion Science and Technology **2005**; 19:817–55.
[317] Schober M. *On the Characterization and Modeling of Interfaces in Fiber Reinforced Polymer Structures* (PhD Thesis). Karlsruhe Institute of Technology, **2019**.
[318] Morlin B, Czigany T. *Cylinder test: Development of a new microbond method*. Polymer Testing **2012**; 31:164–70.
[319] Zhandarov SF, Pisanova E, Mäder E. *Is there any contradiction between the stress and energy failure criteria in micromechanical tests? Part III. Experimental observation of crack propagation in the microbond test*. Journal of Adhesion Science and Technology **2005**; 19:679–704.
[320] Zinck P, Wagner HD, Salmon L, Gerard JF. *Are microcomposites realistic models of the fibre/matrix interface? II. Physico-chemical approach*. Polymer **2001**; 42:6641–50.
[321] Liu Z, Yuan X, Beck AJ, Jones FR. *Analysis of a modified microbond test for the measurement of interfacial shear strength of an aqueous-based adhesive and a polyamide fibre*. Composites Science and Technology **2011**; 71:1529–34.
[322] Choi NS, Park JE. *Fiber/matrix interfacial shear strength measured by a quasi-disk microbond specimen*. Composites Science and Technology **2009**; 69:1615–22.
[323] Hou Y, Sun T. *An improved method to make the microdroplet single fiber composite specimen for determining the interfacial shear strength*. Journal of Materials Science **2012**; 47:4775–8.
[324] Zhandarov SF, Gorbatkina Y, Mäder E. *Adhesional pressure as a criterion for interfacial failure in fibrous microcomposites and its determination using a microbond test*. Composites Science and Technology **2006**; 66:2610–28.
[325] Thomason J. *An overview of some scaling issues in the sample preparation and data interpretation of the microbond test for fibre-matrix interface characterisation*. Polymer Testing **2022**; 111:107591.
[326] Haaksma RA, Cehelnik MJ. *A Critical Evaluation of the Use of the Microbond Method for Determination of Composite Interfacial Properties*. MRS Online Proceedings Library **1989**; 170:71–6.
[327] Brahatheeswaran C, Gupta VB. *Internal stress in a cured epoxy resin system*. Polymer **1993**; 34:289–94.
[328] Lange J, Toll S, Månson JAE, Hult A. *Residual stress build-up in thermoset films cured above their ultimate glass transition temperature*. Polymer **1995**; 36:3135–41.
[329] Mendels DA, Leterrier Y, Manson J-AE, Nairn JA. *The influence of internal stresses on the microbond test II: Physical aging and adhesion*. Journal of Composite Materials **2002**; 36:1655–76.
[330] Thomason JL, Yang L. *Temperature dependence of the interfacial shear strength in glass-fibre polypropylene composites*. Composites Science and Technology **2011**; 71:1600–5.
[331] Zhandarov SF, Pisanova E, Lauke B. *Is there any contradiction between the stress and energy failure criteria in micromechanical tests? Part I. Crack initiation: Stress-controlled or energy-controlled?*. Composite Interfaces **1998**; 5:387–404.
[332] Zhandarov SF, Pisanova E, Mäder E. *Is there any contradiction between the stress and energy failure criteria in micromechanical tests? Part II. Crack propagation: effect of friction on force-displacement curves*. Composite Interfaces **2000**; 7:149–75.
[333] Zhandarov SF, Pisanova E, Schneider K. *Fiber-stretching test: A new technique for characterizing the fiber-matrix interface using direct observation of crack initiation and propagation*. Journal of Adhesion

Science and Technology **2000**; 14:381–98.
[334] Zhandarov SF, Mäder E. *Determining the interfacial toughness from force-displacement curves in the pull-out and microbond tests using the alternative method*. International Journal of Adhesion and Adhesives **2016**; 65:11–8.
[335] Scheer RJ, Nairn JA. *A Comparison of Several Fracture Mechanics Methods for Measuring Interfacial Toughness with Microbond Tests*. The Journal of Adhesion **1995**; 53:45–68.
[336] Liu CH, Nairn JA. *Analytical and experimental methods for a fracture mechanics interpretation of the microbond test including the effects of friction and thermal stresses*. International Journal of Adhesion and Adhesives **1999**; 19:59–70.
[337] Zhandarov SF, Pisanova E V. *The local bond strength and its determination by fragmentation and pull-out tests*. Composites Science and Technology **1997**; 57:957–64.
[338] Gorbatkina YA, Khazanovich TN. *No Title*. In the Proceedings of the The 5th All-Union Congress on Theoretic and Applied Mechanics; Nauka, Alma-Ata, Kazakhstan; **1981**.
[339] Zhandarov SF, Mäder E, Yurkevich OR. *Indirect estimation of fiber/polymer bond strength and interfacial friction from maximum load values recorded in the microbond and pull-out tests. Part I: Local bond strength*. Journal of Adhesion Science and Technology **2002**; 16:1171–200.
[340] Zhandarov SF, Mäder E. *Indirect estimation of fiber/polymer bond strength and interfacial friction from maximum load values recorded in the microbond and pull-out tests. Part II: Critical energy release rate*. Journal of Adhesion Science and Technology **2003**; 17:967–80.
[341] Marotzke C. *Influence of the fiber length on the stress transfer from glass and carbon fibers into a thermoplastic matrix in the pull-out test*. Composite Interfaces **1993**; 1:153–66.
[342] Scheer RJ, Nairn JA. *Variational mechanics analysis of stresses and failure in microdrop debond specimens*. Composites Engineering **1992**; 2:641–54.
[343] Gu X, Young RJ. *Deformation Micromechanics in Model Carbon Fiber Reinforced Composites Part II: The Microbond Test*. Textile Research Journal **1997**; 67:93–100.
[344] Wu HF, Claypool CM. *An analytical approach of the microbond test method used in characterizing the fibre-matrix interface*. Journal of Materials Science Letters **1991**; 10:260–2.
[345] Wu HF, Claypool CM. *A finite-element model of the use of the microbond test method for characterization of composite interfacial properties*. Journal of Materials Science Letters **1991**; 10:1072–5.
[346] Pandey G, Kareliya CH, Singh RP. *A study of the effect of experimental test parameters on data scatter in microbond testing*. Journal of Composite Materials **2011**; 46:275–84.
[347] Zinck P, Wagner HD, Salmon L, Gerard JF. *Are microcomposites realistic models of the fibre/matrix interface? I. Micromechanical modelling*. Polymer **2001**; 42:5401–13.
[348] Penn LS, Lee SM. *Interpretation of Experimental Results in the Single Pull-out Filament Test*. Journal of Composite Technology and Research **1989**; 11:23–30.
[349] Zhandarov SF, Mäder E. *An alternative method of determining the local interfacial shear strength from force-displacement curves in the pull-out and microbond tests*. International Journal of Adhesion and Adhesives **2014**; 55:37–42.
[350] Pisanova E, Zhandarov SF, Mäder E. *How can adhesion be determined from micromechanical tests?*. Composites Part A: Applied Science and Manufacturing **2001**; 32:425–34.
[351] Piggott MR. *A new model for interface failure in fibre-reinforced polymers*. Composites Science and Technology **1995**; 55:269–76.
[352] Banholzer B, Brameshuber W. *Eine methode zur beschreibung des verbundes zwischen faser und zementgebundener matrix*. Beton- und Stahlbetonbau **2001**; 96:663–9.
[353] Brameshuber W, Banholzer B, Brümmer G. *Ansatz für eine vereinfachte Auswertung von Faser-Ausziehversuchen*. Beton- und Stahlbetonbau **2000**; 95:702–6.
[354] Zhandarov SF, Mäder E. *Determination of interfacial parameters in fiber-polymer systems from pull-out test data using a bilinear bond law*. Composite Interfaces **2004**; 11:361–91.
[355] Chou CT, Gaur U, Miller B. *The effect of microvise gap width on microbond pull-out test results*. Composites Science and Technology **1994**; 51:111–6.
[356] Mendels D-A, Leterrier Y, Manson J-AE. *Stress transfer model for single fibre and platelet composites*. Journal of Composite Materials **1999**; 33:1525–43.
[357] Dsouza R, Antunes P, Kakkonen M, Jokinen J, Sarlin E, Kallio P, Kanerva M. *3D interfacial debonding during microbond testing: Advantages of local strain recording*. Composites Science and Technology **2020**; 195:108163.
[358] Dugdale DS. *Yielding of steel sheets containing slits*. Journal of the Mechanics and Physics of Solids **1960**; 8:100–4.
[359] Nishikawa M, Okabe T, Takeda N. *Numerical simulation of interlaminar damage propagation in CFRP*

cross-ply laminates under transverse loading. International Journal of Solids and Structures **2007**; 44:3101–13.

[360] Nian G, Li Q, Xu Q, Qu S. *A cohesive zone model incorporating a Coulomb friction law for fiber-reinforced composites*. Composites Science and Technology **2018**; 157:195–201.

[361] Zhi C, Long H, Miao M. *Microbond testing and finite element simulation of fibre-microballoon-epoxy ternary composites*. Polymer Testing **2018**; 65:450–8.

[362] Gu X, Young RJ. *Deformation Micromechanics in Model Carbon Fiber Reinforced Composites Part I: The single-fibre pull-out test*. Textile Research Journal **1995**; 30:1409–19.

[363] Piggott MR. *Why the fibre/polymer interface can appear to be stronger than the polymer matrix*. Composite Science and Technology **1997**; 57:853–7.

[364] Piggott MR. *A new model for interface failure in fibre-reinforced polymers*. Composite Science and Technology **1995**; 55:269–76.

[365] Järvelä P, Laitinen KW, Purola J, Törmälä P. *The three-fibre method for measuring glass fibre to resin bond strength*. International Journal of Adhesion and Adhesives **1983**; 3:141–7.

[366] Bryce D, Thomason J, Yang L. *Micromechanical and spectroscopic characterisation of the curing performance of epoxy resins in the microbond test*. IOP Conf Series: Materials Science and Engineering (41st Risø International Symposium on Materials Science) **2020**; 942.

[367] Thomason JL, Jenkins PG, Xypolias G. *Microbond testing of the interface in glass fibre vinylester composites*. Composite Interfaces **2022**; 29:695–709.

[368] Yang L, Thomason JL, Zhu W. *Composites : Part A The influence of thermo-oxidative degradation on the measured interface strength of glass fibre-polypropylene*. Composites Part A **2011**; 42:1293–300.

[369] Thomason JL, Yang L. *Temperature dependence of the interfacial shear strength in glass-fibre polypropylene composites*. Composites Science and Technology **2011**; 71:1600–5.

[370] Thomason JL, Yang L. *Temperature dependence of the interfacial shear strength in glass-fibre epoxy composites*. Composite Science and Technology **2014**; 96:7–12.

[371] Minty RF, Yang L, Thomason JL. *The influence of hardener-to-epoxy ratio on the interfacial strength in glass fibre reinforced epoxy composites*. Composites Part A **2018**; 112:64–70.

[372] Mandell JF, Chen JH, McGarry FJ. *A microdebonding test for in situ assessment of fibre/matrix bond strength in composite materials*. International Journal of Adhesion and Adhesives **1980**; 1:40–4.

[373] Gibson RF. *A review of recent research on nanoindentation of polymer composites and their constituents*. Composites Science and Technology **2014**; 105:51–65.

[374] González C, Vilatela JJ, Molina-Aldareguía JM, Lopes CS, LLorca J. *Structural composites for multifunctional applications: Current challenges and future trends*. Progress in Materials Science **2017**; 89:194–251.

[375] Kalinka G, Leistner A, Hampe A. *Characterisation of the fibre/matrix interface in reinforced polymers by the push-in technique*. Composites Science and Technology **1997**; 57:845–51.

[376] Marshall DB, Oliver WC. *Interfacial mechanical properties of fiber-reinforced ceramic composites*. Journal of the American Ceramic Society **1987**; 70:542–8.

[377] Greisel M, Jäger J, Moosburger-Will J, Sause MGR, Mueller WM, Horn S. *Influence of residual thermal stress in carbon fiber-reinforced thermoplastic composites on interfacial fracture toughness evaluated by cyclic single-fiber push-out tests*. Composites Part A: Applied Science and Manufacturing **2014**; 66:117–27.

[378] Marshall DB. *An Indentation Method for Measuring Matrix-Fiber Frictional Stresses in Ceramic Composites*. Journal of the American Ceramic Society **1984**; 67:C-259-C-260.

[379] Marshall DB. *Analysis of fiber debonding and sliding experiments in brittle matrix composites*. Acta Metallurgica et Materialia **1992**; 40:427–41.

[380] Kharrat M, Chateauminois A, Carpentier L, Kapsa P. *On the interfacial behaviour of a glass/epoxy composite during a micro-indentation test: Assessment of interfacial shear strength using reduced indentation curves*. Composites Part A: Applied Science and Manufacturing **1997**; 28:39–46.

[381] Zidi M, Carpentier L, Chateauminois A, Sidoroff F. *Quantitative analysis of the micro-indentation behaviour of fibre-reinforced composites: Development and validation of an analytical model*. Composites Science and Technology **2000**; 60:429–37.

[382] Desaeger M, Verpoest I. *On The Use of the Micro-Indentation Test Technique to Measure the Interfacial Shear Strength of Fibre-Reinforced Polymer Composites*. Composite Science and Technology **1993**; 48:215–26.

[383] Molina-Aldareguía JM, Rodríguez M, González C, Llorca J. *An experimental and numerical study of the influence of local effects on the application of the fibre push-in test*. Philosophical Magazine **2011**; 91:1293–307.

[384] Rodríguez M, Molina-Aldareguía JM, González C, Llorca J. *A methodology to measure the interface shear strength by means of the fiber push-in test*. Composites Science and Technology **2012**; 72:1924–32.
[385] Medina C, Molina-Aldareguía JM, González C, Melendrez MF, Flores P, Llorca J. *Comparison of push-in and push-out tests for measuring interfacial shear strength in nano-reinforced composite materials*. Journal of Composite Materials **2016**; 50:1651–9.
[386] Brunner AJ, Schwiedrzik JJ, Mohanty G, Michler J. *Fiber push-in failure in carbon fiber epoxy composites*. Procedia Structural Integrity **2020**; 28:538–45.
[387] Wang J, Feng Y, Zhao G, Yang L, Xu J. *Effect of elastic and thermal mismatch on push-in mechanism and shear strength measurement of fiber/matrix interface*. Composite Interfaces **2020**; 27:921–35.
[388] Watanabe T, Takeichi Y, Niwa Y, Hojo M, Kimura M. *Nanoscale in situ observations of crack initiation and propagation in carbon fiber/epoxy composites using synchrotron radiation X-ray computed tomography*. Composites Science and Technology **2020**; 197:108244.
[389] Ghaffari S, Seon G, Makeev A. *In-situ SEM based method for assessing fiber-matrix interface shear strength in CFRPs*. Materials and Design **2021**; 197:109242.
[390] Li X, Yang Q, Liu Z. *Interfacial mechanics of fiber push-out test: Nano-indention technique and cohesive element modeling*. In the Proceedings of the 13th International Conference on Fracture, 6; Beijing, China; **2013**.
[391] Jäger J, Sause MGR, Burkert F, Moosburger-Will J, Greisel M, Horn S. *Influence of plastic deformation on single-fiber push-out tests of carbon fiber reinforced epoxy resin*. Composites Part A: Applied Science and Manufacturing **2015**; 71:157–67.
[392] Ramanathan T, Bismarck A, Schulz E, Subramanian K. *Investigation of the influence of surface-activated carbon fibres on debonding energy and frictional stress in polymer-matrix composites by the micro-indentation technique*. Composites Science and Technology **2001**; 61:2511–8.
[393] Ghaffari S, Makeev A, Seon G, Cole DP, Magagnosc DJ, Bhowmick S. *Understanding compressive strength improvement of high modulus carbon-fiber reinforced polymeric composites through fiber-matrix interface characterization*. Materials and Design **2020**; 193:108798.
[394] Rohrmüller B, Gumbsch P, Hohe J. *Calibrating a fiber-matrix interface failure model to single fiber push-out tests and numerical simulations*. Composites Part A: Applied Science and Manufacturing **2021**; 150:106607.
[395] Esqué-De Los Ojos D, Ghisleni R, Battisti A, Mohanty G, Michler J, Sort J, Brunner AJ. *Understanding the mechanical behavior of fiber/matrix interfaces during push-in tests by means of finite element simulations and a cohesive zone model*. Computational Materials Science **2016**; 117:330–7.
[396] Corujeira Gallo S, Li X, Zhang Z, Charitidis C, Dong H. *Viscoelastic response of carbon fibre reinforced polymer during push-out tests*. Composites Part A: Applied Science and Manufacturing **2018**; 112:178–85.
[397] Battisti A, Esqué-de los Ojos D, Ghisleni R, Brunner AJ. *Single fiber push-out characterization of interfacial properties of hierarchical CNT-carbon fiber composites prepared by electrophoretic deposition*. Composites Science and Technology **2014**; 95:121–7.
[398] Mueller WM, Moosburger-Will J, Sause MGR, Horn S. *Microscopic analysis of single-fiber push-out tests on ceramic matrix composites performed with Berkovich and flat-end indenter and evaluation of interfacial fracture toughness*. Journal of the European Ceramic Society **2013**; 33:441–51.
[399] Lin G, Geubelle PH, Sottos NR. *Simulation of fiber debonding with friction in a model composite pushout test*. International Journal of Solids and Structures **2001**; 38:8547–62.
[400] Sakharova NA, Fernandes J V., Antunes JM, Oliveira MC. *Comparison between Berkovich, Vickers and conical indentation tests: A three-dimensional numerical simulation study*. International Journal of Solids and Structures **2009**; 46:1095–104.
[401] Hardiman M. *Nanoindentation Characterisation of Carbon Fibre Reinforced Plastic Microstructures* (PhD Thesis). University of Limerick, **2016**.
[402] De Meyere RMG, Song K, Gale L, Harris S, Edmonds IM, Marrow TJ, Saiz E, Giuliani F, Armstrong DEJ, Gavaldà-Diaz O. *A novel trench fibre push-out method to evaluate interfacial failure in long fibre composites*. Journal of Materials Research **2021**; 36:2305–14.
[403] Sun M, Feng Y, Xu J, Wang X, Zhou H. *Design, Analysis and Experiment of the Fiber Push-Out Device Based on Piezoelectric Actuator*. Micromachines **2021**; 12.
[404] Herrera PJ, Drzal LT. *Comparison of methods for the measurement of fibre/matrix adhesion in composites*. Composites **1992**; 23:2–27.
[405] Zhao G, Liu H-Y, Du X, Zhou H, Mai Y-W, Jia Y-Y, Yan W. *Glass fibres coated with flame synthesised carbon nanotubes to enhance interface properties*. Composites Communications **2021**; 24:100623.
[406] Hu J, Dong S, Feng Q, Zhou M, Wang X, Cheng Y. *Tailoring carbon nanotube/matrix interface to optimize*

mechanical properties of multiscale composites. Carbon **2014**; 69:621–5.
[407] Zhamu A, Zhong WH, Stone JJ. *Experimental study on adhesion property of UHMWPE fiber/nano-epoxy by fiber bundle pull-out tests*. Composites Science and Technology **2006**; 66:2736–42.
[408] Gorbatkina YA. Adhesive strength in fibre-polymer systems. New York; **1992**.
[409] Andreevska GD, Gorbatkina YA. *Adhesion of Polymeric Binders to Glass Fiber*. Industrial and Engineering Chemistry Product Research and Development **1972**; 11:24–6.
[410] Gorbatkina YA, Ivanova-Mumzhieva VG, Gorenberg AY. *Adhesive strength of bonds of polymers with carbon fibres at different loading rates*. Fibre Chemistry **1999**; 31:405–9.
[411] Zhou J, Li Y, Li N, Hao X, Liu C. *Interfacial shear strength of microwave processed carbon fiber/epoxy composites characterized by an improved fiber-bundle pull-out test*. Composites Science and Technology **2016**; 133:173–83.
[412] Alimuddin MA, Piggott MR. *Fracture toughness of fiber-polymer interfaces estimated from single fiber peel tests*. Polymer Composites **1999**; 20:655–63.
[413] Farooq MU, Carlsson LA, Acha BA. *Determination of fiber/matrix adhesion using the Outwater-Murphy single fiber specimen*. Engineering Fracture Mechanics **2009**; 76:2758–65.
[414] Broutman LJ. *Measurement of the Fiber-Polymer Matrix Interfacial Strength*. Interfaces in Composites ASTM International **1969**:27–41.
[415] Sinclair R, Young RJ, Martin RDS. *Determination of the axial and radial fibre stress distributions for the Broutman test*. Composites Science and Technology **2004**; 64:181–9.
[416] Ageorges C, Friedrich K, Schüller T, Lauke B. *Single-fibre Broutman test: Fibre-matrix interface transverse debonding*. Composites Part A: Applied Science and Manufacturing **1999**; 30:1423–34.
[417] Vogtmann J, Klingler A, Rief T, Gurka M. *3D X-Ray Microscopy as a Tool for in Depth Analysis of the Interfacial Interaction Between a Single Carbon Fiber and an Epoxy Matrix after Mechanical Loading*. Journal of Composites Science **2021**; 5.
[418] McDaniel PB, Deitzel JM, Gregory D, Polakovic T, Gillespie JW. *Single fiber peel test to assess ultra high molecular weight polyethylene fiber mesostructure interactions*. Journal of Applied Polymer Science **2018**; 135:1–11.
[419] Alimuddin MA. *Peel test for the evaluation of environmental effects on fiber-polymer interface (Master Thesis)* (PhD Thesis). University of Toronto, **1999**.
[420] Crocombe AD, Adams RD. *Peel Analysis Using the Finite Element Method*. The Journal of Adhesion **1981**; 12:127–39.
[421] Outwater JO, Murphy MC. *The Influences of Environment and Glass Finishes on the Fracture Energy of Glass-Epoxy Joints*. The Journal of Adhesion **1970**; 2:242–53.
[422] Farooq MU, Carlsson LA, Acha BA. *Design Analysis of the Outwater-Murphy Single-Fiber Specimen*. Journal of Composite Materials **2009**; 43:2455–67.
[423] Jero PD. *Interfacial properties of SiC/borosilicate glass systems by indentation pushout*. American Ceramic Society **1990**; 69:484.
[424] Jero PD, Kerans RJ. *The contribution of interfacial roughness to sliding friction of ceramic fibers in a glass matrix*. Scripta Metallurgica et Materialia **1990**; 24:2315–8.
[425] Jero PD, Kerans RJ, Parthasarathy TA. *Effect of Interfacial Roughness on the Frictional Stress Measured Using Pushout Tests*. Journal of the American Ceramic Society **1991**; 74:2793–801.
[426] Cherouali H, Fantozzi G, Reynaud P, Rouby D. *Analysis of interfacial sliding in brittle-matrix composites during push-out and push-back tests*. Materials Science and Engineering A **1998**; 250:169–77.
[427] Moosburger-Will J, Greisel M, Schulz M, Löffler M, Mueller WM, Horn S. *Investigation of the fiber-matrix interaction in carbon fiber-reinforced polyether ether ketone by cyclic single fiber push-out and push-back tests*. Composite Interfaces **2020**; 27:227–47.
[428] Soutis C. *Fibre reinforced composites in aircraft construction*. Progress in Aerospace Sciences **2005**; 41:143–51.
[429] Varandas LF, Arteiro A, Catalanotti G, Falzon BG. *Micromechanical analysis of interlaminar crack propagation between angled plies in mode I tests*. Composite Structures **2019**; 220:827–41.
[430] Pimenta S, Pinho ST. *An analytical model for the translaminar fracture toughness of fibre composites with stochastic quasi-fractal fracture surfaces*. Journal of the Mechanics and Physics of Solids **2014**; 66:78–102.
[431] Reifsnider KL. *Modelling of the interphase in polymer-matrix composite material systems*. Composites **1994**; 25:461–9.
[432] Buxton A, Baillie C. *A study of the influence of the environment on the measurement of interfacial properties of carbon fibre/epoxy resin composites*. Composites **1994**; 25:604–8.
[433] Gaur U, Chou CT, Miller B. *Effect of hydrothermal ageing on bond strength*. Composites **1994**; 25:609–

12.
[434] Schutte CL, McDonough W, Shioya M, McAuliffe M, Greenwood M. *The use of a single-fibre fragmentation test to study environmental durability of interfaces/interphases between DGEBA/mPDA epoxy and glass fibre: the effect of moisture*. Composites **1994**; 25:617–24.
[435] DiBenedetto A. *Measurement of the Thermomechanieal Stability of Interphases by the Embedded Single Fiber Test*. Composite Science and Technology **1991**; 42:103–23.
[436] Graciani E, Balzquez A, Paris F, Varna J. *Numerical analysis of the single fibre fragmentation test using cohesive elements*. In the Proceedings of the 14th European Conference on Composite Materials; Budapest, Hungary; **2010**.
[437] Garcea SC, Wang Y, Withers PJ. *X-ray Computed Tomography of Polymer Composites*. Composites Science and Technology **2018**; 156:305–19.
[438] Melanitis N, Galiotis C, Tetlow PL, Davies CKL. *Interfacial shear stress distribution in model composites: the effect of fibre modulus*. Composites **1993**; 24:459–66.
[439] Ma T, Liu L, Wang C. *Interfacial shear strength of opaque resin/carbon fiber based on mapping from energy dispersive X-ray spectroscopy*. Polymer Composites **2020**; 41:2134–44.
[440] Qi G, Du S, Zhang B, Tang Z, Yu Y. *Evaluation of carbon fiber/epoxy interfacial strength in transverse fiber bundle composite: Experiment and multiscale failure modeling*. Composites Science and Technology **2014**; 105:1–8.
[441] Qi G, Du S, Zhang B, Yu Y. *A new approach to assessing carbon fiber/epoxy interfacial shear strength by tensile test of 45° fiber bundle composites: Experiment, modeling and applicability*. Composites Science and Technology **2016**; 129:214–21.
[442] Dilandro L, Dibenedetto AT, Groeger J. *The effect of fiber-matrix stress transfer on the strength of fiber-reinforced composite materials*. Polymer Composites **1988**; 9:209–21.
[443] Boura O, Diamanti EK, Grammatikos SA, Gournis D, Paipetis AS. *Carbon nanotube growth on high modulus carbon fibres: Morphological and interfacial characterization*. Surface and Interface Analysis **2013**; 45:1372–81.
[444] Lachman N, Carey BJ, Hashim DP, Ajayan PM, Wagner HD. *Application of continuously-monitored single fiber fragmentation tests to carbon nanotube/carbon microfiber hybrid composites*. Composites Science and Technology **2012**; 72:1711–7.
[445] Kim KJ, Kim J, Yu WR, Youk JH, Lee J. *Improved tensile strength of carbon fibers undergoing catalytic growth of carbon nanotubes on their surface*. Carbon **2013**; 54:258–67.
[446] Kim T, Kameya M, Natori J, Kawada H. *Fabrication of CNTs grafted hierarchical multiscale composite and evaluation of its mechanical properties*. In the Proceedings of the 16th European Conference on Composite Materials; Seville, Spain; **2014**.
[447] Anthony DB, Sui XM, Kellersztein I, De Luca HG, White ER, Wagner HD, Greenhalgh ES, Bismarck A, Shaffer MSP. *Continuous carbon nanotube synthesis on charged carbon fibers*. Composites Part A: Applied Science and Manufacturing **2018**; 112:525–38.
[448] Qian H, Bismarck A, Greenhalgh ES, Shaffer MSP. *Carbon nanotube grafted carbon fibres: A study of wetting and fibre fragmentation*. Composites Part A: Applied Science and Manufacturing **2010**; 41:1107–14.
[449] Zhou XF, Wagner HD, Nutt SR. *Interfacial properties of polymer composites measured by push-out and fragmentation tests*. Composites: Part A **2001**; 32:1543–51.
[450] Ramirez FA, Carlsson LA. *Modified single fiber fragmentation test procedure to study water degradation of the fiber/matrix interface toughness of glass/vinylester*. Journal of Materials Science **2009**; 44:3035–42.
[451] Mahato B, Babarinde VO, Abaimov SG, Lomov S V., Akhatov I. *Interface strength of glass fibers in polypropylene: Dependence on the cooling rate and the degree of crystallinity*. Polymer Composites **2020**; 41:1310–22.
[452] Etcheverry M, Ferreira ML, Capiati NJ, Pegoretti A, Barbosa SE. *Strengthening of polypropylene-glass fiber interface by direct metallocenic polymerization of propylene onto the fibers*. Composites Part A **2008**; 39:1915–23.
[453] Bogoeva-Gaceva G, Mäder E, Häußler L, Sahre K. *Parameters affecting the interface properties in carbon fibre/epoxy systems*. Composites **1995**; 26:103–7.
[454] Miramini A, Kadkhodaei M, Alipour A, Mashayekhi M. *Analysis of interfacial debonding in shape memory alloy wire-reinforced composites*. Smart Materials and Structures **2016**; 25:15032.
[455] Du X, Xu F, Liu H-Y, Miao Y, Guo W-G, Mai Y-W. *Improving the electrical conductivity and interface properties of carbon fiber/epoxy composites by low temperature flame growth of carbon nanotubes*. RSC Advances **2016**; 6:48896–904.
[456] Zhandarov SF, Mäder E. *An alternative method of determining the local interfacial shear strength from*

force-displacement curves in the pull-out and microbond tests. International Journal of Adhesion and Adhesives **2014**; 55:37–42.

[457] Pearson A, Liao W, Kazemi Y, Duncan M, Slingerland E, Kakroodi A, Heydrich M, Hammami A, Naguib HE. *Fiber-matrix adhesion between high-density polyethylene and carbon fiber*. Polymer Testing **2022**; 105:107423.

[458] Yang L, Thomason JL. *Development and application of micromechanical techniques for characterising interfacial shear strength in fibre-thermoplastic composites*. Polymer Testing **2012**; 31:895–903.

[459] Zu M, Li Q, Zhu Y, Dey M, Wang G, Lu W, Deitzel JM, Gillespie JW, Byun JH, Chou TW. *The effective interfacial shear strength of carbon nanotube fibers in an epoxy matrix characterized by a microdroplet test*. Carbon **2012**; 50:1271–9.

[460] An F, Lu C, Guo J, He S, Lu H, Yang Y. *Preparation of vertically aligned carbon nanotube arrays grown onto carbon fiber fabric and evaluating its wettability on effect of composite*. Applied Surface Science **2011**; 258:1069–76.

[461] An F, Lu C, Li Y, Guo J, Lu X, Lu H, He S, Yang Y. *Preparation and characterization of carbon nanotube-hybridized carbon fiber to reinforce epoxy composite*. Materials and Design **2012**; 33:197–202.

[462] Ren C, Gong Q, Guo L, Zhao X, Liang J. *Analyses of reinforcing effects of in situ grown CNTs on carbon fibre fabric/epoxy composites at micro- and macroscale*. Micro and Nano Letters **2012**; 7:240–3.

[463] Wang C, Li Y, Tong L, Song Q, Li K, Li J, Peng Q, He X, Wang R, Jiao W, Du S. *The role of grafting force and surface wettability in interfacial enhancement of carbon nanotube/carbon fiber hierarchical composites*. Carbon **2014**; 69:239–46.

[464] Gao X, Jensen RE, Li W, Deitzel J, McKnightt SH, Gillespie JW. *Effect of fiber surface texture created from silane blends on the strength and energy absorption of the glass fiber/epoxy interphase*. Journal of Composite Materials **2008**; 42:513–34.

[465] Haldar S, Herráez M, Naya F, González C, Lopes CS. *Relations between intralaminar micromechanisms and translaminar fracture behavior of unidirectional FRP supported by experimental micromechanics*. Composites Part B: Engineering **2019**; 174.

[466] Naya F, Molina-Aldareguía JM, Lopes CS, González C, Llorca J. *Interface Characterization in Fiber-Reinforced Polymer–Matrix Composites*. Jom **2017**; 69:13–21.

[467] Xu T, Luo H, Xu Z, Hu Z, Minary-Jolandan M, Roy S, Lu H. *Evaluation of the Effect of Thermal Oxidation and Moisture on the Interfacial Shear Strength of Unidirectional IM7/BMI Composite by Fiber Push-in Nanoindentation*. Experimental Mechanics **2018**; 58:111–23.

[468] Zhang L, De Greef N, Kalinka G, Van Bilzen B, Locquet JP, Verpoest I, Seo JW. *Carbon nanotube-grafted carbon fiber polymer composites: Damage characterization on the micro-scale*. Composites Part B: Engineering **2017**; 126:202–10.

[469] Adams RD, Lloyd DH. *Apparatus for measuring the torsional modulus and damping of single carbon fibres*. Journal of Physics E Scientific Instruments **1975**; 8:475–80.

[470] Adams RD. *The dynamic longitudinal shear modulus and damping of carbon fibres*. Journal of Physics D: Applied Physics **1975**; 8:738–48.

List of Abbreviations and Symbols

45FBT	45° fibre bundle tensile test
AE	Acoustic emission
AFM	Atomic force microscopy
ANN	Artificial neural network
BAM	Federal institute for materials research and testing
BEM	Boundary element method
CF	Carbon fibre
CFRP	Carbon fibre reinforced polymer
CKT	Cottrell-Kelly-Tyson model
CMC	Ceramic matrix composites
CNT	Carbon nanotubes
CT	Computed tomography
CTE	Coefficient of thermal expansion
CZM	Cohesive zone model
DEM	Discrete element method
EPZ	Embedded process zone model
FBG	Fibre Bragg grating
FE(M)	Finite element (method)
FRP	Fibre-reinforced polymer
GF	Glass fibre
GFRP	Glass fibre reinforced polymer
HM	High modulus carbon fibre
IFFT	Interfacial fracture toughness
IFNS	Interfacial normal (radial) strength
IFSS	Interfacial shear strength
$IFSS_{app}$	Apparent interfacial shear strength
ILSS	Interlaminar shear strength
IMD	Intermediate modulus
LRS	Laser Raman spectroscopy
MB (MBT)	Microbond test
MFFT	Multi-fibre fragmentation test
MRS	Micro-Raman spectroscopy
PA	Polyamide
PC	Polycarbonate
PEEK	Polyether ether ketone
PEI	Polyetherimide
PP	Polypropylene
PPS	Polyphenylene sulphide
SCF	Stress (or strain) concentration factor
SEM	Scanning electron microscopy
SERR	Strain energy release rate
SFFT	Single-fibre fragmentation test
SLM	Shear-lag model
TFBT	Transverse fibre bundle tensile test
TP	Thermoplastic

A_{emb}	Embedded area
a	Crack length
b_i	Interface effective thickness
$\mathrm{d}a$	Change in crack length
$\mathrm{d}C$	Change in compliance
d_f	Fibre diameter
$\mathrm{d}U$	Energy summation proposed by Marshall and Oliver
$\mathrm{d}U_e$	Change of the elastic energy inside the fibre
$\mathrm{d}U_f$	Work of friction in the interface
$\mathrm{d}U_{G_i}$	Debonding energy associated with the new debonded area
$\mathrm{d}U_l$	Potential energy of the loading system
$\mathrm{d}U_m$	Change in matrix elastic energy
E_1	Longitudinal Young's modulus of the model composite
E_f (E_{f1})	Axial Young's modulus of the fibre
E_m	Matrix Young's modulus
E_T	Transverse Young's modulus of the fibre
$F-\delta$	Force-displacement
F_b	Initial post-debonding force
F_{cat}	Catastrophic failure load
F_d	Debonding force
$F_{fric.,max}$	Maximum frictional force
F_{max}	Maximum load
F_s	Shear force
G	Strain energy release rate (fracture toughness)
G_i	Interfacial fracture toughness
$G_{int.}$	Shear modulus of the interface
G_m	Matrix shear modulus
$G_{prop.}$	Strain energy release rate for debond propagation
G_{ic}^{II}	Interfacial mode II fracture toughness
H	Height in contact angle
K	slope of the force-displacement curve
K_f	fibre free length stiffness
K_i	Cohesive stiffness
L	Droplet length
l	Fibre length, Axial location of the crack front
l_{avg}	Arithmetic mean of the fragment lengths at saturation
l_c	Critical fibre length
l_{cat}	Fibre embedded length shorter than $l_{max,cat}$
l_d	Debond length
l_{emb}	Embedded fibre length
$l_{emb,c}$	Critical embedded length
l_{free}	Fibre free-length
l_m	The point where the results of FEM, variational mechanics and SLM converge
l_{max}	Maximum fragment length
$l_{max,cat}$	Maximum fibre length beyond which catastrophic debonding does not occur
$l_{max,friction}$	Maximum fibre length to surpass the frictional dissipation of energy
m	A parameter acquired from the slope of the u against ${F_s}^2$ plot in push-in tests
P	Applied load
P_c	Critical load at the debond initiation
P_d	Debonding load
q_o	Normal pressure exerted on the fibre due to the matrix shrinkage during cure
R	Axial distance at which $\tau_m = 0$
R_{eq}	Equivalent cylinder radius
R_i	Indentation position to the fibre centre
S_0	Slope of the linear region in a push-in load-displacement curve

T_f	Tensile force on fibre
T_g	Glass transition temperature
T_m	Tensile force on matrix
U_θ	Deformation in θ direction in a cylindrical coordinate system ($r\theta z$)
u	Total recorded displacement throughout the push-in test
u_{ep}	Elastoplastic indentation of the fibre surface
u_f	Fibre surface displacement due to the fibre compression
$V_{droplet}$	Droplet volume
V_f	Fibre volume fraction
V_m	Matrix volume fraction
U_θ	Deformation in θ direction in a cylindrical coordinate system ($r\theta z$)
W_A	Work required to separate the two neighbouring molecular layers of the fibre and the matrix, Work of adhesion
w	Thickness of a push-out specimen (equal to the fibre length)
w^2	Cross section area of a square specimen
z	Fibre axial axis
z^*	The z-coordinate where the stress is evaluated

α_{fL}	Axial thermal expansion coefficients of the fibre
α_{fT}	Transverse thermal expansion coefficients of the fibre
α_m	Thermal expansion coefficient of the matrix
β	Shear-lag parameter
β_{Cox}	Cox shear-lag parameter
$\beta_{geom.}$	Geometrical correction factor
β_{Nayfeh}	Nayfeh shear-lag parameter
$\Delta E_{elastic}$	Elastic deformation energy of the fibre, matrix and bending of the sample
$\Delta E_{friction}$	Work of friction
$\Delta E_{plastic}$	Plastic deformation energy of fibre, matrix, and interface
ΔT	Temperature difference
δ	Separation in traction-separation
ε	Applied strain, Fibre axial strain distributions
ε_f	Fibre strain
ε_m	Matrix strain
θ	Contact angle
k	Frictional stress transfer rate
λ	Effective normal displacement between the contacting surfaces required for their separation
μ_i	Interfacial friction coefficient
ν_f	Fibre Poisson's ratio
ν_{fL}	Axial Poisson's ratios of the fibre
ν_{fT}	Transverse Poisson's ratios of the fibre
ν_m	Poisson's ratio of the Matrix
σ_0	Net axial stress, Axial stress at the minimum cross-section of the specimen
σ_{c1}	Longitudinal stress in a model composite
σ_d	Debonding initiation stress, Adhesion pressure
σ_f	Fibre failure strength
σ_i	Interfacial tensile stress
σ_n	Normal stress
σ_{rr}	Radial stress in variational mechanics
$\sigma_{rr}^{critical}$	Critical radial stress
σ_{ult}	Critical radial stress value at the onset of the debond initiation
$\bar{\sigma}_z$	Cross-sectional average axial stress of fibre
τ_y	Matrix shear yield strength
τ_{app}	Apparent interfacial shear strength
τ_d	Local interfacial shear strength
τ_f	Interfacial frictional sliding stress (post-debond frictional shear stress)

τ_i	Interfacial shear stress
τ_{ic}	Interfacial shear strength
τ_m	Shear stress of the matrix
τ_{max}	Maximum interfacial shear stress
τ_{max}^{act}	Actual interfacial shear strength
τ_{max}^{LRS}	Maximum interfacial shear stress obtained from laser Raman spectroscopy
τ_{max}^{SLM}	Interfacial shear strength obtained with the shear-lag model
$\tau_{max,th}^{s}$	Maximum residual shear stress
τ_{rz}	Interfacial shear stress in variational mechanics
$\tau_{thermal}$	Residual thermal stresses
τ_{ult}	Ultimate interfacial shear strength

Appendix

To avoid cramming the sections with analytical equations, the excess (but practical) harmonised equations are dispatched here, wherever possible.

Table 1.A. Overview of the major stress-based analytical models. Equations in black font are the main equations, whereas the ones in grey font are parameter definitions required for the main equations.

Model	Equation	Additional info
Cottrell-Kelly-Tyson [78,84]	$l_s = \frac{d_f}{4}\frac{E_f\varepsilon_\infty}{\tau_{ic}}$ $\sigma_{fz} = \begin{cases} 4\tau_{ic}\frac{z}{d_f}, & 0 \le z \le l_s \\ E_f\varepsilon_\infty, & l_s \le z \le \infty \end{cases}$ $\tau_i = \begin{cases} -\tau_{ic}, & 0 \le z \le l_s \\ 0, & l_s \le z \le \infty \end{cases}$	l_s is the slip length, ε_∞ is the far-field strain in the fibre direction and z is the axial coordinate along the fibre with the origin located at the break.
Cox [106]	$\sigma_{fz} = E_f\varepsilon_\infty\left[1 - \frac{\cosh\beta\,(l/2 - z)}{\cosh\beta\,(l/2)}\right]$ $\tau_i = \frac{E_f r_f \varepsilon_\infty \beta}{2}\left[\frac{\sinh\beta\,(l/2 - z)}{\cosh\beta\,(l/2)}\right]$ $\beta_{Cox} = \sqrt{\frac{2\pi G_m}{E_f A_f \ln(R_m/r_f)}}$	To employ the Nayfeh model [110], simply replace β_{Cox} with: $\beta_{Nayfeh} = \sqrt{\frac{2}{r_f^2 E_f E_m}\left[\frac{E_f V_f + E_m V_m}{\frac{V_m}{4G_f} + \frac{1}{2G_m}\left[\frac{1}{V_m}\ln\frac{1}{V_f} - 1 - \frac{V_m}{2}\right]}\right]}$ β_{Nayfeh} is adequate for a wide practical range of V_f (0.001 to ~ 0.3), which covers micromechanical tests with single fibres [109].
Modified Cox by Landis-McMeeking [116]	$l_s = \frac{d_f}{4}\left(\frac{E_f\varepsilon_\infty}{\tau_c} - 2\sqrt{\frac{E_f w}{G_m d_f}}\right)$ $\sigma_{fz} = \begin{cases} 4\tau_{ic}\frac{z}{d_f}, & 0 \le z \le l_s \\ E_f\varepsilon_\infty - 2\tau_{ic}\sqrt{\frac{E_f w}{G_m d_f}}\exp\left[2\frac{\sqrt{G_m d_f}}{E_f w}\left(\frac{l_s - z}{d_f}\right)\right], & l_s \le z \le \infty \end{cases}$ $\tau_i = \begin{cases} -\tau_{ic}, & 0 \le z \le l_s \\ -\tau_{ic}\exp\left[2\frac{\sqrt{G_m d_f}}{E_f w}\left(\frac{l_s - z}{d_f}\right)\right], & l_s \le z \le \infty \end{cases}$	Shear sliding can be added to the Cox model by limiting the shear stress at the interface to a prescribed value of τ_c. w is a measure of fibre spacing. Note that if: $\varepsilon_\infty \le 2\frac{\tau_c}{E_f}\sqrt{\frac{E_f w}{G_m d_f}}$ then $l_s = 0$ and σ_{fz} and τ_i are given by original Cox equations.
Whitney-Drzal [125]	$\sigma_{fz} = A_1\varepsilon_\infty\left[1 - (4.75\frac{z}{L_i} + 1)e^{\left(-4.75\frac{z}{L_i}\right)}\right]$ $\tau_i = -4.75\mu A_1\varepsilon_\infty\frac{z}{L_i}e^{-4.75\frac{z}{L_i}}$ $A_1 = E_{1f} + \frac{4K_f G_m \nu_{1f}}{(K_f + G_m)}(\nu_{1f} - \nu_m)$ $K_f = \frac{E_m}{2(2 - E_{2f}/2G_{2f} - 2\nu_{2f}E_{2f}/E_{1f})}$ $L_i = \frac{2.375(d_f/2)}{\mu}$ $\mu = \sqrt{\frac{G_m}{E_{1f} - 4\nu_{1f}G_m}}$	L_i is the ineffective length: the distance over which the broken fibre stress recovers to 95% of the far-field stress. K_f is the plane strain bulk modulus of the fibre.
Mendels [108]	$\sigma_{fz} = \varphi_1\cosh(\beta z) + \varphi_2\sinh(\beta z)$ $\varphi_1 = \frac{\left(\frac{2\tau_f l_d^r/r_f + \psi_\infty}{\cosh\beta(l_t - l_d^r)}\right) - \left(\frac{2\tau_f l_d^l/r_f + \psi_\infty}{\cosh\beta(l_t - l_d^l)}\right)}{\tanh\beta(l_t - l_d^r) - \tanh\beta(l_t - l_d^l)}$ $\varphi_2 = \frac{\left(\frac{2\tau_f l_d^r/r_f + \psi_\infty}{\sinh\beta(l_t - l_d^r)}\right) - \left(\frac{2\tau_f l_d^l/r_f + \psi_\infty}{\sinh\beta(l_t - l_d^l)}\right)}{\frac{1}{\tanh\beta(l_t - l_d^r)} - \frac{1}{\tanh\beta(l_t - l_d^l)}}$ $\psi_\infty = E_f(\varepsilon_\infty + \varepsilon_i) + K$ $\beta = \sqrt{\kappa\frac{(r_f^2 E_f + (r_m^2 - r_f^2)E_m)}{r_f E_f(1 + \nu_m)}}$	This partial-debonding stress transfer model involves two debonded zones, l_d^r and l_d^l, respectively the right and the left debond lengths, both of which are shorter than the half-length of the fibre, l_t. The model assumes uniform friction in these regions with a value of $\pm\tau_f$. The ψ_∞ is the far-field shrinkage due to the contribution of ε_∞ and ε_i (the tension applied to the fibre pre-curing) and K (thermal shrinkage). κ is a function of the constituents elastic moduli and the system geometry.

Table 2.A. Reported Interfacial properties in the literature for SFFT of CF and GF reinforced composites.

Material	IFSS [MPa]	IFFT [J/m^2]	Friction Coeff.	Ref.
CF-Epoxy	23.8±6.6 *(untreated)*, 47.3±15.4 *(treated)*	-	-	[22]
AS4 CF-Epoxy	68.3	-	-	[404]
PAN-based T50 CF-Epoxy	40±1	34±1	-	[133]
AS4 CF-Epoxy	-	220 *(new debonds)*, 105 *(whole)*	-	[83]
AS4 CF-Epoxy	-	220	-	[146]
AS4 CF-Epoxy	48	103	-	[435]
IM6G CF-Epoxy	58	170	-	[435]
HMS4 CF-Epoxy	40	50	-	[435]
HMS CF-Epoxy	36±6	-	-	[438]
IMD CF-Epoxy	66±15	-	-	[438]
CF-Epoxy	30.1±0.9 *(from l_c in LRS)*, 41.9±7.2 *(from peak shear stress in LRS)*	-	-	[197]
Unsized CF-Epoxy	25.9±0.9 *(from l_c in LRS)*, 36.8±6.5 *(from peak shear stress in LRS)*	-	-	[197]
T300 CF-Epoxy	56.1 *(optical microscopy)*, 54.3 *(mapping from EDS)*	-	-	[439]
T700 CF-Epoxy	39.9 *(optical microscopy)*, 41.9 *(mapping from EDS)*	-	-	[439]
T1000 CF-Epoxy	42.1 *(optical microscopy)*, 45.2 *(mapping from EDS)*	-	-	[439]
T300 CF-Epoxy *(FEM)*	60-75 *(weak interface)* 100 *(intermediate interface)* 125 *(strong interface)* 18.7 *(IFSS from SFFT)*	120-150 *(weak interface)* 200 *(intermediate interface)* 250 *(strong interface)*	-	[101]
T700S CF-Epoxy	107.5 *(IFSS from combined 45FBT and FEM)* 72.7 *(IFNS from combined TFBT and FEM)*	-	-	[440,441]
PAN-based T50-Epoxy	26.2-26.7	-	-	[39]
Pitch-based P55-Epoxy	16.1-16.4	-	-	[39]
AS4-Epoxy	60.26 *(mean fragment length by AE)* 59.33 *(mean fragment length optically)*	-	-	[87]
PAN-based T50-Epoxy	20±2 *(untreated)* 45±4 *(plasma-treated fibre)*	-	-	[187]
HM CF-Epoxy	30.1±7.2 *(treated, CKT)* 41.9±3.5 *(treated, LRS)* 25.9±6.5 *(untreated, CKT)* 36.8±5.7 *(untreated, LRS)*	-	-	[35]
HM CF-Epoxy *(FEM fitted on* [35]*)*	-	-	0.8-0.9	[32]
T700GC CF-Epoxy	56.3 *(as received)* 39.9 *(unsized)* 49.6 *(resized)* 35.5 *(CNT-grafted)*	-	-	[59]
T300-Epoxy	17.4 *(unsized)* 22.3-47.8 *(depends on orientation and length of grafted MWCNTs)*	-	-	[58]
AS4-Epoxy	47.9	-	-	
HMS4-Epoxy	40.3	-	-	[442]
IM6G-Epoxy	58.4	-	-	
CF-Epoxy *(FEM parametric study)*	30-100	10-100	-	[190]
M40-Epoxy	28.1±5.5 *(unsized)*, 32.0±6.1 *(CNT-grafted)*	-	-	[443]
T300-Epoxy	36.9±8.3, 70.0±12.5 *(CNT-grafted)*	-	-	[444]
T700SC-Epoxy	15.94±2.01, 91.52±10.89 *(CNT-grafted)*	-	-	[445]
T700S-Epoxy	20.4±1.06, 66.0±4.16 *(CNT-grafted)*	-	-	[446]
AS4C-Epoxy	102.6±7.7, 100.6±5.1 *(CNT-grafted)*	-	-	[447]
IM7-PMMA	12.5±0.2 *(unsized)*, 15.8±0.4 *(CNT-grafted)*	-	-	[448]
E-GF-Epoxy *(numerical model fitted to SFFTs in* [83,146]*)*	110	12.12	1.0	[145]
E GF-Epoxy	-	120	0.01	[146]
E GF-Epoxy	-	105 *(new debonds)*, 98 *(whole)*	-	[83]
GF-Epoxy *(FEM)*	94-188	10-40	0-0.2	[436]
Untreated E-GF-Epoxy	30±7	571±162	-	[449]
E-GF-Epoxy	43±11	957±216	-	[449]
S2 GF-Epoxy	49.26 *(mean fragment length by AE)* 50.59 *(mean fragment length optically)*	-	-	[87]
GF-Epoxy *(FEM)*	40	20, 50, 50	0.3	[102]
GF-Epoxy *(inverse analytical model for SFFTs in* [146]*)*	65	60	-	[190]
GF-Epoxy	-	59.7 *(dry GF)* 15.8 *(wet GF)*	0.1 *(dry GF)* 0.1 *(wet GF)*	[164,450]
GF-Epoxy *(inverse analytical model for SFFTs in* [164,450]*)*	53 *(dry GF)* 32 *(wet GF)*	64 *(dry GF)* 18 *(wet GF)*	-	[190]
E GF-HDPE	3-14	57-106	-	[435]
E GF-PP	33.0±6.0 *(slow-cooled specimens, high crystallinity)* 9.5±1.9 *(fast-cooled specimens, low crystallinity)*	-	-	[451]
GF-PP	3.5-7.4 *(sizing/surface treatment dependent)*	-	-	[452]

Table 3.A. Reported interfacial properties from single-fibre pull-out tests of CF- and GF-reinforced composites.

Material	IFSS [MPa]	IFFT [J/m^2]	Friction Coeff.	Ref.
CF-Epoxy	64.6±8.2 *(untreated)*, 84.1±19.4 *(treated)*	-	-	[22]
AS4-DGEBA Epoxy	61±2, 88±5	-	-	[229]
AS2-EPON 815	48±4	-	-	[229]
T300-Epoxy *(fibre bundle pull-out)*	43.7±4.8	-	-	[411]
T700SC-Epoxy *(fibre bundle pull-out)*	36.3±4.3	-	-	[411]
HMS40-Epoxy	41±2	-	-	[242]
CF-Epoxy	72.7	37.7	1.25	[266]
T700S-Epoxy	~80 *(sized)* ~60 *(unsized)*	-	-	[240]
CF-Epoxy *(FEM fitted on* [453]*)*	45	562.5	-	[273]
AS1 CF-Epoxy	60	>100	0.42-0.58 *(cure temperature dependent)*	[216]
CF-Epoxy *(FEM)*	15-45	562.5	0.15-0.25	[273,454]
CF-Epoxy *(FEM fitted on* [453]*)*	45	562.5	0.9	[274]
PAN-based CF-Epoxy	75.2±4.2 *(unsized)*, 118.3±1.9 *(CNT-grafted)*	-	-	[60]
CF-Epoxy	27.4±2, 46.8±1.1 *(CNT-grafted)*	-	-	[455]
AS4C-Epoxy	79.7±2.5, 73.3±1.6 *(CNT-grafted)*	-	-	[447]
AS4-PEEK	92±15	-	-	[229]
AS4-PA	85±24	-	-	[229]
CF-PA 6,6	39-112 *(various data reduction methods)*	-	-	[239]
CF-PA 6,6	48.8±30.1	-	-	[456]
CF-HDPE	2.9-9.4 *(various sizings)*	-	-	[457]
GF-Epoxy	-	-	0.34-0.76	[237]
GF-Epoxy	34	140 *(cure temperature dependent)*	1.08-1.52 *(cure temperature dependent)*	[216]
GF-Epoxy	55-141 *(various epoxies, pull-out rate & data reduction methods)*	3-94 *(various epoxies, pull-out rate & data reduction methods)*	-	[239]
GF-EPON 815	-	50±14	0.83	[277]
GF-PES	-	-	0.23-0.38	[237]
GF-PES	10	300-350 *(cure temperature dependent)*	0.56	[216]
GF-PP	16.2±3.7	-	-	[456]
GF-PP	8.2-17.3 *(sizing/surface treatment dependent)*	-	-	[458]
GF-LDPE	15	-	-	[8]
GF-PA 6,6	-	5-6	-	[222]
GF-PC	15-22 *(function of l_{emb})*	40	-	[222]
GF-PES	60-65	110-180	2.0-5.0	[80,245]

Table 4.A. Reported interfacial properties measured via microbond tests of CF- and GF-reinforced composites.

Material	IFSS [MPa]	IFFT [J/m^2]	Friction Coeff.	Ref.
CF-Epoxy	48.3±14.1 *(untreated)*, 69.7±19.7 *(treated)*	-	-	[22]
Celion *(PAN-based)* CF-Epoxy	57	-	-	[285]
AS4 CF-Epoxy *(quasi-disk)*	20±1.65	-	-	[306,322]
AS4 CF-Epoxy *(droplet)*	33.7±8.93	-	-	[306,322]
AS4 CF-Epoxy	35.7-54.7 *(curing scheme dependent)*	-	-	[314]
AS4 CF-Epoxy	50.3	-	-	[300]
AU4 CF-Epoxy	23.4	-	-	[300]
AS4 CF-Epoxy	55.3 *(Eq. 13)* 37.1-73.3 *(regression approximations)*	-	-	[313]
HM40 CF-Epoxy	33±4 *(Eq. 13)* 40±4 *(extrapolation of Eq. 25, independent of l_{emb})* 39±5 *(LRS, max. of Eq. 58 plots)*	-	-	[343]
HMS40 CF-Epoxy	37±4 *(Eq. 13)* 47±4 *(extrapolation of Eq. 13, independent of l_{emb})* 50±5 *(LRS, max. of Eq. 34 plots)*	-	-	[343]
CNT Fibre-Epoxy	14.4	-	-	[459]
T300 CF-Epoxy	65±3 *(unsized)*, 135±9 *(coated + CNT-grafted)*	-	-	[460]
T300 CF-Epoxy	65±3 *(unsized)*, 126±6 *(CNT-grafted)*	-	-	[461]
T300-Epoxy	121, 166 *(CNT-grafted)*	-	-	[462]
HT CF-Epoxy	43±3, 55±6 *(CNT-grafted)*	-	-	[463]
T300 CF-PEEK	44.87±5.76	-	-	[290]
T700SC CF-PPS	35.2-51.0 *(test speed and data reduction scheme dependent)*	-	-	[312]
CF-PA 6,6	37.3±19.2 *(from F_d and F_{max})* 47.9±29.0 *(from $F_{max}(l_{emb})$)* 48.8±30.1*(from F_b and F_{max})*	-	-	[349]
E GF-Epoxy	33	-	-	[285]
E GF + Silane-Epoxy	49	-	-	[285]
GF-Epoxy	49.5	9.8	-	[319]
GF-Epoxy	46-80 *(test speed & hardener dependent)*	32-246 *(test speed & hardener dependent)*		[320]
GF-Epoxy *(FEM compared to* [464] *experiments)*	25, 50, 100	50, 100	0.1, 0.3	[304]
E GF-Epoxy	89 *($IFSS_{avg}$)* 100 *(Greszczuk)*	885 *(Piggott)* 971 *(Penn & Lee)* 239 *(Scheer-Shear Lag)* 243 *(Scheer-Variational)*	-	[347]
S GF-Epoxy *(FEM compared to* [336] *experiments)*	120	160	0.54	[305]
GF-Epoxy *(FEM to fit their experiments)*	68	3740	0.1	[360]
GF-Epoxy	45.8±0.5 *(linear regression)* 48.7±12.8 *(stress-based model* [316]*)*	-	-	[301]
E GF-Epoxy	43.5±2.3	-	-	[307]
GF-Epoxy	118.1 *(by direct crack length measurement)*	117.6 *(by direct crack length measurement)*	-	[243]
E GF-Epoxy	22.1±0.2	262±14	-	[329]
FBG-Epoxy *(FEM fitting on experiments)*	9-11 *(varying l_{emb} and $d_{droplet}$)*	41-130 *(varying l_{emb} and $d_{droplet}$)*	-	[357]
E GF-PP *(fitting Eq. 16 & Eq. 18, 19.A-21.A)*	13.5	4.66	-	[331]
E GF-PS *(fitting Eq. 16 & Eq. 18, 19.A-21.A)*	94.0	82.7	-	[331]
E GF-ABS *(fitting Eq. 16 & Eq. 18, 19.A-21.A)*	103.9	136.4	-	[331]
GF-PP	2.8-5.2 *(melt flow rate & maleic anhydride content dependent)*	-	-	[308]
E GF-PPS	27-31 *(Greszczuk model)*	41.8 *(Piggott model)* 29-57 *(Penn & Lee model)*	-	[309]
E GF-PP	18.3±3.4 *(from F_d and F_{max})* 16.3±4.2 *(from $F_{max}(l_{emb})$)*	-	-	[349]
E GF-PP	16.2±3.7 *(from F_b and F_{max})* 10.4 *(bare)*	-	-	[311]

24.5 *(sizing + MAPP)*

Table 5.A Reported interfacial properties from push-in/-out tests of CF- and GF-reinforced composites.

	Material	IFSS [MPa]	IFFT [J/m^2]	Friction Coeff.	Ref.
Push-in	CF-Epoxy	-	1.67±1-8.7±3.5	-	[392]
	CF-Epoxy *(FEM)*	50-100	2-100	0-1.0	[384]
	T800 CF-Epoxy *(Eq. 45)*	63±5	-	-	[384]
	AS4-8552 Epoxy *(Eq. 45)*	64±2.6	-	-	[465]
	AS4-8552 Epoxy *(Eq. 43 & 44)*	31±1.9	-	-	[466]
	CF-Epoxy *(FEM)*	100	10	0.2	[387]
	CF-Epoxy	75±9 *(bad adhesion)*-102±10 *(good adhesion)*	-	-	[382]
	CF-BMI	103±7 *(bad adhesion)*-117±10 *(good adhesion)*	-	-	[382]
	CF-PPS	-	3.79±2.1-18.72±4	-	[392]
	AS4-PEEK *(Eq. 69)*	37±1.2	-	-	[465]
	AS4-PEEK *(Eq. 43 & 44)*	16±0.8	-	-	[466]
	IM7-BMI *(FEM)*	40-100	2-80	0-0.6	[467]
Push-out	CF-Epoxy	-	4.7±2-42.6±5.1	-	[392]
	HS40-Epoxy	95 *(free-standing samples)*, 101 *(cave specimens)*	-	-	[389]
	HM63-Epoxy	89 *(free-standing samples)*, 93 *(cave specimens)*	-	-	[389]
	PAN-based CF-Epoxy	49.5±1.4 *(without CNTs)*, 50.6±2.8 *(CNT-grafted)*	-	-	[60]
	T700SC CF-PPS	-	24±15 *(untreated)* 57±23 *(annealed)*	-	[377]
	AS4-PEEK	-	171±10	-	[427]
	T300 CF-Epoxy *(FEM)*	13.7 *(calculated)*	13-32	0-0.9	[390]
	T700SC CF-Epoxy	56.4±5.3, 36.3±8.3 *(CNT-grafted)*	-	-	[468]
Push-in	E GF-Epoxy	73±5	-	-	[381]
	GF-Epoxy	80	100	-	[383]
	GF-TP	59±24	-	-	[382]
	GF-PA	21±5 *(bad adhesion & poorly polished)*-45±8 *(good adhesion)*	-	-	[382]
Push-out	GF-UPPH	52.9-64.2	81.3-107	0.35	[394]

For **Eq. 8** (section 3.3.2), the SERR for crack propagation in ***Gao-Mai-Cotterell model***, the parameters are define as follows:

$$k = \frac{\alpha\nu_f + \gamma\nu_m}{\alpha(1-\nu_f) + 1 + \nu_m + 2\gamma} \tag{1.A}$$

$$\beta = \frac{\gamma(1-2k\nu_m)}{\alpha(1-2k\nu_f)} \tag{2.A}$$

$$Q = T_m(l) = \frac{\alpha\nu_f(\tilde{P}+P)}{\alpha\nu_f + \gamma\nu_m}(e^{\lambda l}-1) \tag{3.A}$$

$$\tilde{P} = \frac{\pi r^2 q_o}{\alpha\nu_f}[\alpha(1-\nu_f) + 1 + \nu_m + 2\gamma] \tag{4.A}$$

$$\lambda = \frac{2\mu k}{r} \tag{5.A}$$

$$\alpha = E_m/E_f \tag{6.A}$$

$$\gamma = r^2/(R^2-r^2) \tag{7.A}$$

$$P = T_m + T_f \tag{8.A}$$

ν_f and ν_m are the Poisson's ratios, and T_m and T_f are the tensile forces on the matrix and fibre, respectively. q_o is the normal pressure exerted on the fibre due to the matrix shrinkage during cure and the mismatch of the CTEs, and l is the axial location of the crack front [225].

The *droplet profile* on a cylindrical fibre is determined by **Eq. 9** and **Eq. 10** (section 4.1) and:

$$a = \frac{h\cos\theta - r_f}{h - r_f\cos\theta} \tag{9.A}$$

$$k^2 = \frac{h^2 - a^2{r_f}^2}{h^2} \tag{10.A}$$

φ is an auxiliary parameter indicating the angle between a point on the droplet circumference and the y-axis (see Fig. 18), $F(\varphi,k)$ and $E(\varphi,k)$ are the Legendre's standard incomplete elliptic integrals of the first and second kind, l_{emb} and h (see Fig. 18) are evaluated experimentally, and the parameters φ_{max} and θ are determined at contact points $(x,y) = (\pm l/2, r_f)$ by:

$${r_f}^2 = h^2(1-k^2\sin^2\varphi_{max}) \tag{11.A}$$

$$l_{emb} = 2\left(ar_fF\left(\varphi_{max},k\right) + hE\left(\varphi_{max},k\right)\right) \tag{12.A}$$

For **Eq. 14-18** (section 4.3.2):

$$D_{3s} = \frac{1}{2}(\alpha_{1f} - \alpha_m) \tag{13.A}$$

$$C_{33s} = \frac{1}{2}(\frac{1}{E_{fL}} + \frac{V_f}{V_m E_m}) \tag{14.A}$$

$$D_3 = -\frac{V_m A_3}{V_f A_0}(\alpha_{fT} - \alpha_m) + \frac{1}{2}(\alpha_{fL} - \alpha_m) \tag{15.A}$$

$$C_{33} = \frac{1}{2}\left(\frac{1}{E_{f1}} + \frac{V_f}{V_m E_m}\right) - \frac{V_m A_3^2}{V_f A_0} \tag{16.A}$$

$$A_0 = \frac{V_m(1 - \nu_{fT})}{V_f E_T} + \frac{1 - \nu_m}{E_m} + \frac{1 + \nu_m}{V_f E_m} \tag{17.A}$$

$$A_3 = -\left(\frac{\nu_{fL}}{E_f} + \frac{V_f \nu_m}{V_m E_m}\right) \tag{18.A}$$

L, T, f and m subscripts indicate longitudinal, transverse, fibre, and matrix, α is the CTE, E is the elastic moduli, V is the volume fraction, and ΔT is the temperature drop over the cool down.

The resulting expressions (section 4.3.2) are [331]:

$$\sigma_d = \frac{2\tanh(\beta l_{emb})}{\beta r_f}[\tau_{ult} - \tau_{thermal}\tanh(\beta\, l_{emb}/2)] \tag{19.A}$$

$$\tau_{ult} = \frac{F_d \beta}{2\pi r_f \tanh(\beta l_{emb})} + \tau_{thermal}\tanh(\beta\, l_{emb}/2) \tag{20.A}$$

$$\tau_{app} = [\tau_{ult} - \tau_{thermal}\tanh(\beta\, l_{emb}/2)]\frac{\tanh(\beta l_{emb})}{\beta l_{emb}} \tag{21.A}$$

$$\tau(l_d) = \beta\coth[\beta(l_{emb} - l_d)]\left(\frac{F}{2\pi r_f} - \tau_f l_d\right) + \tau_{thermal}\tanh\left[\frac{\beta(l_{emb} - l_d)}{2}\right] \tag{22.A}$$

τ_f is the post-debond frictional shear stress in the debonded regions, and the shear-lag parameter, β, can either be based on Cox formulation [106] (imprecise at low V_f, see Table 1.A) or, more accurately, on Nayfeh's β definition [110]:

$$\beta_{Nayfeh}{}^2 = \frac{2}{E_{Lf} E_m r_f^2}\left(\frac{E_{Lf} V_f + E_m V_m}{\frac{V_m}{4G_{Lf}} + \frac{1}{2G_m}\left(\frac{1}{V_m}\ln\frac{1}{V_f} - 1 - \frac{V_f}{2}\right)}\right) \tag{23.A}$$

G_{Lf} is the longitudinal shear modulus of the fibre and can be determined by a torsion pendulum [469,470]. The residual thermal stress is given by:

$$\tau_{thermal} = -E_{Lf}\beta r_f D_{3s}\Delta T \tag{24.A}$$

A set of $\tau\ (l_d)$ curves, corresponding to different τ_f values, can be plotted for a microbond specimen using Eq. 40, and the 'optimally flat' plot can be used to determine the best-fit values

of τ_d and τ_f [324]. By acknowledging $G_{ic} \cong$ constant and the best fit to the experimental τ_{ult} data using $\tau_{ult} \propto {d_f}^{-1/2}$ approximation, the interfacial failure was better viewed as an energy-controlled phenomenon for a GF-epoxy system [331]. However, it was reported that the fitted curves of both debonding initiation criteria (G_{ic} and τ_{ult}) to the microbond experimental data were identical [331].